Computational Modelling of Yttrium Stabilised Zirconia in Catalysis

Thesis submitted for the degree of Engineering Doctorate

Crispin Cooper

Department of Chemistry
University College London

2013

Declaration

I, Crispin Cooper confirm that the work presented in this thesis is my own. Where information has been derived from other sources, I confirm that this has been indicated in the thesis.

…….....

Abstract

This thesis employs a range of computational modelling techniques to explore the structure, properties and catalytic activity of yttrium stabilised zirconia (YSZ) with a focus on its functions as a catalyst in methane reforming by partial oxidation.

The surface and bulk properties of the material are explored, including the use of an exhaustive search of all possible defect configurations at a low yttrium loading in a bulk and a surface system allowing conclusions to be drawn about the relationship between defect configurations and stability.

One significant property of YSZ materials is their ability to become oxygen ionic conductors at high temperatures, which is crucial to their use in solid oxide fuel cells and may be significant in catalytic applications. This thesis presents results of calculations designed to explore the effects of surfaces and defects on the ionic conductivity of YSZ materials, presenting evidence that oxygen conduction may be significantly enhanced at the surfaces of the material.

Calculations using electronic structure techniques are carried out to examine the catalytic properties of YSZ. Initially potential surface active sites are characterised. The surface model is then shown to strongly adsorb and activate molecular oxygen, carbon dioxide and water from the gas phase. The energetics and electron movements in these surface interactions are described. These results provide the basis for investigations of reforming reactions in subsequent chapters and will be of interest in investigations of other catalytic processes over YSZ materials.

A novel mechanism of methane C-H bond activation is reported over YSZ, activated by the presence of an adsorbed partially reduced O_2 species. The mechanism is investigated in detail, including the use of two electronic structure techniques to allow mechanistic details to be proposed and activation energy estimated. It may be that this mechanism is more generally applicable to oxidative C – H bond activation over many metal oxide materials.

List of Contents

List of Abbreviations

AIMs	-	Atoms In Molecules
ATR	-	AutoThermal Reforming / AutoThermal Reformer
BFGS	-	Broyden Fletcher Goldfarb Shanno
BLYP	-	The DFT functional of Becke, Lee, Yang and Parr
Ch.	-	Used to denote a chapter
DFT	-	Density Functional Theory
EPR	-	Electron Paramagnetic Resonance
eV	-	Electron Volt, a unit of energy equivalent to 1.602×10^{-19}J
Fig.	-	Used to denote a figure
GGA	-	Generalised Gradient Approximation
GULP	-	General Utility Lattice Program
HF	-	Hartree-Fock
HSE	-	The hybrid DFT functional of Heyd, Scuseria and Ernzerhof.
IR	-	Infra Red
KS	-	Kohn-Sham
LDA	-	Local Density Approximation
MEP	-	Minimum Energy Pathway
MP*x*	-	Møller-Plesset perturbation theory of order *x*.
MS	-	Mass Spectroscopy
NEB	-	Nudged Elastic Band
NN	-	Nearest Neighbour
NNN	-	Next Nearest Neighbour
OCM	-	Oxidative Coupling of Methane
PAW	-	Projector Augmented Wave
PBE	-	The DFT functional of Perdew, Burke and Ernzerhof.
PW91	-	The 1991 DFT functional of Perdew and Wang
QM	-	Quantum Mechanical

SCF - Self Consistent Field

SOD - Site Occupancy Disorder

SOFC - Solid Oxide Fuel Cell

Syngas - Synthesis Gas, a mixture of carbon monoxide and hydrogen

Tab. - Used to denote a table

TPD - Temperature Programmed Desorption

VASP - Vienna Ab-initio Simulation Package

WGS - Water Gas Shift

XRD - X-Ray Diffraction

YSZ - Yttrium Stabilised Zirconia

Chapter 1. Methane Reforming

This chapter discusses the significance of catalytic methane reforming in its industrial context. The creation and uses of synthesis gas are discussed, as are the different reforming reactions by which it is created. Several catalytic systems are discussed to provide broad context. One specific catalytic system, the autothermal reformer, is discussed in detail. The available literature regarding methane reforming catalysis over zirconia materials is reviewed, providing vital background for the work outlined in later chapters of this thesis.

1.1 Catalytic Partial Oxidation of Methane

Catalytic partial oxidation of natural gas to produce higher value products, both directly through coupling and via synthesis gas (a mixture of carbon monoxide and hydrogen produced by selective partial oxidation reforming processes), has great value in making use of an abundant and relatively low value resource. In this section catalytic methane reforming will be discussed generally and will focus in depth on the role of YSZ materials.

Methane is the main constituent of natural gas which is extracted from the ground on its own or along side heavier hydrocarbons including oil, or by the process of 'fracking' suitable gas rich shale rocks. Methane is also a by-product of many biological processes. Natural gas is a widely distributed and relatively abundant fossil fuel, with proven reserves of $2.08x10^{17}dm^3$ in 2011[1]. However, methane is a relatively poor fuel due to its low volumetric energy density ($3.78kJ.dm^{-3}$) as well as requiring the complexity of high pressure cryogenic transportation and storage. Products of much greater utility and therefore value can be derived from methane by 'upgrading' through oxidative reforming. Reforming processes have allowed methane from natural gas to become an important raw material for many valuable industrial processes, including hydrogen production, synthetic fuels and methanol synthesis[2]. Literature regarding catalytic methane reforming can be found dating back to 1902, when Senderens and Sabatier[3] demonstrated the formation of synthesis gas from methane in an example of nickel catalysed steam reforming. Methane reforming and upgrading processes are now very valuable and used on a large scale in industrial applications.

1.2 Oxidative Coupling

Oxidative coupling of methane (OCM) involves the direct conversion of methane and oxygen to higher hydrocarbons and water. OCM normally takes place over a heterogeneous metal oxide catalyst. The target product is most commonly ethylene, as it has a relatively high market value and demand. Ethylene is not the initial reaction product. Interaction of methane with the surface of the catalyst

generates both gas phase and adsorbed methyl radicals[4]. The coupling of methyl radicals leads to the formation of ethane, and subsequent reactions convert a large proportion of this to ethylene. Further radical reactions may lead to small proportions of higher hydrocarbons in the product mixture. Inevitably there is some production of unwanted CO_x products which is undesirable as it represents an inefficient use of methane, generates unwanted heat and CO can poison many OCM catalysts[5].

1.3 Synthesis Gas

Synthesis gas (syngas) is produced by partial oxidation of light hydrocarbons and is an important intermediate in the majority of processes which use natural gas as a raw material. Syngas is primarily a mixture of carbon monoxide and hydrogen in variable proportions and may also contain a small fraction of carbon dioxide and water as products of complete combustion and possibly other trace impurities depending on the process and feedstock. Synthesis gas has a wide range of important industrial applications, the most significant of which are the Fischer-Tropsch process, methanol synthesis and hydrogen production. A range of the uses of syngas is summarised in the diagram below, reproduced from Choudhary et al[2].

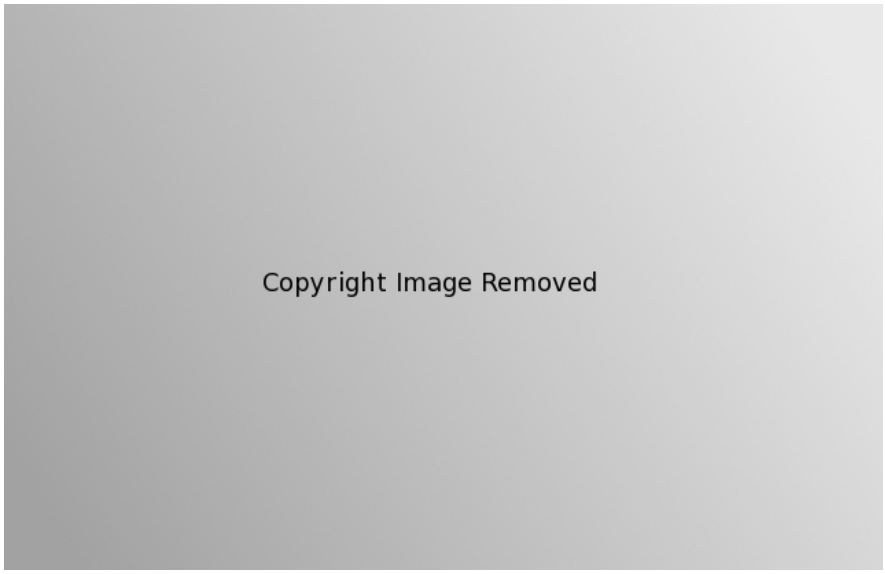

The principle uses of Syngas

(Fig. 1.3.1)

The Fischer-Tropsch process produces longer chain hydrocarbons including high grade synthetic fuels, waxes and products of further use in synthetic chemistry as shown below:

$$(2n+1)H_2 + nCO \rightarrow C_nH_{(2n+2)} + nH_2O$$

(Eq. 1.3.1.)

Methanol may either be used as a liquid fuel or a feedstock for a variety of chemical synthesis processes. The chemical equation for syngas to methanol is shown below:

$$CO + 2H_2 \rightarrow CH_3OH$$

(Eq. 1.3.2.)

Almost all commercially available hydrogen is produced via the reforming of hydrocarbons. The significance of this hydrogen is hard to overestimate since it is used in wider array of refinery processes and other hydrogenations. Arguably its most vital use is in nitrogen fixation via the Haber–Bosch process to produce synthetic fertilisers which are necessary to feed a large portion of the global population. The chemical equation for ammonia synthesis by the Haber-Bosch process, typically a promoted iron catalyst is used, is given below:

$$N_2 + 3H_2 \rightleftharpoons 2NH_3$$

(Eq. 1.3.3.)

Where hydrogen production is the desired application, carbon monoxide can be further oxidised to carbon dioxide using water as the oxidant to liberate hydrogen from the water in a reaction known as the water gas shift (WGS) process.

$$CO + H_2O \leftrightarrow CO_2 + H_2$$

$$\Delta H = -41 kJ.Mol^{-1}$$

(Eq. 1.3.4)

The ratio of products which make up syngas may also be controlled to some extent by varying the composition of the feed gases, i.e. the oxidants used. Oxidant feedstocks may include oxygen, water, carbon dioxide or any mixture of these components. The overall reactions and energetics for these processes are provided below. Enthalpies given are at 298K and taken from Zhu et al[6].

	Oxidant	Overall Reaction	ΔH (kJ.Mol^{-1})
Dry	CO_2	$CH_4 + CO_2 \rightarrow 2CO + 2H_2$	+246
Steam	H_2O	$CH_4 + H_2O \rightarrow CO + 3H_2$	+205
Direct Oxidation	O_2	$CH_4 + O_2 \rightarrow CO + H_2 + H_2O$	-278

Reactions and energetics of methane reforming reactions.

(Tab. 1.3.1)

As can be seen, both dry and steam reforming are highly endothermic, while direct oxidation is exothermic. Complete combustion is highly exothermic[6] at −891kJ.Mol^{-1}. It will also be apparent that different product ratios will result from use of differing oxidants and could therefore produce a synthesis gas more suitable for one use or another.

1.4 Metal Catalysts

Reports of metal catalysed methane reforming date back over a century. Early examples include Senderens and Sabatier[3] in 1902, Liander[7] in 1929 and in 1933, Padovani[8]. In 1946 Prettre et al[9] used supported nickel and were able to convert a 2:1 mixture of methane and oxygen to a 2:1 mixture of hydrogen and carbon monoxide (syngas) with high overall conversion. These early researchers noted problems with carbon deposition.

Published in 1990, the work of Green, Ashcroft and Vernon[10] drew substantial interest to the research area by demonstrating that high selectivity for and yield of syngas were achievable over noble metal catalysts. This occurred as an accidental finding while studying $La_2Ru_2O_7$ as a potential oxidative coupling catalyst. It was found that metallic ruthenium on a lanthanum oxide support had been produced on heating the material, resulting in substantial syngas production approaching thermodynamic equilibrium. Following this work, in 1993 another

group[11] demonstrated that almost total methane conversion with extremely high syngas selectivity was possible over noble metals supported on alumina.

Rhodium, ruthenium, iridium, platinum and palladium have all been studied as methane reforming catalysts, either produced from mixed oxide precursors or on alumina supports. When relative carbon deposition rate was explicitly studied[12-14] it was found that iridium and rhodium suffer negligible carbon deposition. The rates of carbon deposition on the metals was found to follow the following order; Ni > Pd > Rh > Ir. The same research also distinguished between two possible mechanisms of carbon deposition:

$$2CO \rightarrow C_{(s)} + CO_2 \qquad \text{(Eq. 1.4.1.)}$$

$$CH_4 \rightarrow C_{(s)} + 2H_2 \qquad \text{(Eq. 1.4.2.)}$$

The studies conclude that second of these reactions (Eq. 1.4.2.) was the most significant cause of carbon deposition on the catalysts studied. A mixed platinum – palladium catalyst has been used in experiments examining the order of reactions in catalytic systems[15]. It was thought on the basis of the results that near total oxidation, limited by oxygen availability, to produce steam, carbon dioxide and carbon monoxide was the initial step. This is then followed by the reactions of dry and steam reforming and to a lesser extent, the water shift reaction, to produce the final product ratio.

The much reduced cost of nickel compared to platinum or ruthenium has made it an attractive option and as such it has been the subject much research. In 1991 Lunsford et al[16] found that an alumina supported nickel catalyst could produce excellent results. However, they found that carbon deposition was a problem and that the system was not stable unless excess oxygen was included in the feed gas. They also found that different phases were present in this catalyst system, with one (nickel oxide on alumina) catalysing unwanted total combustion.

In order to reduce carbon deposition on nickel based catalysts many support materials have been investigated. In 1992 Choudhary and co-workers[17] achieved

extremely high conversion and selectivity over a magnesium oxide supported nickel catalyst. They also investigated many other oxide materials and rare-earth doped alumina as potential support materials, publishing their results in a large number of articles[17-27]. This research allowed a comparison of the performance of different support materials, finding that some gave improved stability and activity (magnesium and calcium oxides), while others were of little use due to problems of sintering (silicon dioxide and titanium dioxide). It was found that all the catalyst systems, to varying degrees, suffered from a reduction in nickel surface area and soot formation when operating. Even the highly active magnesium oxide supported nickel catalyst was found to produce carbon deposits, gradually deactivating itsself. Other groups have also studied the MgO supported system, its activity and relative stability[28-30]. It is thought that the weakly basic nature may reduce carbon deposition and that even distribution of nickel throughout the support also aids its stability. Keeping metal particles small is thought to slow carbon deposition, while surface oxide species are thought to be helpful in oxidising and removing carbon.

Other supports investigated for use in nickel based systems include perovskite type materials, which are thought[31] to be able to resist carbon deposition by producing dispersed and very small nickel particles which are below the size needed for rapid carbon formation. It is suggested that the perovskite materials may also be able to produce reactive oxygen species which will be able to oxidise and remove any carbon soot formed. In an attempt to produce a material with a more controlled nickel particle size various methods of producing the perovskite supported nickel have been investigated[32].

Metal catalysts including platinum, rhodium and nickel have also found use supported on YSZ materials. YSZ has a number of properties (discussed subsequently) making it an effective and active support material for methane oxidation catalysis.

1.5 Auto-thermal Reforming

An important industrial reforming process, and that of greatest significance in this thesis, couples steam reforming with direct oxidation and is termed auto-thermal reforming (ATR). The auto-thermal reforming process takes place in a cylindrical reaction vessel designed to operate at very high flow rates, as depicted in the simplified schematic below (fig. 1.5.1).

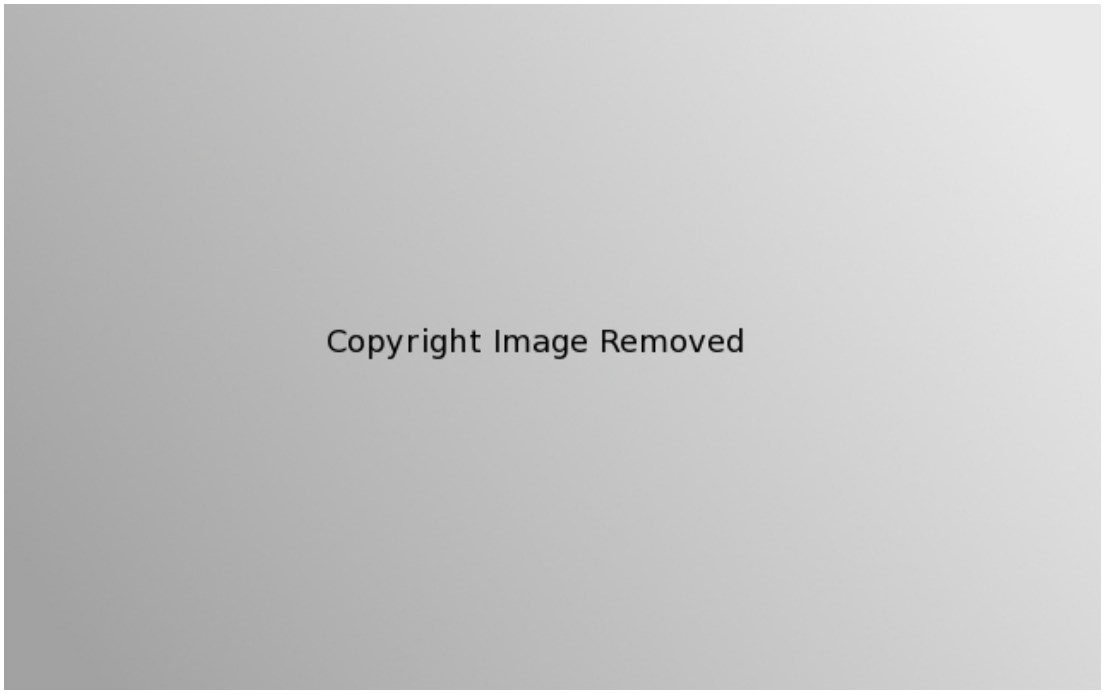

(Fig. 1.5.1.)

The methane and steam mixture is pre-heated before being mixed with an oxygen source at the top of the reactor vessel. There is then space in which gas phase reactions including complete and partial combustion occur and the temperature will rise further. The hot reacting gas mixture then reaches the catalyst bed which consists of platinum group or transition metal particles supported on a metal oxide material. It is on and above the catalyst material that a wide array of reactions take place to yield the product mix. The temperature in the combustion zone and catalyst bed can be extremely high, up to 1200ºC.

1.6 YSZ as a Catalyst

An effective catalyst material must have a set of specific properties beyond activity for the desired reactions. The reforming reaction takes place at extremely high temperatures which any catalyst / support combination must be able to withstand, including allowance for potential hotspots from exothermic reactions. In addition to thermal stability, the catalyst must be mechanically robust and chemically stable under reaction conditions. A resistance to deactivation through coking, poisoning, surface restructuring, loss of active sites and other means is also required. One material which meets many of these requirements and has found industrial use as an active support material is cubic yttrium stabilised zirconia (YSZ). YSZ is used as a support for metallic particles, but has been shown to be far from inert under autothermal reforming reaction conditions and plays an active role in the catalytic process. YSZ materials will form the basis of this research project.

Yttrium stabilised zirconia has been shown to be a very active partial methane oxidation catalyst for an irreducible oxide, although not as selective and active as the supported metal catalysts. Zhu et al[6,33,34] have performed a substantial experimental investigation into the reaction scheme of partial oxidation of methane over YSZ. The study made use of in situ infra-red (IR) spectroscopy and mass spectroscopy (MS) to observe both the surface species and products during the experiments. The active surface was also investigated by cooling the catalyst immediately from its active state and then performing temperature programmed desorption (TPD). IR and MS were used to analyse the desorbed species. Zhu et al found that methane could react with surface reactive oxygen species at temperatures of 400C or possibly even lower (significantly lower than for the supported metal catalysts[35]). Based on this work they proposed the following reaction scheme, reproduced from Zhu et al[6]:

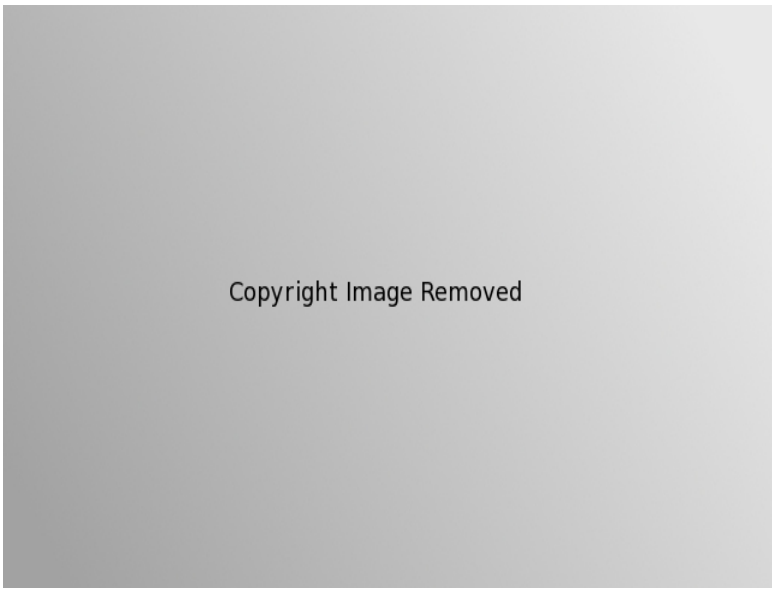

A proposed reaction scheme for methane oxidation over YSZ. 'a' denotes adsorbed species.

(Fig. 1.6.1.)

Figure 1.6.1 illustrates the proposed oxidation processes on YSZ. The first step is the formation of adsorbed formaldehyde by reaction of methane with reactive oxygen species on the oxide surface. Formaldehyde can then be oxidised in the gas phase or via formate adsorbed on the surface. The adsorbed formaldehyde is oxidised to formate by neighbouring lattice oxygen. It is thought[36] that this occurs on low index planes rather than structural defects. Either pathway results in a mixture of CO, H_2, H_2O and CO_2. Secondary reactions of dry reforming, steam reforming and water gas shift can occur and are thought to enhance selectivity[37]. The study also analyses the relative rates of each of the pathways shown in Fig. 1.6.1 across a range of temperatures. At temperatures greater than around 600ºC, the rate limiting step is found to be the initial activation of methane (transformation 1 in Fig. 1.6.1). Methane is a highly symmetrical and relatively stable molecule and as such it would be expected that the initial activation would be the rate limiting step.

The relative rates of subsequent reaction steps will determine the selectivity of the conversion process. Transformation 5 in figure 1.6.1 is the conversion of formaldehyde to syngas, transformation 3 and 4 yield hydrogen and carbon monoxide respectively with some combustion by-products of carbon dioxide or water. Transformation 9, proceeding via carbonate, yields only combustion products. According to Zhu et al approximately 97% of the methane is converted via

transformations 3, 4 or 5 with only ~2% proceeding along the complete combustion process via carbonate (9). However, transformations 3 and 4 account for 77% of the conversion yielding significant by-products, only 20% undergoes transformation 5 to syngas without combustion by-products.

Zhu et al discuss possible active sites and the role of oxygen based on ^{18}O exchange and pulsed reaction measurements. The mechanisms they propose are summarised in two diagrams, one for the process on monoclinic pure zirconia and the other on cubic YSZ:

The role of oxygen in methane oxidation over zirconia and YSZ materials.
(Fig. 1.6.2.)

They suggest that extractable surface O^{2-} species are the key sites for methane oxidation. The surface of both materials will allow the extraction of some oxygen, more in the case of pure zirconia. However, much higher activity is observed at elevated temperatures over YSZ, containing mobile oxygen vacancies. The proposed explanation for this is that YSZ is able to more rapidly absorb and transport oxygen to form active sites whereas pure zirconia requires direct replacement of oxygen from the gas phase at the same surface site. This is supported by evidence from labelled oxygen exchange experiments, with a significantly higher exchange rate being observed over YSZ materials. The temperature response is also consistent with this hypothesis, since it is at elevated temperatures that YSZ is able to exhibit rapid oxygen conductivity. The oxygen conductivity to surface sites is also believed to play a role in limiting carbon deposition, by allowing oxygen to move to adsorbed carbon

and burn it off. The reduction of carbon deposition on these materials is also discussed by Zhu et al, based on results of temperature programmed oxidation of surface carbon deposits.

The interaction of oxygen anion conducting materials with supported metal particles is also of interest. Oxide materials, including YSZ, can promote the activity of catalytic metal particles through a number of mechanisms. Interactions with surface atoms of the support material can alter the morphology and geometry of the metal particles, potentially presenting different faces and sites. The interface region between the metal particles and oxide support can provide a range of sites where a substrate may access both metallic sites and the ionic material. Support materials may conduct or 'spill over' oxygen ions on to the metallic particle and interface region. Finally the support material may itsself contain sites active for some or all of the steps in a catalytic process. Evidence from both modelling and experimental work has shed some light on the support-metal interactions on YSZ materials, a small subset of which is presented below.

The diagram below (fig. 1.6.3), reproduced from Huang et al[38], illustrates the proposed behaviour of oxygen on nickel supported on an ionically conductive oxide catalyst system in methane partial oxidation.

Summary of proposed reactivity of nickel on oxygen conductor catalysts. (Fig. 1.6.3.)

As can be seen in Fig. 1.6.3, oxygen may be reduced and adsorbed from the

gas phase on to the surface, incorporated in to the lattice and diffuse through the material. Adsorbed and incorporated oxygen species may interact with substrate molecules at surface sites such as vacancies and boundaries with the metal particles or may be transferred on to metal particles. In this way, the oxygen conducting materials may be both intrinsically catalytically active and promote the oxidative catalytic activity of metal particles supported on their surfaces.

Computational modelling has been applied to investigating the interaction of oxygen conducting materials and supported metal particles. Shishkin et al[39] applied DFT to nickel on YSZ as an oxidation catalyst at the anode of solid oxide fuel cell systems. The results of calculations show that oxygen may spill over from the YSZ material on to the nickel particles where it is active for oxidation reactions. The diagram below (Fig. 1.6.4) shows oxygen spillover from YSZ with and without a neighbouring oxygen vacancy, reproduced from Shishkin et al[39].

The circles and squares represent oxygen vacancies native to the YSZ structure and resulting from the spillover process respectively. The blue is nickel, red oxygen, grey zirconium and green yttrium.

(Fig. 1.6.4.)

While this thesis is focused on the catalytic properties of YSZ materials without metal particles, knowledge of the interactions with supported particles aids understanding of the materials properties and role in industrial catalysis. The moment of oxygen between YSZ and supported metal particles is likely a very important process in oxidation catalysis.

The catalytic methane oxidation processes described in this chapter constitute the industrial context of much of the work reported in this thesis. The information

presented in section 1.6 will form the basis for the exploration of catalytic reactions over YSZ.

References

[1] "BP Statistical Review of World Energy". *BP*, **2012**.

[2] T. Choudhary, V. Choudhary, *Angew. Chem. Int. Ed.* 47, 1828, **2008**.

[3] P. Sabatier, J. Senderens, *Compt. Rend*. 134, 514, **1902**.

[4] J. Lunsford, P. Hinson, M. Rosynek, C. Shi, M. Xu, X. Yang, *J. Catal.* 147, 301, **1994**.

[5] K. Peil, J. Goodwin, G. Marcelin, *Stud. Surf. Sci. Catal.* 61, 73, **1991**.

[6] J. Zhu, M. Mujeebur Rahuman, J.van Ommen, L. Lefferts, *Appl. Catal. A.* 259, 95, **2004**.

[7] H. Liander, *Trans. Faraday Soc.* 25, 462, **1929**.

[8] C. Padovani, P. Franchetti, *Giorn. Chem. Ind. Appl. Catal.* 15, 429, **1933**.

[9] M. Prettre, C. Eichner, M. Perrin, *Trans. Faraday Soc.* 42, 335, **1946**.

[10] A. Ashcroft, A. Cheetham, J. Foord, M. Green, C.Grey, A. Murrell, P. Vernon, *Science.* 344, 319, **1990**.

[11] D. Hickman, L. Schmidt, *Science.* 259, 343, **1993**.

[12] A. Ashcroft, A. Cheetham, J. Ford, M. Green, C. Grey, A. Murrell, P. Vernon, *Nature.* 344, 133, **1990**.

[13] P. Vernon, M. Green, A. Cheetham, A. Ashcroft, *Catal. Lett.* 6, 181, **1990**.

[14] J. Claridge, H. Green, C. Tsang, A. York, A. Ashcroft, D. Battle, *Catal. Lett.* 22:4, 299, **1993**.

[15] J. Hochmuth, *Appl. Catal. B.* 1, 89, **1992**.

[16] D. Dissanyake, M. Rosynek, K. Kharas, J. Lunsford, *J. Catal.* 132, 117, **1991**.

[17] V. Choudhary, A. Mamman, S. Sansare, *Angew. Chem. Int. Ed. Engl.* 31, 1189, **1992**.

[18] V. Choudhary, R. Ramarjeet, V. Rane, *J. Phys. Chem.* 96, 8686, **1992**.

[19] V. Choudhary, A. Rajput, V. Rane, *Catal. Lett.* 16, 269, **1992**.

[20] V. Choudhary, A. Rajput, B. Prabhakar, *Catal. Lett.* 15, 363, **1992**.

[21] V. Choudhary, S. Sansare, A. Mamman, *App. Catal.* 99, **1992**.

[22] V. Choudhary, V. Rane, A. Rajput, *Catal. Lett.* 22, 289, **1993**.

[23] V. Choudhary, A. Rajput, B. Prabhakar, *J. Catal.* 139, 326, **1993**.

[24] V. Choudhary, V. Rane, A. Rajput, *App. Catal. A.* 162, 235, **1997**.

[25] V. Choudhary, A. Rajput, B. Prabhakar, A. Mamman, *Fuel.* 77, 1803, **1998**.

[26] V. Choudhary, A. Mamman, *Fuel Proc. Tech.* 60, 203, **1999**.

[27] V. Choudhary, A. Mamman, *App. Energy*, 66, 161, **2000**.

[28] Y. Hu, E. Ruchenstein, *Ind. Eng. Chem. Res.* 37, 2333, **1998**.

[29] E. Ruckenstein, Y. Hu, *App. Catal. A.* 183, 85, **1999**.

[30] A. Santos, M. Menendez, A. Monzon, J. Santamaria, E Miro, E, Lombardo, *J. Catal.* 158, 83, **1996**.

[31] T. Hayakawa, H. Harihara, A. Andersen, A. York, K. Suzuki, H. Yasuda, K. Takehira, *Angew. Chem. Int. Ed. Engl.* 35, 192, **1996**.

[32] B. Basini, M. D'Amore, G. Fornasari, A. Guarinoni, D. Matteuzzi, G. Piero, F. Trifireo, A. Vaccari, *J. Catal.* 173, 247, **1998**.

[33] J. Zhu, J. van Ommen, L. Lefferts, *J. Catal.* 255, 388, **2004**.

[34] J. Zhu, J. van Ommen, A. Knoester, L. Lefferts, *J. Catal*. 230, 291. **2005** .

[35] R. Jin, Y. Chen, W. Li, W. Cui, Y. Ji, C. Yu, Y. Jiang, *Appl. Catal. A.* 201, 71, **2000**.

[36] J. Zhu, J. Ommen, L. Lefferts, *Catal. Today.* 117, 167, **2006**.

[37] J. Zhu, J. Ommen, A. Knoester, L. Lefferts, *J. Catal.* 230, 291, **2005**.

[38] T. Huang, H. Lin, T. Yu, *Catal. Lett.* 105, 239, **2005** .

[39] M. Shishkin, T. Ziegler, *J. Phys. Chem. C.* 13, 21667, **2009**.

Chapter 2. Zirconia Materials

Zirconia (ZrO_2) and related materials find a variety of commercial applications, including; refractory ceramics, structural engineering materials, ionic conductors in SOFCs (Solid Oxide Fuel Cells), oxygen sensing and purification, biomedical applications, synthetic gems in jewellery, and catalysts and catalyst supports for a variety of chemical processes. The material is frequently modified by doping with other metal oxides in order to tailor the properties. This section will introduce this family of materials, beginning with the natural mineral form and the properties of pure ZrO_2 before discussing doping and its effects, oxide ion conductivity, surface structure and finally surface properties and species relevant to its behaviour in catalytic applications.

2.1 Bulk Structure & Properties

Zirconia (ZrO_2, zirconium dioxide) can be found in nature as the rare mineral baddeleyite[1] which frequently contains hafnium, iron and titanium impurities[2]. The mineral was named after Joseph Baddely, a railway construction superintendent who found the first known sample while searching for a display specimen of another mineral for the Museum of Practical Geology, London[1]. Baddely found his sample near Rakwana, Sri Lanka (Ceylon at the time of the discovery). Below is an image of a baddeleyite specimen[3] and the general monoclinic structure of the material[4].

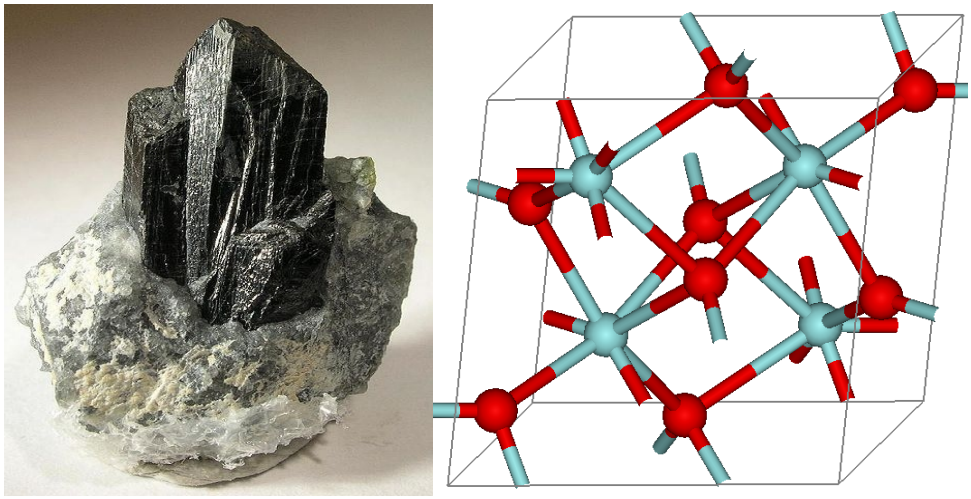

Images of a sample (left) and the monoclinic structure (right) of baddeleyite. Blue represents zirconium, red oxygen.

(Fig. 2.1.1)

Baddeleyite is frequently co-located with the mineral zircon ($ZiSiO_4$, zirconium silicate) in silicon poor formations. Baddeleyite is rarely found in in silicon rich environments as zirconia will convert to zircon. The structure and stability of baddeleyite make it suitable for lead – uranium geochronometry[5].

Pure zirconia adopts a monoclinic crystal structure at atmospheric pressure and low temperatures. At high temperatures, the material then undergoes a transition to tetragonal (1440K) and finally cubic (2640K) phases. There are also two known high pressure orthorhombic phases. A temperature / pressure phase diagram is provided below, reproduced from Bouvier et al[6].

A temperature – pressure phase diagram for pure zirconia.

(Fig. 2.1.2)

The two orthorhombic phases, O_I and O_{II} in figure 2.1.2 above, are only accessible at extremely high pressures. O_I may be formed at over 3GPa and O_{II} in the region of 20GPa[7]. These high pressure phase transformations result in a higher zirconium co-ordination number of up to 9 as the material is compressed. The orthorhombic phases play no significant role in the materials which are the subject of this research.

The monoclinic phase is found at temperatures of up to ~1440K at atmospheric pressure. In this phase the zirconium is sevenfold coordinated. There are two inequivalent oxygen environments, one having threefold coordination and the other fourfold. This structure is illustrated below[8], small spheres representing zirconium ions, the larger oxygen:

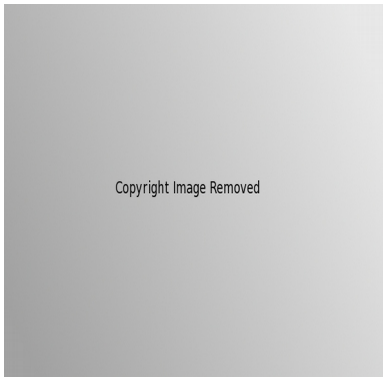

Monoclinic structure of zirconia. The larger circles represent oxygen, the smaller zirconium.

(Fig. 2.1.3)

The tetragonal phase occurs in the range of 1440 – 2640K at atmospheric pressure. In this phase zirconium is eightfold coordinated as shown in the structure below[8]:

Tetragonal structure of zirconia. The larger circles represent oxygen, the smaller zirconium.

(Fig. 2.1.4)

The cubic phase is the structure of primary interest in this study. In pure zirconia at atmospheric pressure it only occurs at high temperatures of >2600K but may be stabilised by doping across a very wide temperature range as described in the subsequent section (2.2). A visualisation of the cubic structure, also containing eightfold zirconium, is provided below[8]:

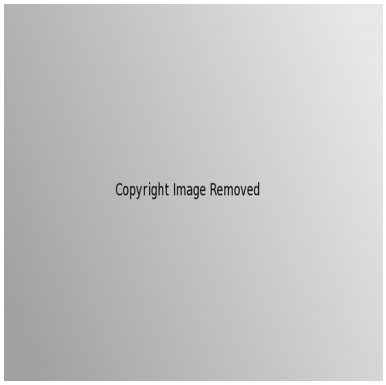

Cubic structure of zirconia. The larger circles represent oxygen, the smaller zirconium.

(Fig. 2.1.5)

Transitions between the phases are accompanied by large changes in volume, particularly between the monoclinic and tetragonal due to the change in zirconium coordination, resulting in the material being unstable when exposed to temperature variations which cross phase boundaries and hence it is unsuitable for applications where structural stability across a broad temperature range is paramount.

There have been a number of computational simulations of zirconia materials which attempt to correctly predict the phase behaviour[9-17]. In the case of potential based models, they have largely been limited to describing structure or properties of the phases for which they are fitted. Despite this limitation classical potential models of zirconia materials have been reported[9-17] which have contributed substantially to the understanding of its structure and properties.

There are no reported classical potential models which correctly describe all the phases of zirconia despite several attempts and improvements. A number of differing methods have yielded varying levels of success in describing the phase behaviour. Examples include breathing ion models[10], models derived from

electronic structure calculations[9] and compressible ion models[17]. There are difficulties in producing an adequate potential model for this material resulting from its electronic structure and the assumptions such models must make. The electron clouds surrounding each ionic core will deform in a manner that is hard to model precisely using classical potential approximation methods such as breathing or compressible ions models.

Subtle polarisation and covalent effects are thought to be crucial in stabilising the lower symmetry and coordination monoclinic phase with respect to the cubic structure and cannot be easily included in potential models. Calculations utilising electronic structure techniques[18-22] have been carried out and in conjunction with other investigations[23-25] suggest that the covalent component of the interactions in ionic systems such as zirconia is significant in stabilising the lower coordinated, lower symmetry phase. Such structures have been found to have a somewhat less ionic and more covalent nature when compared to the cubic structure.

2.2 Doping and Stabilisation

In order to produce a ceramic material with stability across a wide temperature range and other potentially desirable properties such as oxygen conductivity and specific surface features, it is necessary to introduce impurities or dopants. There are a variety of cationic dopants which may be used in specific quantities in order to produce a wide range of properties and features.

Doped zirconia materials may be prepared in several ways, including co-precipitation, milling or by melting source materials in a crucible. The most appropriate preparation method and source materials will depend on factors such as quantity of material required, desired grain or crystal sizes and the desired dopant element and concentration.

In most cases, one effect of doping is to stabilise the cubic or near cubic phase across a wide range of temperatures. The range of dopants and their effects are reviewed briefly below before detailed attention is paid to a singe doped zirconia material, YSZ. Dopants can be loosely grouped based on the valency of the metal (M^{n+}) cation. M^{2+} species commonly used include Ca^{2+} and Mg^{2+} [26]. In this case the

metal ions occupy the lattice sites usually occupied by Zr^{4+} cations and are charge compensated by one oxygen vacancy per cation substitution. Each O^{2-} vacancy has an effective charge of 2+ whilst the substation of Zr^{4+} by M^{2+} has an effective charge of 2- so the doping is overall charge neutral with the defects occurring in a 1:1 ratio. The doping process can be more concisely expressed in Kröger-Vink notation[27], M representing a generic metal.

$$MO + Zr_{Zr} + O_O \rightarrow M_{Zr}^{''} + V_O^{\cdot\cdot} + ZrO_2$$

(Eq. 2.2.1)

The creation of oxygen vacancies may stabilise the material's structure across a wide temperature range by reducing the mean zirconium coordination number relative to the pure material when the zirconium cation sublattice is in the cubic arrangement and allowing the oxide anion sublattice to relax. Oxygen vacancies induced through doping with di or trivalent cations inhibit certain phonon modes which would otherwise drive the phase transition. Potential limitations of doping with highly charge mismatched (i.e. Ca^{2+} on a Zr^{4+}sites) include lattice instability and the possibility of phase segregation at elevated temperatures[28]. There is reason to expect that potential phase segregation, clustering of defects and trapping of oxide vacancies would make M^{2+} stabilised zirconia a poor ionic conductor when compared to other zirconia materials. Instability of this class of materials means that they are suitable for different uses compared to highly stable, (fully stabilised) zirconia materials.

Another way to stabilise the cubic phase is the addition of larger metal cations (M^{4+}) with the same ionic charge as the zirconium ions they replace. By far the most common metal used to produce this class of materials is cerium in the form of cerium oxide (CeO_2). Ce^{4+} has an ionic radius of 92pm compared to Zr^{4+} at 79pm leading to expansion and stabilisation of the cubic lattice when used in sufficient concentration. Ce^{4+} substituting Zr^{4+} is charge neutral and will create no oxygen vacancies. Cerium is however readily reducible from Ce^{4+} to Ce^{3+}, unlike the zirconium for which it substitutes[29]. Trivalent cerium has both a larger radius (103.4pm) and may give rise to charge compensating oxygen vacancies. Cerium is typically required at very high

concentrations to achieve significant stabilisation[30], 30% will stabilise the tetragonal phase whilst levels as high as 70% are required to fully stabilise the cubic phase at high temperatures.

The cubic phase of zirconia can be stabilised though oxygen vacancies induced by doping with trivalent metal (M^{3+}) ions. This category includes the materials which are the focus of this study, yttrium stabilised zirconia (YSZ). A generic Kröger-Vink formula for the doping process is provided below:

$$M_2O_3 + 2\ Zr_{Zr} + O_O \rightarrow 2\ M_{zr}^{'} + V_O^{\cdot\cdot} + 2\ ZrO_2 \qquad \text{(Eq. 2.2.2)}$$

M^{3+} ions occupy Zr^{4+} lattice sites, resulting in an effective defect charge of -1. For every two cation substitutions a charge compensating O^{2-} vacancy is created, thus the ratio of cationic substitutions to oxygen vacancies is 2:1. Significant factors in the stabilising effect of various M^{3+} metals are the ionic radius relative to that of Zr^{4+} and the compatibility of the M_2O_3 material lattice with that of cubic phase zirconia. Materials which are with significant incompatibility based on either factor are likely to have low solubility in zircona and may phase segregate. Materials with a compatible cubic lattice and significant solubility in zirconia include[31, 32] M = Y & Sc, the lanthanides Tb to Yb as well as Lu and Gd. The oxides of these metals adopt a body centred cubic lattice structure with an underpopulated (¼ sites unoccupied) and somewhat disordered cubic oxide anion sublattice. Of the metal oxides listed above, only yttrium is sufficiently abundant and practical for widespread use in manufacture of stabilised zirconia ceramics. In addition, scandium has attracted considerable interest[33-37] as it creates a stabilised zirconia material with higher oxide ionic conductivity than YSZ, potentially suitable for use in SOFCs and other applications. For the creation of extremely stable materials the most practical option, and the subject of study here, is stabilisation with yttria to create YSZ materials.

2.3 YSZ

Yttria Stabilised Zirconia is created by doping zirconia with yttria, Y^{3+} occupies Zr^{4+} sites and for every two such substitutions there is a charge compensating O^{2-} vacancy as illustrated below:

$$Y_2O_3 + 2\ Zr_{Zr} + O_O \rightarrow 2\ Y_{zr}^{'} + V_O^{\cdot\cdot} + 2\ ZrO_2 \qquad \text{(Eq. 2.3.1)}$$

The cubic phase can be stabilised across a wide temperature range and the oxygen vacancies can be highly mobile[38]. The material is also stable under a wide range of chemical conditions[39]. This combination of properties make YSZ materials suited for several high temperature and ionic conduction applications, such as turbine blades, SOFCs, crucibles and active catalyst supports.

The nature of the YSZ material produced will depend on the yttria content. Yttria forms a solid solution with zirconia across a complete range of relative concentrations. At low yttria concentrations (less than 8 mole % yttria) the tetragonal phases may be stable or metastable depending on temperature, at concentrations above 10 mole % yttria the cubic phase is fully stabilised. There is evidence of a third tetragonal phase occurring in the region of 8% yttria with properties very similar to the cubic phase and being indistinguishable by XRD[32,40,41]. This phase is labelled 'New ordered phases' below in a composition / temperature phase diagram reproduced from Bogicevic et al[41].

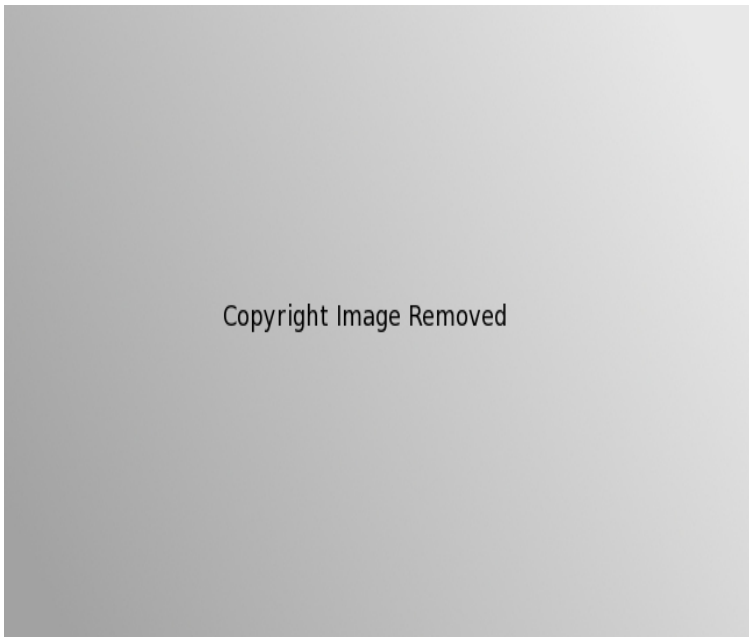

Composition – temperature YSZ phase diagram.

(Fig. 2.3.1)

There has been considerable debate over the favoured relative positioning of yttrium ions and oxygen vacancies within the bulk material, the factors on which the positioning depends and how this may be used to control material properties. Zacate et al[41] conducted modelling work which suggested that the degree of relaxation of the oxygen sublattice surrounding a vacancy depends on the ionic radius of the dopant ion relative to Zr^{4+} with Y^{3+} being sufficiently large to allow only a moderate degree of selective relaxation. But there are contradictory findings, both experimental and computational, as to the ground state relative positions of yttrium ions and vacancies. Studies by Li et al and earlier experimental X-ray studies[42,43] conclude that oxygen vacancies are most stable located as nearest neighbour (NN) adjacent to yttrium ions. However there are a range of other studies, both experimental[41,44] and computational[41,45-47], which conclude that the next nearest neighbour (NNN) sites are preferred. NN and NNN configurations are illustrated in the diagram below, reproduced from Xia et al[48], who conclude that the most favourable arrangement is with yttrium ions adjacent to each other and both NNN relative to the oxygen vacancy. Xia et al use potential based methods within both 3D periodic and Mott-Littleton models to explore the question of relative positioning, as well surface structure and yttrium segregation.

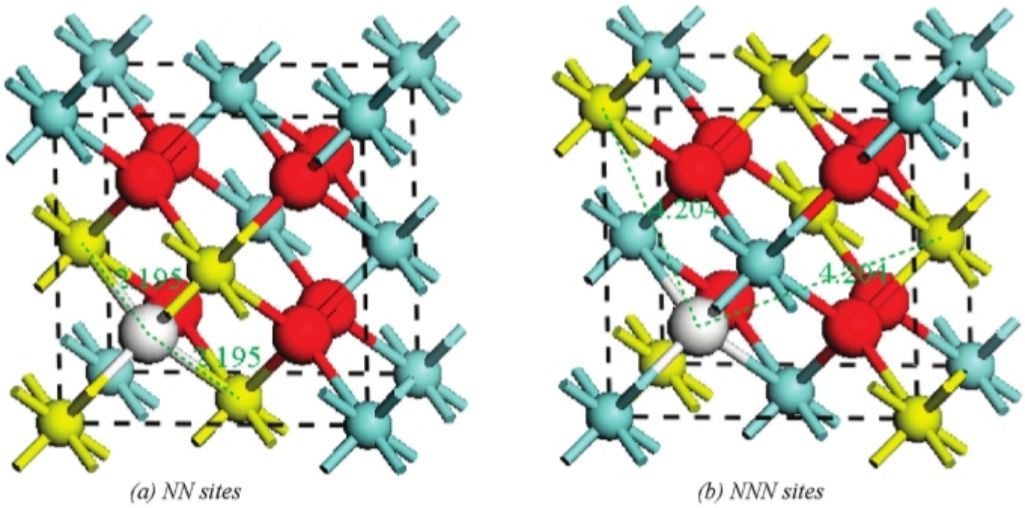

(a) NN sites *(b) NNN sites*

NN and NNN arrangements of Y-V-Y defect clusters in bulk YSZ.
(Fig. 2.3.2)

The question of relative positions is revisited in this study using both interatomic potentials and DFT modelling in chapter 4.

2.4 Oxygen Ion Conductivity

Many of the applications of YSZ materials, especially as an electrolyte in SOFCs, oxygen purification, oxygen sensing and catalytic applications rely on its ability to conduct oxide ions. Factors affecting the material's ability to conduct oxygen ions, the mechanisms of conduction and ways to control this property have been subject to considerable interest, as reviewed throughout this section. This section presents a discussion of the previous work and provides background for further calculations conducted as part of this current study (chapter 5).

Doping with yttrium creates charge compensating oxygen vacancies as discussed in section 2.3. At high temperatures these oxygen vacancies become highly mobile, allowing oxygen to migrate rapidly through the material by a hopping mechanism[49]. Oxygen ions move to fill a neighbouring vacancy, passing between two cations to reach the new location. This process is illustrated in figure below 2.4.1.

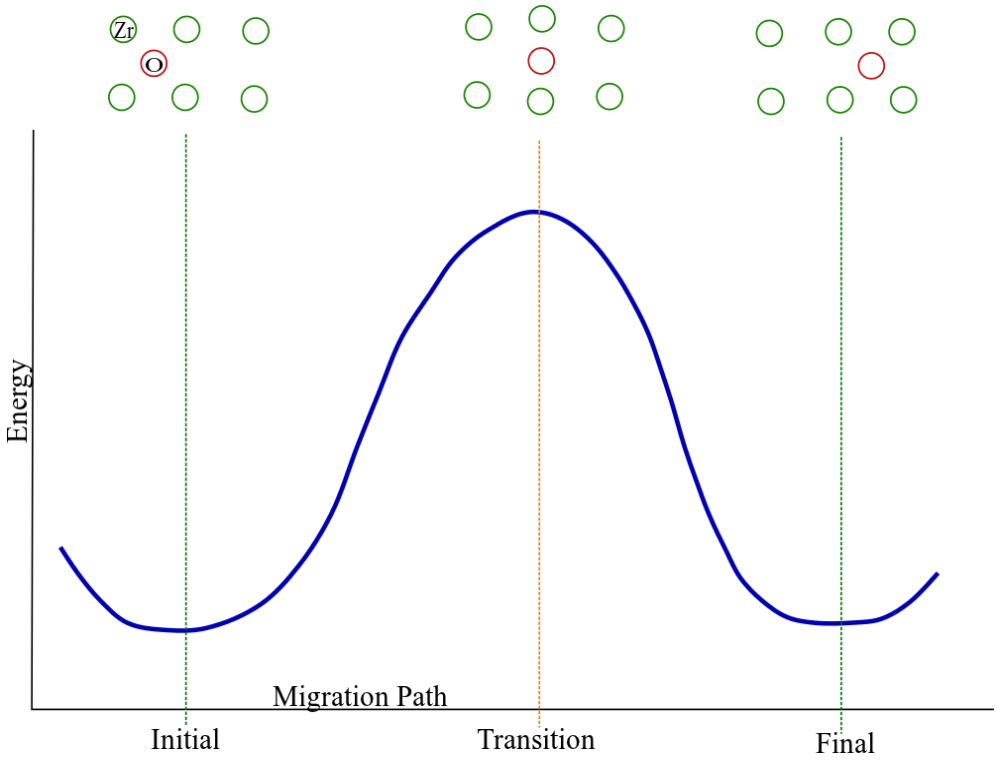

Illustrative energy profile for oxygen ionic conduction through YSZ.
(Fig. 2.4.1)

As can be seen in figure 2.4.1, there is an activation barrier which must be crossed in order to allow the migration to proceed. The factors controlling total migration rate will include the total number of available carriers (mobile vacancies), the mobility of the carriers (activation energy) and the energy available to cross activation barriers (temperature).

The concentration of vacancies is directly proportional to the yttrium doping ratio but the ionic conductivity is not. Indeed several studies[40-52] show that the overall conductivity will increase with yttrium concentration to a maximum at ~8 to 10% yttria before declining again. This relationship can be seen in the figure below, reproduced from Krishnamurthy et al[52].

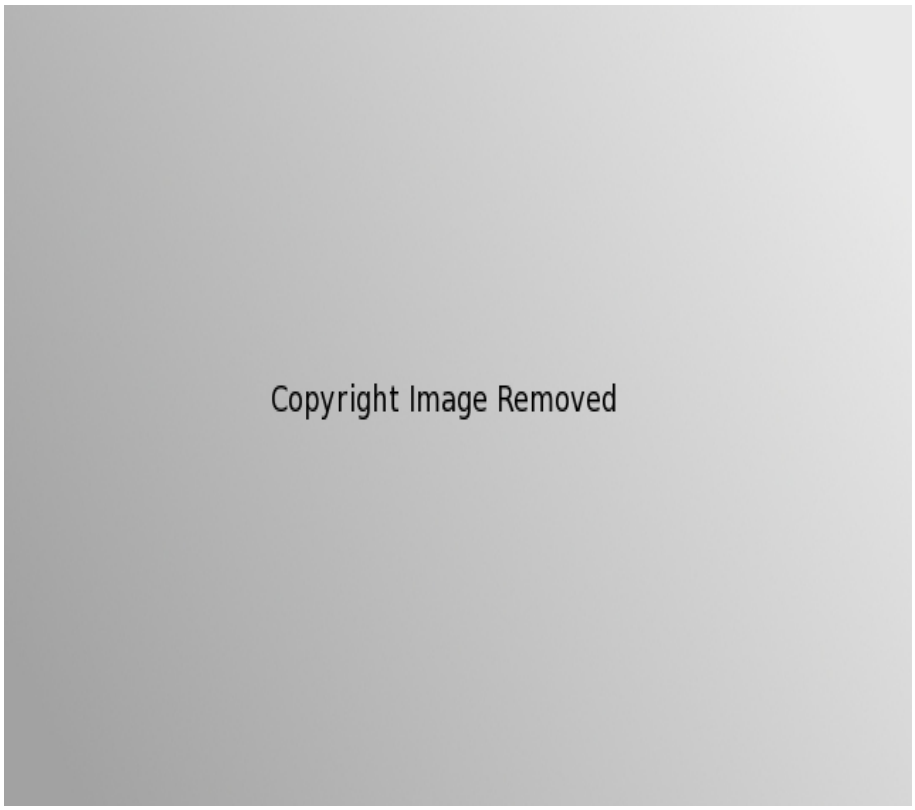

Oxygen conduction rate as function of yttrium concentration at a range of temperatures.

(Fig. 2.4.2)

The initial rise in total ionic conductivity with doping can simply be attributed to the increase in available ionic carriers (vacancies). In order to explain why this trend does not continue it is necessary to consider another factor, the mobility of each carrier. With increasing defect concentrations they are thought to form relatively stable clusters and a reduction in the number of low energy migration pathways through the material[52-56]. In essence, higher levels of yttrium will trap vacancies in ordered clusters dramatically reducing their ability to migrate.

The temperature dependence is fairly straight forward to explain, at higher temperatures a higher proportion of the oxygen ions with a neighbouring vacancy will have sufficient energy to cross the activation barrier within a given time period. The lattice will also become more flexible allowing the migrating ion to pass between neighbouring cations with greater ease as the surrounding lattice dynamically distorts. Temperature dependence can also be seen in Fig. 2.4.2. above.

One factor which may play a significant role in determining the migration rate in some situations, but which has received only limited attention, is surface proximity and morphology. The surface of a material will differ in geometry, coordination numbers and energetics from the bulk lattice. Surface effects on migration may be significant when considering nano-particles, grain boundaries, thin films, interfaces with other materials and surface limited processes such as catalysis. For example, there has been significant controversy over the physical origins of an extraordinarily high conductivity observed at the boundary between YSZ and strontium titanate[57-59].

In order to understand the catalytic interactions and other properties of YSZ materials a study of dopant and surface effects on ionic conduction, geometry and catalytic properties has been conducted. Both DFT and interatomic potentials are employed as part of this work, the results are reported in later chapters.

2.5 Cubic YSZ Surfaces

The surface geometry and features of zirconia materials are crucial in its role in catalysis and other applications. This study is primarily concerned with the stabilised cubic phase of the material. Presented below is an overview of previous studies of relevance to understanding catalytic behaviours of cubic stabilised zirconia surfaces.

2.5.1 Surface Geometries

The cubic YSZ structure contains several inequivalent planes. Determining which of these are likely to be surfaces of catalytic importance is required before surface features and behaviour can be investigated.

Models have been constructed for the (011) and (111) surfaces of cubic YSZ. Work based on both interatomic potentials[60] and electronic structure[61,62] methods has been reported and achieve good agreement as to the relative stabilities of the (111) and (011) surfaces. The (310) surface has been shown using interatomic potentials methods to require significant rearrangement of the structure and is not

energetically favourable when compared to the (111) surface[60]. The (111) surface maintains a relatively high coordination number of seven for zirconium ions and is terminated with protruding three-coordinate oxygen ions. The (011) surface forces zirconium ions into six-coordinate sites resulting is a less thermodynamically favourable arrangement than the (111) surface. Electronic structure studies suggest a greater covalent contribution to the interactions between the lower coordinated surface ions.

2.5.2 Surface Dopant Behaviour

The behaviour of dopant ions and dopant induced defects in the bulk phase has been discussed in section 2.3. Such dopant and defect behaviour must also be considered for the special case of surfaces. The predominant surfaces of the material in the conditions which are the focus of this study are discussed in section 2.5.1 and those considered here are primarily the (111) terrace and step geometries.[48]

The relative arrangements of yttrium ions, their charge compensating oxygen vacancies and the surface of the material must be considered and understood in order to construct accurate models of the catalytically active surfaces of the materials. There has been extensive work conducted by Xia et al using interatomic potentials[48] to describe possible near-surface arrangements of yttrium and oxygen vacancies including a list of orientations and arrangements of surface defect clusters and their modelled energies. Xia et al also report DFT work examining surface defect cluster arrangements and their role in creating surface oxygen species[63]. The arrangements reported by Xia et al are derived by sampling a subset of the defect configurations possible in the material, results of an exhaustive sampling of low concentration defects in the bulk and at the surface are reported in subsequent chapters, as are the interactions of YSZ surface sites with oxygen, water, carbon dioxide, hydrogen and most importantly methane.

Another effect of considerable importance is the potential for the near surface region to be, on average, richer or poorer in dopants and defects than the bulk. There is some evidence that yttrium and accompanying vacancies will accumulate at a

higher relative concentration in the near surface region, i.e. they 'surface segregate'. This may be at least partially driven by the lower coordination zirconium environments at the surface being preferentially occupied by the less charged yttrium ion relative to the bulk. A wide range of evidence to support yttrium surface segregation in cubic YSZ is provided by both theoretical and experimental work.

Experimental evidence of yttrium surface segregation is reported based upon ion scattering[64,65] and XPS[66,67] (X-ray photo-electron spectroscopy) studies, which are sensitive to ion types at the surface of the material. The studies examine materials with different yttrium concentrations, from two mole percent in the work of Morterra et al[66] to materials with greater than ten percent yttrium as in the work of de Riddler et al[64,65]. There is some evidence to suggest that once a minimum concentration of yttrium that is present the surface concentration may be independent of that of the bulk. The surface will be yttrium enriched until a limit is reached at which point no further segregation will occur[68]. Theoretical evidence in support of yttrium segregation is provided from electronic structure models of various YSZ surfaces[69-71]. There is a strong consensus that yttrium will surface segregate in the (111) surfaces but less support for segregation in the (110) surfaces. The depth to which surface segregation will extend and the precise extent to which the surface will be yttrium enriched remain open questions. However, Xia et al report models predicting surface segregation at a depth of up to 5Å from the surface[48].

2.6 Potentially Active Surface Species and Sites

The surfaces of YSZ materials have sites which may be catalytically active or which may stabilise or create other active species. Some potential sites are intrinsic to the material itself. Some examples, complete with visualisations, are provided below.

The defect free oxygen terminated zirconia (111) surface exposes two ionic types, zirconium and oxygen. They are formally present as Zr^{4+} and O^{2-}.

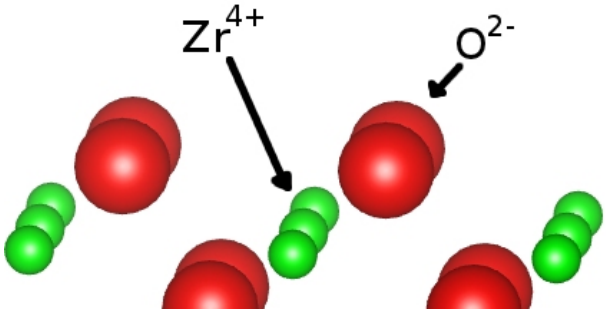

Zirconia surface ions, red is oxygen, green zirconium.

(Fig. 2.6.1)

As has previously been discussed the electronic properties of systems, especially at the surface, are not adequately characterised by assigning formal charges. Their precise electronic state is crucial to any interactions with substrate molecules in catalytic environments.

The doped material presents additional surface features which may be of significance. The presence of yttrium ions and oxygen vacancies in the surface region will be significant in itself and will also alter the electronic state of neighbouring ions.

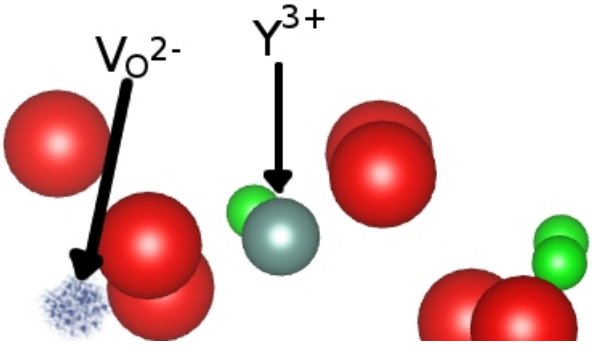

YSZ surface features, red is oxygen, green zirconium, blue-grey yttrium.

(Fig. 2.6.2)

As can be seen in Fig. 2.6.2, there will also be lower coordinate ions adjacent to a vacancy. The vacancies are known[63] to be able to stabilise reactive oxygen species such as superoxide (O_2^-). The diagram in figure 2.6.3 shows examples of surface oxygen species and their calculated energies as reported by Xia et al[63].

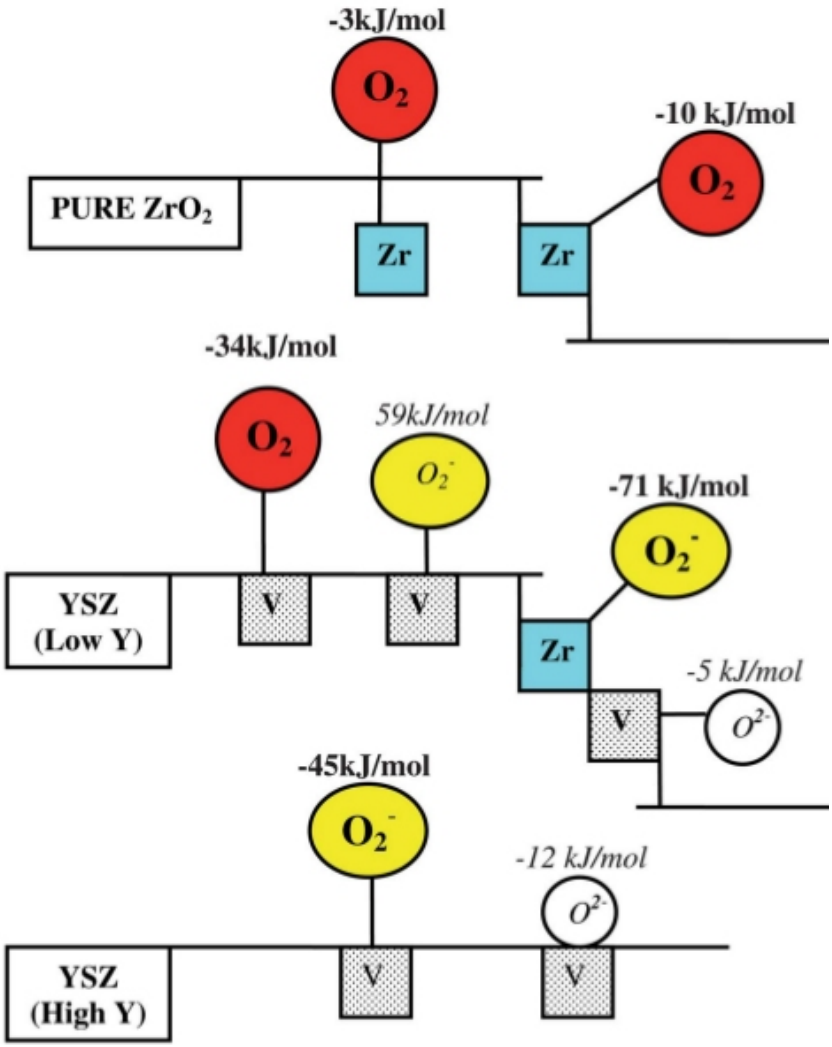

Graphical summary of oxygen adsorption over zirconia materials by Xia et al[63]. (Fig. 2.6.3)

The ability to stabilise reactive oxygen species has been studied experimentally through EPR studies[72] and in great detail through computational methods by Xia et al[63]. A large range of surface – oxygen interactions were modelled, enabling the latter authors to report findings on the oxygen species (some highly reduced), their energetics and likely adsorption pathways on the (111) terrace and stepped surfaces of pure zirconia and YSZ with varying yttrium concentrations. They conclude that oxygen vacancies provide an adsorption site for oxygen and that low coordinate zirconium ions can attract reduced oxygen species.

One limitation of the previous work is the reliance on GGA DFT (see chapter 3) to represent electronic structure. DFT has a well known self-interaction error and will tend to excessively de-localise the unpaired electrons in reactive oxygen species. For this reason hybrid functional DFT is applied in some cases here to investigate surface oxygen interactions (reported in chapter 6).

Other reactive species of importance to the partial oxidation of methane may be generated or stabilised at surface vacancies. Therefore, interaction of other potential oxidants with the surface vacancies will be a focus of this research (for example, chapter 6 reports investigation of the interactions between water and surface vacancies).

2.7 YSZ in Catalysis

YSZ has long been used in catalytic applications as a support material owing to the suitability of its physical, thermal and chemical properties and stability. YSZ typically supports other catalytically active components such as metallic particles. Supports may be formed by pressing crystalline powders of controlled grain size into pellets of a morphology designed to control surface area, flow rate and back pressure in a reactor as is common to many other metal oxide support materials such as alumina. Examples of metals frequently used include nickel and platinum group metals. The bare YSZ material has also been shown to be catalytically active for partial oxidation of methane. Zhu et al[68] presented the most complete exploration of its activity using an experimental system consisting of two catalytic beds of YSZ materials. The process of methane reforming in general, and specifically over YSZ materials was discussed in greater detail in chapter 1.

2.8 Summary

Zirconia materials can exist in several phases, determined by pressure, temperature and doping. The cubic phase can be stabilised across a very wide temperature range by doping with various other metal oxides.

YSZ is created when yttrium ions are present on the zirconium sites and are

charge compensated by oxygen vacancies in a 2:1 ratio. There is good evidence to suggest that the most stable bulk arrangement of the defects in in next nearest neighbour relationships.

Oxygen ions can be conducted through the lattice of cubic YSZ by a hopping mechanism between neighbouring oxygen sites. The rate of oxygen conduction is a function of temperature and yttrium concentration, with yttrium increasing the number of vacancies but also trapping them at higher concentrations.

The most stable surface of cubic zirconia and YSZ is a 111 oxygen terminated terrace. There is strong evidence to suggest that the surface region will be yttrium enriched relative to the bulk of the material at low yttrium concentrations.

The surface features of YSZ will determine its catalytic activity. The surface is able to stabilise molecular oxygen and, at surface oxygen vacancy sites, reduced oxygen species.

References

[1] L. Fletcher, *Mineralogy Mag. and J. Mineralogical Soc.* 149-161, **1892**.

[2] R. Lumpkin, *J. Nuclear Materials.* 247, 206-217, **1999**.

[3] R. Lavinski, "http://www.mindat.org/photo-37769.html" retrieved **2012**. Reproduction permitted by CC license.

[4] A. Drabińska, K. Grodecki, W. Strupiński, R. Bożek, K. Korona, A. Wysmołek, R. Stępniewski, J. Baranowski, *Phys. Rev. B.* 81, **2010**.

[5] T. Bayanova, *Petrology.* 14, 187-200, **2006**.

[6] P. Bouvier, E. Djurado, G. Lucazeau, T. Le Bihan, *Phys. Rev. B.* 62, **2000.**

[7] M. Wilson, U. Schönberger, M. Finnis, *Phys. Rev. B*. 54, 9147, **1996 .**

[8] A. Christensen, E. Carter, *Phys. Rev. B*. 58, 8050, **1998**.

[9] L. Boyer, B. Klein, *J. Am. Ceram. Soc.* 68, **1985**.

[10] R. Cohen, M. Mehl, L. Boyer, *Physica B.* 150, 1-9, **1988**.

[11] A. Cormack, S. Parker, *J. Am. Ceram. Soc.* 73, **1990**.

[12] A. Dwivedi, A. Cormack, *Philosoph. Mag. A.* 61, **1990**.

[13] F. Shimojo, T. Okabe, F. Tachibana, M. Kobayashi, H. Okazaki, *J. Phys. Soc. Japan.* 61, 2848, **1992**.

[14] F. Shimojo, H. Okazaki, *J. Phys. Soc. Japan.* 61, 4106, **1992**.

[15] X. Li, B. Hafskjold, *J. Phys. Cond. Matter.* 7, 1255, **1995**.

[16] A. Mirgorodsky, M. Smirnov, P. Quintard, *Phys. Rev. B*. 55, 19, **1997**.

[17] M. Finnis, A. Paxton, M. Methfessel, M. van Schilfgaarde, *Phys. Rev. Lett.* 81, 23, **1998**.

[18] E. Stefanovich, A. Shluger, C.R.A. Catlow, *Phys. Rev. B.* 49, 11560, **1994**.

[19] R. Orlando, C. Pisani, C. Poetti, E. Stefanovich, *Phys. Rev. B.* 45, 596, **1992.**

[20] B. Králik, E. Chang, S. Louie, *Phys. Rev. B*. 43, 7027, **1998**.

[21] G. Jomard, T. Petit, A. Pasturel, L. Magaud, G. Kresse, J. Hafner, *Phys. Rev. B*. 59, 4044, **1999**.

[22] G. Stapper, M. Bernasconi. N. Nicoloso, M. Parrinello, *Phys. Rev. B*. 59, 797, **1999**.

[23] J. Van Vechten, *Phys. Rev.* 187, 1007, **1969** .

[24] J. Phillips, *Phys. Today*. 23, **1970**.

[25] A. Garcia, M. Cohen, *Phys. Rev. B.* 47, 4215, **1993**.

[26] P. Duwez, F. Odell, F. Brown, *J. Am. Ceram. Soc*. 35, 107, **1952**.

[27] F. Kroger, H. Vink, *Solid State Phys.* 3, 273, **1956**.

[28] N. Arul-Dhas, K. Patil, *J. Mat. Sci. Lett.* 23, 1844, **1993**.

[29] G. Balducci, J. Kaspar, P. Fornasiero, M. Graziani, M. S. Islam, J. D. Gale, *J. Phys. Chem. B.* 101, 1750, **1997**.

[30] M. Yashima, K. Morimoto, N. Ishizawa, M. Yoshimura, *J. Am. Ceram. Soc*. 76, 1745, **1993** .

[31] M. Zinkevich, *Progr. Mater. Sci.* 52, 597, **2007**.

[32] M. Yashima, H. Takanhashi, K. Ohtake, T. Hirose. M. Kakihana, H. Arashi, M. Yoshimura. *J. Am. Ceram. Soc.* 57, 289, **1996** .

[33] T. Raming, L. Winnubst, H. Verweij, *J. Mater. Chem.* 12, 3705, **2002**.

[34] I. Kobayashi, H. Anderson, Y. Mizutani, K. Ukai, *Solid State Ionics.* 152, 431, **2002**.

[35] I. Kobayashi, I. Takahashi, M. Shiono, M. Dokiya, *Solid State Ionics.* 152, 591, **2002**.

[36] Z Cai, T. Lan, S. Wang, M. Dokiya,. *Solid State Ionics.* 152, 583, **2002**.

[37] V. Srdić, M. Winterer, *Chem, Mater.* 15, 2668, **2003**.

[38] A. Predith, G. Ceder, C. Wolverton, K. Persson, T. Mueller, *Phys. Rev. B.* 77, 144104, **2008**.

[39] T. Etsell, S. Flengas, *Chem. Rev.* 70, 339, **1970**.

[40] V. Stubican, J. Hellmann, S. Ray, *Mat. Sci.* 10, 257, **1982** .

[41] A. Bogicevic, C. Wolverton, G. Crosbie, E. Stechel, *Phys. Rev. B.* 64, **2001**.

[42] M. Zacate, L. Minervini, D. Bradfield, R. Grimes, K. Sickafus, *Solid State Ionics*. 128, 243, **2000**.

[43] P. Li, I. Chen, J. Penner-Hahn, *J. Am. Ceram. Soc*. 77, 118, **1994**.

[44] T. Welberry, R. Withers, J. Thompson, B. Butler, *J. Solid State Chem*. 100, 71, **1992**.

[45] C.R.A. Catlow, A. Chadwick, G. Greaves, L. Moroney, *J. Am. Ceram. Soc*. 69, 272, **1986**.

[46] A. Gallardo-Lopez, J. Martinez-Fernandez, A. Dominguez-Rodriguez, *Philos. Mag. A.* 81, 1675, **2001**.

[47] A. Gallardo-Lopez, J. Martinez-Fernandez, A. Dominguez- Rodriguez, *J. Euro. Ceram. Soc*. 22, 2821, **2002**.

[48] X. Xia, R. Oldman, C. R. A. Catlow, *Chem. Mater.* 21, 3576, **2009**.

[49] M. Kilo, C. Argirusis, G. Borchardt, R. Jackson, *Phys. Chem. Chem. Phys.* 5, 2219, **2003**.

[50] A. Ioffe, D. Rutman, S. Karpachov, *Electro. Chem. Acta.* 23, 141, **1978** .

[51] S. Badwal, *Solid State Ionics*. 52, 23, **1992**.

[52] R. Krishnamurthy, Y. Yoon, D. Srolovitz, R. Car, *J. Am. Ceram. Soc*. 87, 1821, **2004**.

[53] M. Khan, M.S. Islam, D. Bates, *J. Mater. Chem*. 8, 2299, **1998**.

[54] M. Kilo, R. Jackson, G. Borshardt, *Philos. Mag.* 83, 3309, **2003**.

[55] V. Zavodinsky, *Phys. Solid State.* 46, 453, **2004**.

[56] A. Murray, G. Murch, C.R.A. Catlow, *Solid State Ionics.* 18, 196, **1986**.

[57] J. Garcia-Barriocanal, A. Rivera-Calzada, M. Varela, Z. Sefrioui, E. Iborra, C. Leon, S. Pennycook, J. Santamarial, *Science*. 321, 676, **2008**.

[58] X. Guo, *Science.* 324, 465, **2009**.

[59] J. Garcia-Barriocanal, A. Rivera-Calzada, M. Varela, Z. Sefrioui, E. Iborra, C. Leon, S. Pennycook, J. Santamarial, *Science*. 324, 465b, **2009**.

[60] G. Balducci, J. Kaspar, P. Fornasiero, M. Graziani, M.S. Islam, J. *Phys. Chem. B.* 102, 557, **1998**.

[61] S. Gernard, F. Cora, C.R.A. Catlow, *J. Phys. Chem. B.* 103, 10158, **1999**.

[62] A. Bernasik, K. Kowalski, A. Sadowski, *J. Phys. Chem. Solids.* 63, 233, **2002**.

[63] X. Xia, R. Oldman, C.R.A. Catlow, *J. Mater. Chem.* 22, 8594 , **2012**.

[64] M. de Ridder, H. Brongersma, U. Kreissig, *Solid State Ionics*. 158, 67, **2003**.

[65] M. de Ridder, R. G. van Welzenis, H. Brongersma, U. Kreissig, *Solid State Ionics*. 156, 255, **2003**.

[66] C. Morterra, G. Cerrato, L. Ferroni, L. Montanara, *Mat. Chem. Phys.* 37, 243, **1994**.

[67] A. Bernasik, K. Kowalski, A. Sadowski, *J. Phys. Chem. Solids*. 63, 233, **2002**.

[68] J. Zhu, J. G. van Ommen, J. Henny, M. Bouwmeester, L. J. Lefferts, *J. Catal*. 33, 434, **2005**.

[69] A. Eichler, G. Kresse, *Phys. Rev. B*. 69, **2004** .

[70] G. Ballabio, M. Bernasconi, F. Pietrucci, S. Serra. *Phys. Rev. B*. 70, **2004**.

[71] C. Stanek, R. Grimes, M. Rushton, K. McClellan, R. Rawlings, *Philos. Mag. Lett.* 85, 445, **2006**.

[72] M. Anpo, M. Che, B. Fubini, E. Garrone, E. Giamello, M. Paganini, *Top. Catal*. 8, 189, **1999**

Chapter 3. Computational Techniques

Computational modelling methods, when carefully applied, can offer information and understanding of systems which would otherwise not be easily available. The insights offered by modelling can complement, extend and guide experimental work, while conversely experimental evidence is necessary in guiding the construction of models and assessing their validity. Modelling allows materials to be described and analysed on size, time scales and experimental conditions not accessible via experimental techniques and offers the researcher the freedom to construct model systems of precise configuration. The potential of modelling has grown considerably in recent time as improvements in computer hardware, physical descriptions and software techniques have made much more sophisticated model systems accessible. The computational techniques used in this research fall broadly in to three categories: physical models (interatomic potentials and quantum mechanical), optimisation strategies and analysis methods as discussed below.

3.1 interatomic Potentials

In order to calculate internal energy of a system exactly it would be necessary to calculate many body interactions for all entities present, but in reality this is an implausible task for non-trivial systems and various approximations must be made. interatomic potentials are sets of parametrised functions which attempt to approximate the interactions between atomic components of a target system with a useful level of accuracy.

In applying interatomic potentials the electrons are amalgamated into the atoms and not treated independently. This greatly reduces the complexity and number of entities which must be contemplated, but does prevent any explicitly electronic processes from being modelled, such as bond making and breaking in chemical reactivity.

Secondly, the interactions which must be considered form an expansion from self interactions, through two body and three body interactions up to an all body interaction as shown below:

$$U = \sum_{i=1}^{N} U_i + \frac{1}{2}\sum_{i=1}^{N}\sum_{j=1}^{N} U_{ij} + \frac{1}{6}\sum_{i=1}^{N}\sum_{j=1}^{N}\sum_{k=1}^{N} U_{ijk} + \ldots,$$

(Eq. 3.1.1)

This becomes computationally intractable for all but the smallest systems and must be terminated at an order which is usually significantly lower than the number of entities in the system. The excluded contributions are are generally very small, and decrease as the order grows. The interactions between entities can be broadly grouped in to those which decay rapidly over distance (short range) and slowly (long range).

The primary long range potential is the electrostatic (Coulomb) interaction. The two-body coulomb interaction is expressed below, where U is potential energy, q is charge on an entity and r is separation distance between entities:

$$U_{ij} = q_i q_j / 4\pi\varepsilon_0 r$$

(Eq. 3.1.2)

Coulomb interactions can be difficult to evaluate since the number of interacting entities grows ($4\pi r^2$) faster than the interaction energy decreases (1/r), which means that the interaction energy density can increase with distance. The most common solution to this problem and that used in the GULP code is the method of summation, known as an Ewald sum[1].

The Ewald sum relies on separating real and reciprocal space terms, resulting in two expressions which both converge rapidly in their respective spaces. A self-interaction term must also be introduced, and the sum of the three terms is the total electrostatic interaction energy. The expressions below are reproduced from Gale and Rohl[2]. Here q is the charge on an ion, G is the reciprocal lattice vector, V the unit cell volume and η is a parameter controlling the division between real and reciprocal space functions.:

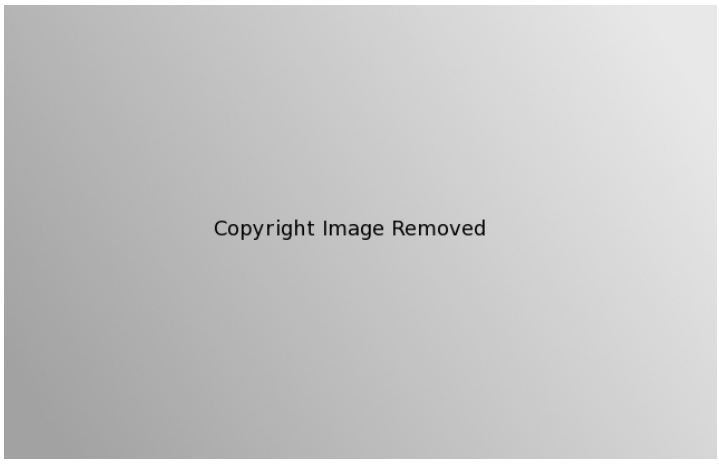

(Eqs. 3.1.3a – 3.1.3d)

A value for η is chosen to minimise the number of terms to be evaluated, taking the relative complexity of real or reciprocal space evaluation into account. The cut-off in both spaces is set such that the interaction energy will be converged to a given accuracy. The approach outlined above is described by Jackson and Catlow[3].

Unlike Coulomb interactions, the attractive dispersion interactions are convergent. However, this does not mean they converge rapidly and an Ewald sum like process[4] is often used to accelerate convergence of dispersion forces. Dispersion energy can be expressed as a series of increasing inverse powers of distance, representing first instantaneous dipole interactions and then higher order dipole interactions as shown below.

$$-C_6/r^6 - C_8/r^8 - C_{10}/r^{10} - \ldots$$

(Eq. 3.1.4)

This series must be truncated at some point and it is usually sufficient to consider only the first term.

The final term of the expression for total energy of a two body Born model[5] is a short range repulsion due to the effects of Pauli exclusion on overlapping electron clouds. This is typically expressed in combination with the dispersion term in a combined interatomic potential. Many such potential forms are available and are listed in the following table (table 3.1.1) by Gale[6]:

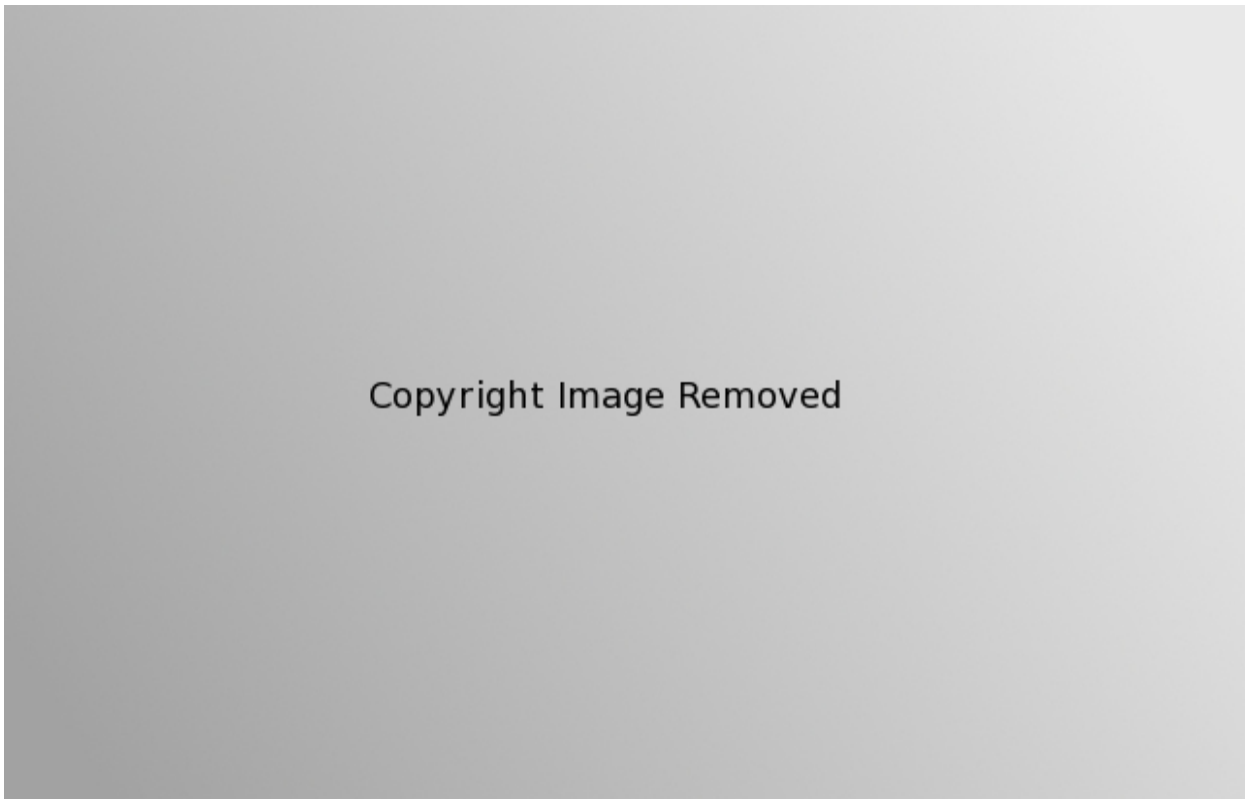

Potential forms available in the GULP software package.

(Tab. 3.1.1)

In this project, Buckingham potentials were used to model interactions between the lattice species. The Buckingham potential expresses the short range repulsive term as an exponent[5], as at larger distances electron density falls exponentially with distance from the nucleus:

$$A\ exp(-r/\rho)$$

Where A and ρ are constants and r is the interatomic separation.

(Eq. 3.1.5)

The short range repulsive term is combined with the truncated dispersion interaction (as discussed before) in the Buckingham potential:

$$U_{(Buc)ij} = A\ exp\ (-r_{ij} / \rho) - C_6 / r_{ij}^6$$

(Eq. 3.1.6)

When plotted as energy against distance the total non-Coulombic interaction predicted by the Buckingham potential is as shown below, the x-axis represents distance (r_{ij}) and the y-axis is the potential energy ($U_{(Buc.)ij}$).:

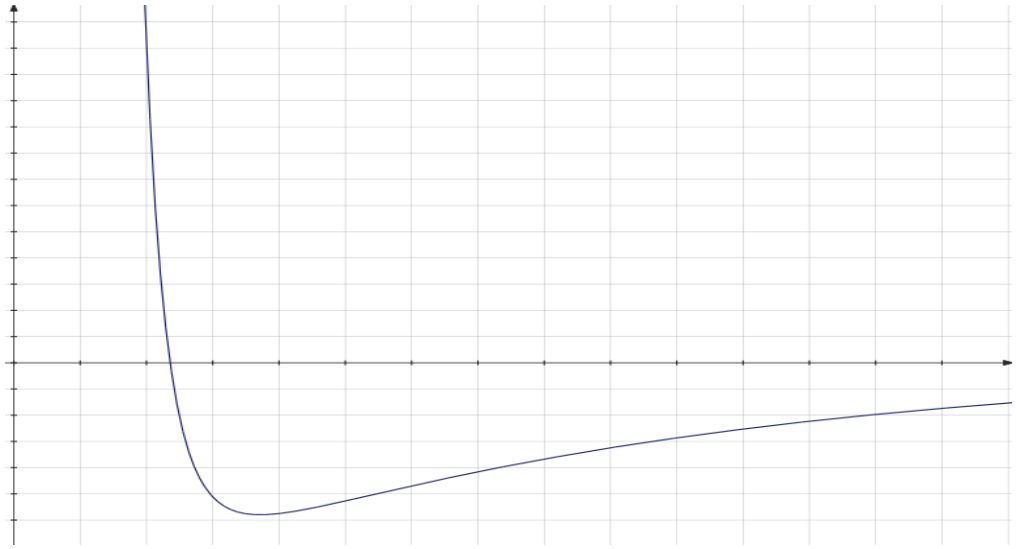

Illustrative plot of the Buckingham potential as a function of distance.
(Fig. 3.1.1)

As can be seen, the attractive dispersion interactions dominate at larger distances whereas at shorter distances the repulsive interactions dominate as the electron clouds overlap and repulsion rapidly increases.

The complete model requires a number of numerical parameters to be specified for each entity present in the model. The electrostatic term requires the charge on each entity (atom, core or shell). The Buckingham potential requires the quantities A, ρ and C to be specified as well as a cut-off distance to be specified for each pair of entities present. At the cut-off the potential should not be abruptly and discontinuously terminated as such sharp discontinuities can lead to unrealistic and undesired behaviour of the model. To avoid sharp discontinuities a taper function can be applied to bring the potential smoothly to zero before terminating it.

The parameters discussed above can be derived in a number of ways[7,8]; ab-initio calculations can be performed to derive the potential energy surface which parameters can then be fitted to or they may be fitted to data from experimental observations. Semi-empirical parameters can also be produced by starting with a

model based on electronic structure calculations and refining to fit experimental data before verifying against other experimental data not used in their construction.

3.1.1 Shell Model

Using interatomic potentials ionic species can be represented either as complete single entities or as a combination of “core” and “shell”[9]. The core is a point entity, representing the nucleus and core electrons and with the appropriate charge. The shell is also centred on a point, but represents the valance electron cloud surrounding the core and is linked to the core by a harmonic 'spring' function. The core / shell concept is illustrated below:

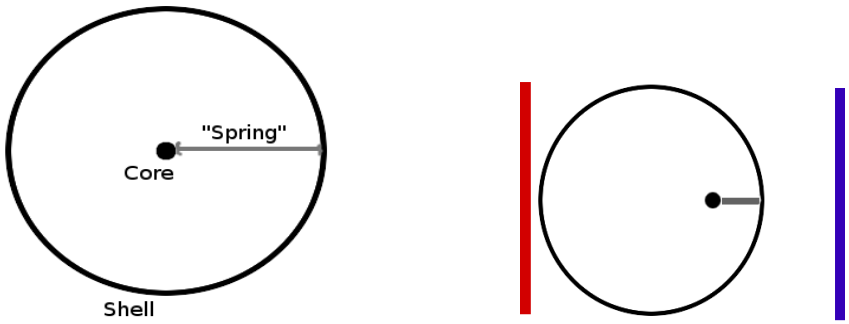

Illustration of the core-shell model (left), shell displaced by electrostatic field (right).

(Fig. 3.1.2)

This separation of core and shell models polarisation[10] which occurs as an electron cloud is distorted by the effects of surrounding species, the diagram on the right shows the effects of an external field mimicking this by displacing the shell.

3.1.2 Potential Parameters

The parameters used in this study are taken from the work of Dwivedi and Cormack[11]. The parameters were produced by empirical fitting, using a least squares method to maximise agreement between experimental and calculated crystal properties. The oxygen – oxygen interaction was derived in earlier work by Catlow[12]. Methods used to derive such potentials are discussed in the work of Lewis and Catlow[13]. The parameters applied are tabulated below, including the partial charges and spring constants used in the shell model:

Charges

Entity	Charge
Y atom	3.000
Zr core	2.650
Zr shell	1.350
O core	0.077
O shell	-2.077

Spring Constant

Species	k (ev Å^{-2})
O^{2-}	27.290
Zr^{4+}	169.617

Buckingham

Entity	A (eV)	ρ (Å)	C (ev Å^{-6})	Cut-off (Å)
Y atom – O shell	1345.100	0.3491	0.00	10
Zr shell – O shell	985.869	0.3760	0.00	10
O shell – O shell	22764.000	0.1490	27.88	12

Interatomic potential parameters used throughout this thesis.

(Tab. 3.1.2)

It may be noticed in the table above that the shell model was not included for yttrium species owing to a lack of suitable parameters in the literature. It is held that this lack of a polarisable shell should have a minimal impact on any calculations performed since the Y^{3+}ion does not have an easily polarised electron cloud.

3.2 Electronic Structure Methods

Electronic structure or QM (quantum mechanical) methods aim to characterise model systems on the basis of an approximate solution to the Schrödinger equation. The time independent form of the Schrödinger equation is given below[14].

$$\hat{H}\Psi = E\Psi$$

(Eq. 3.2.1)

In the above equation Ψ is the wave function, E is the total ground state energy of the system and $\hat{H}$ is the Hamiltonian energy operator. $\hat{H}$ can be divided into kinetic and potential operator components as shown below. Where m = mass, $\hbar = h/2\pi$ (h = Planks' constant), $V(r)$ is the potential distribution:

$$\hat{H} = -\frac{\hbar}{2}\sum \frac{1}{\mathrm{m}_i}\nabla_i^2 + V(r)$$

(Eq. 3.2.2)

The contributions can be further separated into various electronic and nuclear components as follows:

$$\hat{H} = K_N + K_E + V_{NN} + V_{NE} + V_{EE}$$

Where K is kinetic energy, V is potential, N is nuclear, E is electronic.

(Eq. 3.2.3)

An exact solution of the Schrödinger equation would be a perfect representation of the ground state wave function and energy, with the square of the wave function being the ground state electron density distribution for the system. Unfortunately the exact solution is computationally inaccessible due to the lack of an analytical solution of the electron interactions, necessitating further assumptions and approximations for calculations on non-trivial systems.

3.2.1 Born-Oppenheimer Approximation

The Schrödinger equation may be somewhat simplified by treating the electronic and nuclear wave functions as independent[15]. This assumption is based on the relative masses and hence dynamics of electrons and nuclei imparting a time scale separation. Nuclear positions are treated as static with zero kinetic energy and electrons are assumed to arrange instantaneously under the influence of the interactions between each-other and the static potential field of the nuclei. The Born-Oppenheimer approximation may be applied to the energy operator as follows; where K is a kinetic contribution and V a potential contribution, $_N$ and $_E$ denote effects arising due to nuclear or electronic properties respectively:

$$\hat{H} = (K_N + V_{NN}) + (K_E + V_{NE} + V_{EE})$$

(Eq. 3.2.4)

This assumption holds relatively well for the majority of systems, only exposing significant shortcomings where species with extremely light nuclei are handled or where model systems are in an excited state. Despite this simplification, the electron – electron interactions remain inaccessible to exact solution other than for one electron systems, thus further assumptions and approximations are necessary.

3.2.2 Hartree-Fock (HF) Theory

A further simplification, made by Hartree nearly a century ago[16,17], is to express the n electron wave function as a product of single electron wave functions. Hartree's model yields a solvable equation which can be used to give a set of spin orbitals, the 'Hartree product' wave function:

$$\Psi(x_1 \ldots x_n) = \chi_i(x_1)\chi_j(x_2) \ldots \chi_n(x_n)$$

(Eq. 3.2.5)

The energy of the Hartree system may be expressed as follows, where the total energy of the system is simply the sum of independent contributions (E_i):

$$E = \langle\Psi|H|\Psi\rangle = E_i + E_j \ldots + E_n$$

(Eq. 3.2.6)

This model is solved through a selfconsistent field (SCF) approach in which each electron is treated independently, under the influence of the potential of the other electrons (the mean field method). The Schrödinger wave equation is then solved to yield a new wave function and potential field and repeated to reach self consistency. This model does not satisfy the Pauli exclusion principle, that is to say that it does not recognise the way in which electrons are prevented from occupying the same space and spin state i.e. the wave function is not antisymmetric with respect to electron interchange.

In order to take Pauli exclusion in to account an antisymmetric wave function must be constructed. The Slater determinant[18] is the determinant of electrons and spin orbitals in a system and can be used to construct a properly antisymmetric wave function, using which we can minimise the total energy with respect to the orbital coefficients. The Slater determinant is written as:

$$\varphi_{slater} = 1/\sqrt{n}\ det\ \{\chi_i(x_1)\chi_j(x_2) \ldots \chi_n(x_n)\ \} \quad \text{(Eq. 3.2.7)}$$

This method prevents double occupation of a spin orbital since the wave function sums to zero if the exclusion principle is violated. The combination of the Hartree treatment of electrons with antisymmetric wave function construction leads to two integral terms of HF (HartreeFock) energy, firstly the Coulomb integral:

$$C_{ij} = \iint \chi_i(x_1)\chi_j^*(x_2)\ 1/\tau_{12}\ \chi_i(x_1)\chi_j^*(x_2)\ d\tau_1\ d\tau_2 \quad \text{(Eq. 3.2.8)}$$

and secondly, the exchange integral:

$$X_{ij} = \iint \chi_i(x_1)\chi_j^*(x_2)\ 1/\tau_{12}\ \chi_j(x_1)\chi_i^*(x_2)\ d\tau_1\ d\tau_2 \quad \text{(Eq. 3.2.9)}$$

HF theory allows reasonably accurate estimates of bonding and geometry in many systems and has been widely used. HF is also an important element in some hybrid DFT functionals. However, HF is not suitable for direct calculation of some properties of many systems as a result of its assumptions and approximations. HF does not allow any representation of the correlation of electron movements, instead treating electrons as moving independently under the influence of the average Coulombic repulsion. The absent correlation effects can be extremely significant in some systems, such as those with localised elections. HF will also incorrectly describe systems with degenerate electron states, populating one state fully rather than giving them equal occupation.

Post-HF methods which build upon the HF model by adding a representation of correlation. Such methods potentially allow very accurate descriptions of

electronic systems. Example methods include the coupled cluster technique and Møller–Plesset perturbation theory. These methods are generally extremely computationally expensive and are not employed in the research reported in this thesis.

3.3 Density Functional Theory (DFT)

For a system of interacting electrons the ground state energy is impossible to calculate exactly due to the intractable problem of many-electron interactions. However, DFT provides a methodology and a set of assumptions which allow relatively quick calculations to be made whilst preserving sufficient accuracy in many applications so allowing it to become the most widely used electronic structure method in computational chemistry applications. In DFT the energy of a system of electrons is expressed as a functional of electron density distribution.

The obvious predecessor of DFT is Thomas-Fermi theory[19,20], which allows a model of the kinetic, exchange and correlation of a system of electrons to be constructed based on the expressions for these quantities in a homogeneous electron gas. By approximating electron – electron interactions as classical Coulomb potentials it is possible to express the kinetic energy as a function of local density.

Assuming a homogeneous electron gas the total kinetic energy is given by[21]:

$$T[\rho(r)] = 3/10\ (3\pi^2)^{3/2} \int \rho^{5/3}(r)dr \qquad \text{(Eq. 3.3.1)}$$

The function for kinetic energy is derived from the relationships between electron density (ρ), Fermi energy (ε_F) and kinetic energy for a homogeneous electron gas (T):

$$T = 3\rho\varepsilon_F / 5 \qquad \text{(Eq. 3.3.2)}$$

$$\rho = (1/3\pi^2)(2m/\hbar^2)^{3/2}\, \varepsilon_F^{3/2} \qquad \text{(Eq. 3.3.3)}$$

By then treating a globally inhomogeneous system as locally homogeneous and

considering classical potential interactions between electrons and between electrons and nuclei it is possible to arrive at the total ground state energy for a system with in the limits of Thomas-Fermi theory:

$$E_{TF}[\rho(r)] = 3/10\,(3\pi^2)^{3/2} \int \rho^{5/3}(r)dr + \int v(r)\rho(r)dr + \tfrac{1}{2} \iint (\rho(r)\rho(r')) / (|r-r'|)\, drdr' \quad \text{(Eq. 3.3.4)}$$

Thomas-Fermi theory allows an approximation of the energy of a system, including a representation of kinetic energy, electron-electron and electron-nuclear interactions as classical potentials. An exchange contribution, developed by Dirac, may be added to further improve the representation in Thomas-Fermi-Dirac theory. However, there are limitations inherent in the assumptions of the model. Significant errors can be expected in the representations of kinetic and exchange energies and there is no representation of electron correlation in this model of electronic systems. To be of significant use in the study of systems of interest further improvements were required.

Density Functional Theory is based upon two key theorems from the work of Hoenberg and Kohn[22]:

Firstly, it is impossible for two external potentials (arrangements of nuclei) which differ by more than an additive constant to give rise to the same ground state electron density distribution. The external potential $V(r)_{ext}$ and electron density distribution σ(r) may each be uniquely determined by the other.

Secondly, the ground state energy for a given external potential distribution is obtained by minimising energy with respect to the electron density distribution whilst keeping the potential distribution fixed. The resulting electron density distribution at the energy minimum is the correct ground state distribution.

$$E \leq E[\rho(r)_{trial}] = F[\rho(r)_t] + \int V_{ext}(r)\rho(r)_t dr \quad \text{(Eq. 3.3.5)}$$

In DFT the calculated total energy of a system will always be higher than the true ground state energy, allowing the ground state energy to be approached by

application of the variational principle. It is thus possible to represent the solution of the Schrödinger equation for a system as a functional of the electron density distribution. Practical application of this approach still requires calculation of the electron-electron interactions and kinetic energy. The energy can be broken down as follows:

$$E = T[\rho(r)] + V_{en}[\rho(r)] + V_{ee}[\rho(r)] + E_{xc}[\rho(r)] \quad \text{(Eq. 3.3.6)}$$

In the above equation, the total overall functional is split in to contributions from kinetic energy (T), classical Coulombic electron interactions (V_{ee}, V_{en}) and effects arising from exchange and correlation (E_{xc}). The Coulombic interaction, or Hartree energy, can be expressed as follows:

$$J[\rho(r)] = \tfrac{1}{2} \iint (\rho(r)\rho(r')) / (|r-r'|)\, drdr'$$

Here J is analogous to $V_{en} + V_{ee}$ in Eq. 18. (Eq. 3.3.7)

Workable kinetic and exchange correlation terms are required in order to complete the expression.

A practical approach to producing the required terms was provided by Kohn and Sham in 1965[23]. The electronic system is represented as a system of non-interacting electrons with equal density under the influence of an external potential distribution constructed so as to produce an electron density distribution equivalent to that in a system of interacting electrons. This modified external potential is known as the effective potential V_{eff} and may be used to construct a set of single electron Kohn-Sham (KS) orbitals. KS orbitals may be used to construct a Slater determinant and provide a variational expression for kinetic energy:

$$T[\rho] \leq T[\rho]_{KS} = -\tfrac{1}{2}\Sigma \langle \varphi_i | \nabla^2 | \varphi_i \rangle \quad \text{(Eq. 3.3.8)}$$

The above expression allows an iterative self consistent solution for kinetic energy

and the set of orthogonal KS orbitals. The remaining terms may be solved through application of the Kohn-Sham equation using the Kohn-Sham operator:

$$\hat{H}_{KS} = -\tfrac{1}{2}\nabla^2 + \Sigma\, Z_i/(|r - R_i|) + \int \rho(r')/(|r-r'|)dr' + \delta E_{xc}[\rho(r)]/\delta\rho(r)$$

(Eq. 3.3.9)

The above KS operator contains terms for interactions with the potential field of the nuclei, the Coulombic interactions and the exchange correlation term. At this stage some method of approximating the exchange-correlation term is required to allow self consistent solution of for the density distribution of the system.

3.3.1 The Generalised Gradient Approximation (GGA)

All the unknowns are now in the exchange-correlation term. The exact value for this term is incalculable for non-trivial interacting electron systems, so an approximation is used. The simplest approximation is the Local Density Approximation (LDA) in which the exchange-correlation energy per unit volume for the interacting system is assumed to be the same as that in a uniform interacting system with the same local density, which can be accurately calculated. The LDA is sufficiently accurate for many applications, but in this study the Generalised Gradient Approximation was used with the VASP code. A good discussion of the GGA is provided by Perdew et al[24,25].

In summary, the GGA is based on the LDA but takes in to account rapid variations in electron density by including in its approximation the density gradient. The GGA is expressed as follows:

$$E_{xc}[\rho^{\uparrow}(\underline{r}), \rho^{\downarrow}(\underline{r})] = \int d\rho\ \rho(\underline{r})\varepsilon_{xc}(\rho)F_{xc}(\rho^{\uparrow}, \rho^{\downarrow}, |\nabla\rho^{\uparrow}|, |\nabla\rho^{\downarrow}|)$$

where ε_{xc} = the exchange-correlation energy per electron in a uniform interacting electron gas and F_{xc} = is the exchange correlation 'enhancement factor'.

(Eq. 3.3.10)

Selection of an enhancement factor is discussed by Perdew[25].

3.3.2 Self Consistency

The estimate of E_{xc} provided by the GGA can be used in the following equation for

effective potential (V_{eff}):

$$V_{eff} = v(\underline{r}) + V_H(\underline{r}) + V_{XC}(\underline{r}) \quad \text{(Eq. 3.3.11)}$$

The resulting V_{eff} can be used in the Kohn-Sham equation allowing it to be iteratively solved to self-consistency. In fact, a pair must be solved simultaneously, one for each electron spin state in spin polarised calculations.

An initial 'guess' wave function is randomly constructed, which is used with the KS operator and the KS equations solved to obtain a new wave function. These wave functions are compared and if they match to within a tolerance, the wave function is said to be converged and can then be used to calculate the properties of the system. If not then the process is repeated, substituting the new wave function for the old. In reality simply using the new wave function will rarely result in convergence being reached. What is in fact used is a mix of the old and new functions, with their relative contributions being determined by a mixing parameter. The specific algorithm used in the VASP code is the blocked Davidson method[26], which process is represented schematically below.

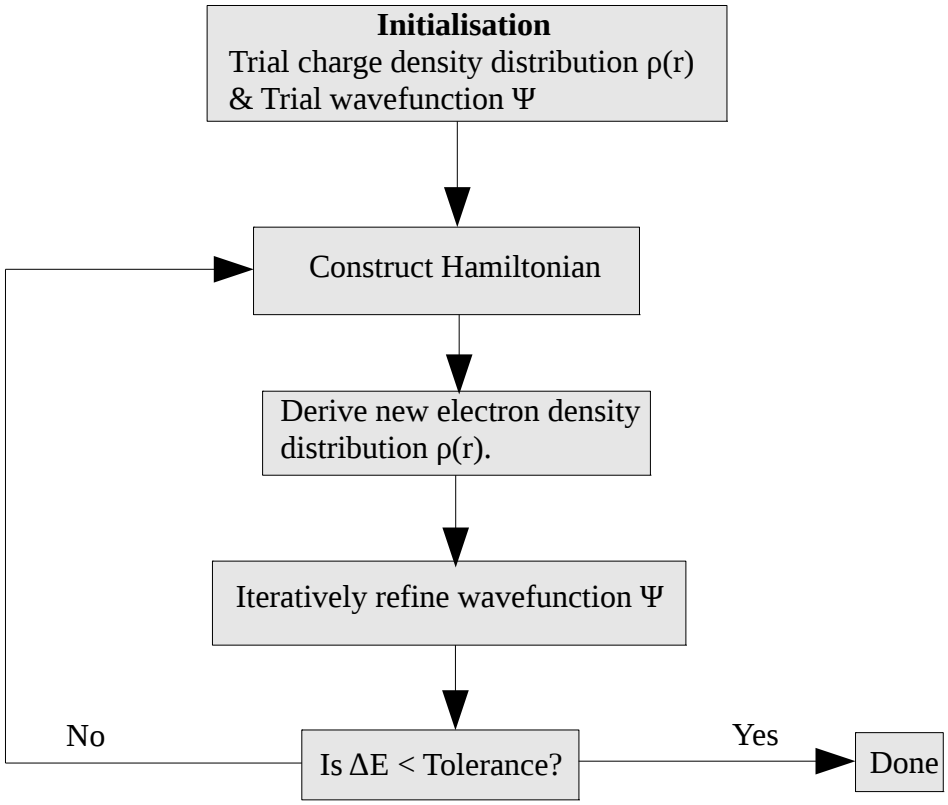

(Fig. 3.3.1)

3.3.3 Basis Set and Pseudo-potential

The Kohn-Sham equation requires a representation of wave functions ($\psi_p(\underline{r})$). A plane wave basis set can be used to represent Kohn-Sham orbitals as follows:

$$\psi_i(\underline{r}) = \Sigma c_{iG}\varphi_G(\underline{r}) = \Omega^{-1/2}\Sigma c_{iG}\, exp(iG.\underline{r})$$

(Eq. 3.3.12)

The sum over the Fourier series must be terminated as some point and since an infinite number of plane waves would be needed for a complete and accurate representation, the point at which it is truncated limits the accuracy. This is normally defined as a specific cut off energy (E_{cut}) related to the basis set by the following condition:

$$E_{cut} > \hbar^2 G^2 / 2m$$

(Eq. 3.3.13)

Ground state energy of the system is convergent with an increasing number of plane waves and hence cut off energy. E_{cut} is a parameter which must be converged for the system studied and largely depends on the choice of pseudopotential.

The use of a pseudopotential allows the core electrons to be treated separately from the valence electrons. Core orbitals are assumed to be equivalent to those in a free atom, so allowing for much reduced computational cost as only the valence orbitals must be calculated explicitly. The function of the pseudopotential is to represent as closely as possible the interaction of the core with the valence electrons. Pseudopotentials are not the true potential generated by the core, but are constructed in such a way as to leave the Kohn-Sham eigenvalues as close to unchanged as possible and produce smooth valence wave functions thereby reducing the required basis set size. A well constructed pesudopotential must result in the lowest energy states being valence states and not in the core.

Pseudopotentials are generally constructed based on results of all electron DFT calculations on free atoms and are constructed to modify only a small spherical region near the core. These potentials should ideally be transferable between systems and so provide a good representation of a particular element core in any given system. The specific pseudopotential functions used in this study are of a class known as Projector Augmented Wave (PAW) pseudopotentials and are those provided with the distribution of the VASP code. Precise details of their nature and construction are provided by those who worked to develop them[27,28]. More generally, the wave functions of valance electrons oscillate rapidly as the core is approached requiring a very large number of plane waves to achieve a good representation at the cost of great computational complexity. PAW pseudo-potentials can achieve substantial reductions in computational cost whilst maintaining accuracy in most situations.

With the theory summarised above, it is possible to achieve a good estimate of the electronic ground state. The lattice structure of the material under investigation

can be arrived at by applying a minimisation process as explained above to the positions of the nuclei. The electronic ground state must be calculated after each adjustment of nuclear positions to give the energy at that point in configuration space. The result is an iterative search for electronic self consistency nested within an iterative energy minimisation search in configuration space. Solving the Kohn-Sham equations is by far the most computationally expensive step and must be performed many times (it sits inside the two nested loops) to produce one minimised structure, requiring large computational resources for each calculation.

3.3.4 Convergent Parameters

Whilst DFT is an ab-initio model and as such requires no empirical or fitted parameters, there are a few adjustable options. Unlike some of the parameters used in the atomistic simulations however, the variables in DFT essentially trade accuracy against computational expense and must simply be converged to within the required degree of accuracy. The adjustable properties of the model are the plane wave cut-off energy (E_{cut}) and the K-point sampling grid size.

The origin of the E_{cut} is discussed in the previous section, and is related to the size of the basis set and thus the accuracy of wave function representation in the Kohn-Sham equations. E_{cut} is a variational property, always resulting in reduced energy calculated as the number of plane waves and hence accuracy increases, making determination of convergence easy. Cut off energies are usually dependent on the pseudopotentials used and are fairly transferable between systems. In the VASP code the cut-off is the same for all entities in the system and so the required value is determined by the most demanding pseudopotential used.

The K-point sampling method used in this work was that devised by Monkhorst and Pack[29]. A regular 3D grid is used to perform Brillouin-zone integration and the density of the grid limits the accuracy of the integration. The density of grid required is a convergent parameter which, unlike E_{cut}, is not variational and is not transferable between systems. The density of grid required is inversely related to the volume of the simulation cell.

3.4 Hybrid Density Functionals

The selfinteraction error inherent in DFT may be corrected for in a number of ways, one of which is to include exact exchange from HF theory in some form[30,31]. In most forms of hybrid DFT some proportion of the exact HF exchange is combined with the approximate DFT exchange-correlation with the aim of significantly reducing the self interaction error and improving the results of the functional. The simplest form of hybrid DFT is a linear combination of HF exchange with DFT exchange-correlation as follows, where '$_X$' denotes exchange contributions and '$_C$' is that of correlation:

$$E_{hyb\text{-}XC} = \alpha E_{HF\text{-}XC} + (1\text{-}\alpha)E_{DFT\text{-}XC} \qquad \text{(Eq. 3.4.1)}$$

In this case α is typically fitted to some experimental parameters, either for a class of materials or individually for a specific model system.

More complex combinations are also possible and yield better results in many situations. Perhaps the best known example is the B3LYP[32] functional which combines several functionals, where '$_{B88}$' is the Beck 1988 functional and '$_{LYP}$' is the functional of Lee, Yang and Parr:

$$E_{XC\text{-}B3LYP} = (1\text{-}\alpha)E_{X\text{-}LDA} + \alpha E_{X\text{-}HF} + \beta E_{X\text{-}B88} + \gamma E_{C\text{-}LYP} + (1\text{-}\gamma)E_{C\text{-}LDA} \qquad \text{(Eq. 3.4.2)}$$

The B3LYP functional is fitted and has been found to work well for many systems including light elements. However, it does not perform well for transition metal oxides or systems including heavy elements. An example which does is the PBE0 functional[33]:

$$E_{XC\text{-}PBE0} = 0.25E_{X\text{-}HF} + 0.75E_{X\text{-}PBE} + E_{C\text{-}PBE} \qquad \text{(Eq. 3.4.3)}$$

PBE0 performs well for a range of systems[34,35], but is unfortunately extremely computationally expensive, especially where a plane wave basis set is used. The computational expense of this functional is due to the slow real space decay of Fock exchange. One way to reduce the computational expense whilst preserving much of the benefit of this functional is to introduce a range separation. One example of such a separated functional is the HSE06 functional[36], SR = Short Range, LR = Long Range:

$$E_{XC\text{-}HSE06} = 0.25E_{X\text{-}Fock,SR} + 0.75E_{X\text{-}PBE,SR} + E_{X\text{-}PBE,LR} + E_{C\text{-}PBE} \quad \text{(Eq. 3.4.4)}$$

The HSE06 functional separates exchange in to short range and long range components. At short range a percentage of exact Fock non-local exchange is added to the PBE exchange. This is separated from the long range PBE only exchange-correlation region by a screening parameter. The screening parameter can be varied to allow for separation at any effective range (pure PBE at zero, PBE0 at infinity) and the fraction of HF energy used in the short range term can be varied between zero (pure PBE) and one (pure HF).

3.5 Periodic Boundaries

The majority of calculations in this project were carried out under three dimensional periodic boundary conditions. Periodic boundaries mean that the environment for the simulated system is provided by tessellating repetitions of its self in three dimensions, extending to infinity. Any change in the simulated area also results in an identical change in the periodic images. This can be thought of either as the simulation cell surrounded by identical images of its self or as the surface of a toroid in n+1 dimensions, where the top joins the bottom and the left edge joins the right. A two dimensional illustration of periodic boundary conditions[37] is reproduced below in figure 3.5.1.

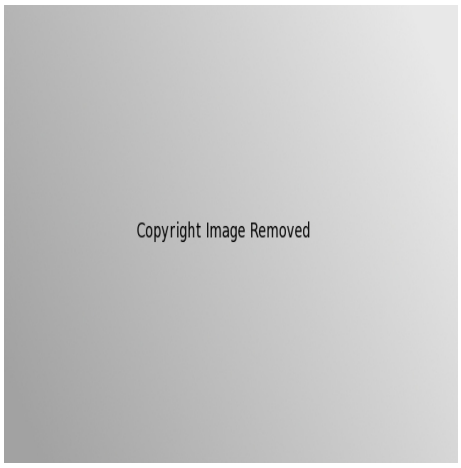

2D representation of periodic boundaries.

(Fig. 3.5.1)

The use of periodic boundaries imposes some restrictions and requirements on the construction of simulations. The simulation cell must contain a complete number of repeating units and be shaped to tessellate perfectly with its repetitions. Any defect or feature contained in the cell will also be repeated in the periodic images. For example, a single defect in a small cell does not represent a single isolated defect in infinite dilution, but actually a finite concentration of identical defects in periodic repetition dependent on cell size. Situations where this must be considered include vacancies and dopant ions, defects and the special case of surfaces.

3.5.1 Vacuum – Slab Model of Surfaces

In order to model surfaces under periodic boundary conditions it is necessary to construct the simulation carefully. The simulation cell is constructed as a section of the material with the bottom layers of atoms fixed in bulk lattice positions making up the 'slab'. The slab must be thick enough that the structure of the surface doesn't change with the addition of extra layers between the fixed 'bulk' layer and the surface. Above this slab a vacuum gap must be left. The result is a simulation of infinitely wide parallel layers of material slab and vacuum. The vacuum gap should be sufficiently wide that any energy or geometry change on widening the vacuum layer is below an acceptable threshold as are any unbalanced forces on the ions in the region of study. The diagram in figure 3.5.2 below illustrates the concept:

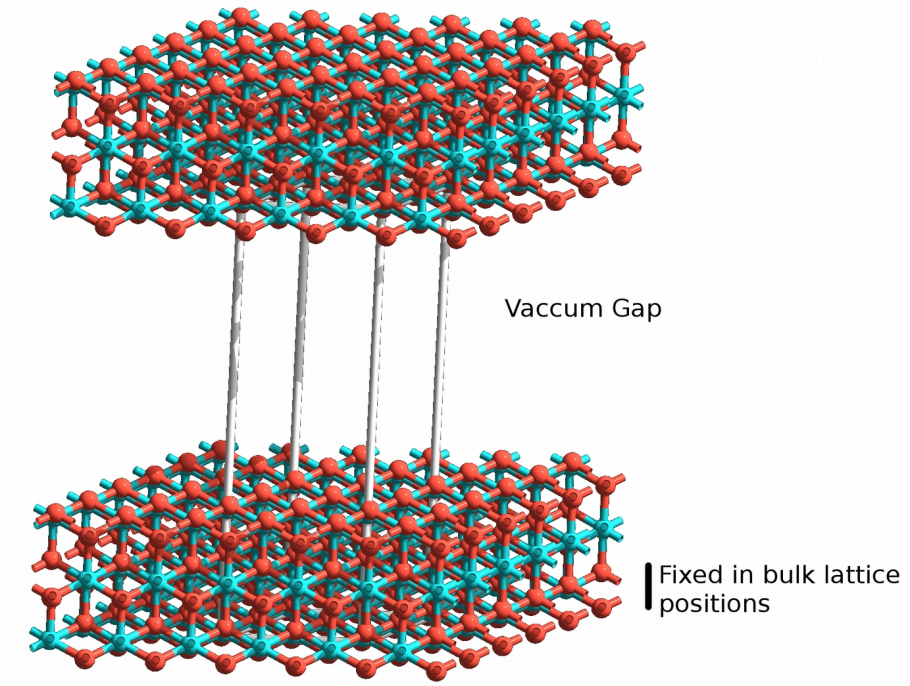

Illustration of the vacuum-slab model. Bounding box represents the simulation cell. (Fig. 3.5.2)

It is also possible to build a vacuum slab model where no ions are fixed, with two surfaces and a bulk like section in the middle of the slab, although a significantly thicker slab is required. In the case of surface interaction with adsorbate molecules the adsorbate is placed in the vacuum gap. Care must be taken to ensure that the molecule has no significant interactions with either the underside of the periodic image of the slab or with adjacent images of its self.

3.6 Optimisation Methods

All possible ways of arranging the species in a given system (the configuration space) and their corresponding potential energy can be imagined as forming a surface or “landscape” with as many dimensions as there are degrees of freedom in the system. The multidimensional surface (hyper-surface) will have various topological features including peaks, troughs and passes between the peaks. Any minima (troughs) deep enough will represent stable or metastable states of the system. Shallow minima can be thought of as reactive intermediates. There is a global minimum in the system representing its thermodynamically most favourable state. The lowest high point (saddle point) which must be crossed represents a

transition state between two minima. Garrison and Srivastava discuss these features in some detail[38]. Computational modelling techniques offer an number of methods of sampling this energy hypersurface. For all but the most trivial systems the hypersurface is larger than could ever be sensibly explored and therefore various sampling methodologies are used; Molecular dynamics allows for time evolution of the system, sampling those points that are reached as part of that natural system evolution. Energy minimisation attempts to find minima by taking samples and following downward slopes by a number of different mechanisms. Monte Carlo simulations sample randomly based upon a set of probability criteria. Pre-programmed sequences of samples can also be taken to explore areas of the energy landscape thought to be of interest, for example likely reaction pathways. Combinations of these techniques are often used.

Energy minimisation searches typically involve the energy calculation of the current position in configuration space then using the derivative of a small move in configuration space or net forces on ions to calculate the search direction. This strategy can be explained with reference to the following Taylor expansion, reproduced from Gale and Rohl[2]:

$$U(x+\delta x) = U(x) + \frac{\partial U}{\partial x}\delta x + \frac{1}{2!}\frac{\partial^2 U}{\partial x^2}(\delta x)^2 + \dots$$

(Eq. 3.6.1)

The series may in practice be truncated at any order. However, it is rare that any term beyond the second is used since it is known in advance that close to a minimum the system becomes harmonic.

The simplest strategy, although inefficient, is to truncate the above expansion and use the first derivatives (g) as discussed below. This process is repeated until it converges. Another more rapidly converging method uses the second order term (H). The method used is known as a Newton – Raphson procedure and can be expressed as follows:

$$\Delta x = -\alpha H^{-1} g$$

Where Δx is the displacement vector and α is a scalar quantity.

(Eq. 3.6.2)

The scalar quantity α is derived from a line search and is needed to prevent the finding of maxima rather than minima. Calculating the inverse Hessian is the most computationally expensive step in the procedure and varies it little between steps. For this reason the Hessian is only calculated (in the GULP implementation) exactly by inverting the second derivative matrix initially and when triggered by one of the following events, quoted from Gale and Rohl[2]:

- The Maximum number of cycles for updating is exceeded.
- The angle between the gradient vector and the search vector exceeds a given threshold.
- The energy has dropped by more than a certain threshold in one cycle, so the curvature is likely to have altered.
- The energy cannot be lowered by line minimisation along the current search vector.

In between the explicit exact calculations the Hessian is updated by an approximate procedure, the Broyden-Fletcher-Goldfarb-Shanno (BFGS) algorithm[39]. The iterative search process is terminated when the energy or other factors have converged, normally to well beyond the accuracy reasonable to expect from other aspects of the model.

Another energy minimisation technique used in this study is the conjugate gradients method. This method is initialised in the same way as a steepest decent approach, but information gained in one iteration is used to influence the next search step as follows:

The steepest descent path is calculated.

$$\Delta x_n = -\nabla_x f(x_n)$$

(Eq. 3.6.3)

The conjugate move is calculated.

$$g_n = \Delta x_n + F_n s_{n-1}$$

(Eq. 3.6.4)

A line search is then performed along the conjugate direction and the position updated. There are several popular functions (F_n) for updating the conjugate directions, the simplest such example is as follows:

$$F_n = (\Delta x_n^\top \Delta x_n) / (\Delta x_{n-1}^\top \Delta x_{n-1})$$

(Eq. 3.6.5)

The conjugate gradients method allows for reasonably efficient selection of search vectors without the need to calculate or invert the Hessian as in quasi-newton approaches.

3.7 Transition State Finding Methods

Accurately locating transition states along reaction pathways is crucial for calculating activation energies, identifying intermediates and assessing which reaction path is likely to be dominant in catalytic systems. Performing a transition state location is a non-trivial problem. The simplest approach is to perform geometry optimisations on initial and final structures, then perform linear interpolation to construct intermediate systems. Reacting components of the system may then be held stationary to prevent the system converging to reactant or product states while the remainder of the system is geometry optimised. A linear interpolation will result in an energy and geometry at each point on a linear reaction path and may be sufficient for some uses. The limitations of a linear stepwise approach are not hard to see, for example the true saddle point is assumed lie on a direct linear path between initial and final configurations and even when it does it is unlikely to be found precisely since only a finite number of intermediate geometries may be calculated. This drawback is apparent when the process is visualised in figure 3.7.1 below:

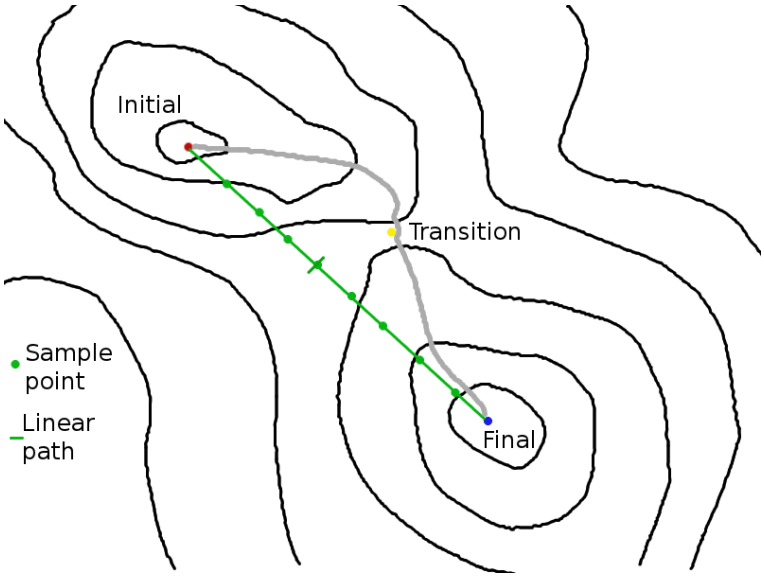

(Fig. 3.7.1)

More sophisticated approaches are necessary for accurate determination of transition states, especially in systems where the reaction path may not be perfectly linear. One such technique is the Nudged Elastic Band (NEB)[40].

NEB is initialised with initial, final and an number of intermediate structures (images) which are normally produced by linear interpolation. The resulting chain of images represents a first approximation of the minimum energy pathway (MEP). These images are then optimised perpendicular to the path between images, with the addition of a 'spring' force linking the images and maintaining even spacing. This effectively forces the images to the bottom of a valley on the energy landscape – a minimum in all directions but the principle reaction path.

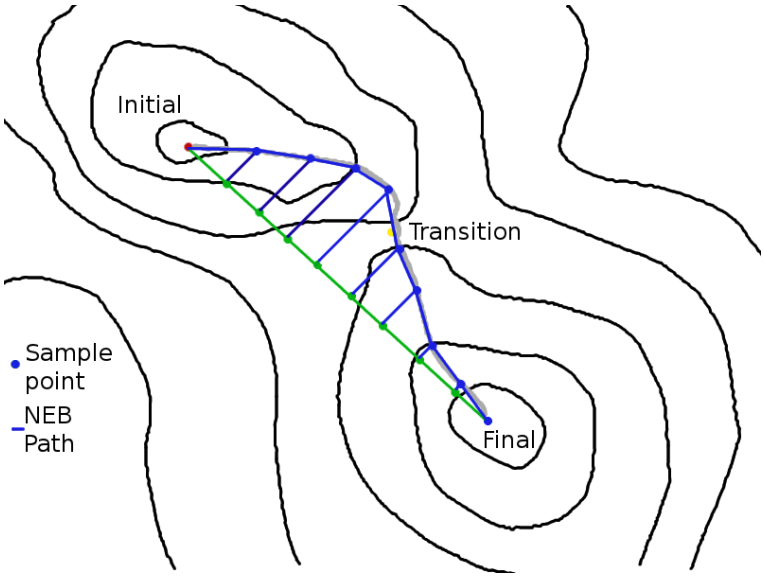

(Fig. 3.7.2)

Finding the transition state is still not guaranteed since there is no necessity for any of the images to optimise to the highest point on the MEP, the saddle point. If used with care the NEB method allows very good determination of transition state geometry, activation energies and the MEP. The principle drawback of NEB methods is that significantly increased computation cost results from the calculation of gradients for many images in the pathway. The cost will depend primarily on the number of images used, a greater number requiring a proportional increase in computational cost but potentially more accurate MEP and transition state determination.

3.8 Charge Analysis

Ionic charges, either partial or formal, are commonly used to describe species within ionic systems. It can be useful to analyse and discuss a system in terms of the charge states of its component species in the bulk, at surfaces or defect sites or as a result of changes due to reactivity. Density functional theory produces a continuous electron density distribution and does not directly provide charges for individual ions in a system. In order to estimate the charge states of individual species the electron density must be divided in some way. There are a variety of methods to partition electrons attributed to each ion. However, the popular Mulliken analysis requires an atomic centred basis set and is not applicable to calculations using a plane wave basis set.

The technique used in this study is known as the Bader “Atoms in Molecules” method[41]. The electron density is divided in to volumes, each representing an ion. The volumes are defined by an electron density maximum surrounded by a boundary surface at the electron density minimum orthogonal to the surface. More formally, a surface is defined by a zero electron density gradient (or zero flux). A volume will typically contain a nucleus and surrounding atomic region, in which case the charge on the species is the difference between the charge of the nucleus and the sum of the electron density within the basin defined by the boundary surface. It is possible in some circumstances for a volume to be defined which contains no nucleus and doesn't represent an atom or ion. The visualisation in figure 3.8.1 shows the Bader volume of a surface ion in a crystalline solid. The bounding surface is shown in yellow, the position of the ions core in grey.

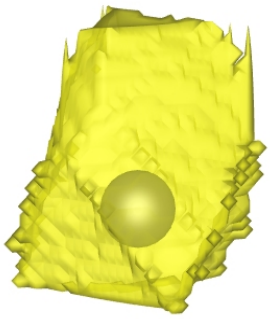

The Bader volume surrounding an ion at the surface of a lattice.
(Fig. 3.8.1)

Bader AIMs analysis allows for a reasonable approximation of the charge state of each species in a system and is independent of the basis set used since it relies only on the calculated electron density distribution.

References

[1] P. Ewald. *Ann. Phys.* 64, 219 **1921**.

[2] J.D. Gale, A. Rohl. *Mol. Sim.* 29, 291 **2003**.

[3] R. Jackson, C.R.A. Catlow. *Mol. Sim.* 1, 207 **1988**.

[4] D. Williams. *Cryst. Rev.* 2, 3 **1989**.

[5] C.R.A. Catlow, E. Kotomin. "Computational Materials Science" ISO Press, **2001**.

[6] J.D. Gale. *JCS Faraday Trans*. 93, 629 **1997**.

[7] J. Perdew, J. Chevary, S. Vosko, K. Jackson, M. Pederson, D. Singh, C. Fiolhais. *Phys. Rev. B.* 46, 6671 **1992**.

[8] J. Perdew, J. Chevary, S. Vosko, K. Jackson, M. Pederson, D. Singh, C. Fiolhais. *Phys. Rev. B.* 48, 4978 **1993**.

[9] B. Dick, A. Overhauser. *Phys. Rev.* 112, 90, **1958**.

[10] S. Kahn, S. Islam, D. Bates. *J. Mat. Chem.* 8. 2299, **1998**.

[11] A. Dwivedi, A. Cormack. *Phil. Mag. A.* 61, 1 **1990**.

[12] C.R.A. Catlow, *Proc. R. Soc. A.* 353, 533 **1977**.

[13] G. Lewis, C.R.A. Catlow. *J. Phys. C.* 18, 1149 **1985**.

[14] V. Fock. Z. *Phys. A: Hadrons.* 62, 795 **1930**.

[15] M. Born, J. R. Oppenheimer, *Ann. d. Physik.* 84, 457, **1927** .

[16] D. Hartree, *Proc. Cambridge. Phil. Soc.* 24, 89, **1928**.

[17] V. Fock, *Z. Phys.* 61, 126, **1930**.

[18] J. Slater, *Phys. Rev*. 35, 210, **1930.**

[19] L.Thomas, *Proc. Cambridge Phil. Soc*. 23, **1927**.

[20] E. Fermi, *Z. Phys*. 48, 73, **1928**.

[21] P. Dirac, *Proc. Cambridge Phil. Soc*. 26, 376, **1930**.

[22] P. Hohenberg, W. Kohn, *Phys. Rev. B.* 136, 864, **1964**.

[23] W. Kohn, L. Sham, *Phys. Rev. A.* 140, 1133, **1965**.

[24] J. Perdew, K. Burke, M. Ernzerhof. *Phys. Rev. Lett.* 77, 3865 **1996**.

[25] J. Perdew, *Int. J. Quant. Chem.* 57, 309, **1996**.

[26] E. Davidson, *Methods in Computational Molecular physics, NATO Advanced Study Institute*. 113, **1983**.

[27] P. Blochl. *Phys. Rev. B.* 5017953, **1994**.

[28] G. Kresse, D. Joubert. *Phys. Rev. B.* 59, 1758, **1999**.

[29] Monkhorst, Pack. *Phys. Rev. B.* 13, 5188, **1976**.

[30] A. Becke, *J. Chem. Phys*. 98, 1372, **1993**.

[31] A. Becke, *J. Chem. Phys*. 98, 5648, **1993**.

[32] P. Stephens, F. Devlin, C. Chabalowski, M. Frisch, *J. Phys. Chem*. 98, 11623, **1994**.

[33] J. Perdew, M. Ernzerhof, K. Burke, *J. Chem. Phys*. 105, 9982, **1996**.

[34] C. Adamo, V. Barone, *J. Chem. Phys*. 110, 6158, **1999**.

[35] J. Paier, M. Marsmann, G. Kress, *J. Chem. Phys*. 127, 024103, **2007**.

[36] S. Heyd, G. Scuseria, M. Ernzerhof, *J. Chem. Phys*. 118, 8207, **2003**.

[37] Periodic Boundary Graphic retrieved from *http://matdl.org/repository/view/matdl:857* 17/2/**2011**.

[38] B. Garrison, D. Srivastava, *Annu. Rev. Phys. Chem.* 46, 373, **1995**.

[39] R. Fletcher, "*Practical Methods of Optimisation*", *Wiley*, **1980**.

[40] G. Henkelman, B. Uberuaga, H. Jonsson, *J. Chem. Phys.* 113, **2000**.

[41] R. Bader, *Acc. Chem. Res*. 18, 9, **1985**.

Chapter 4. YSZ Structure And Properties

This chapter reports results of interatomic potential and density functional theory studies of the bulk and surface structures of pure zirconia and YSZ materials. The thermodynamically preferred defect arrangements in the doped material are explored using a variety of approaches.

4.1 Modelling of Bulk Zirconia

The cubic phase of pure bulk zirconia has been modelled in order to validate the potential model as a precursor to further investigation of doped materials. The material is represented as a 2x2x2 supercell under periodic boundary conditions. The supercell contains 96 ions in total, 32 zirconium and 64 oxygen. Both ion types are represented by the shell model, as discussed in chapter 3. The software used was GULP (General Utility Lattice Program) version 3.4 running on a Linux / x86-64 computer. The parameters used are provided in Tab. 3.1.2.

The initial structure is relaxed to a minimum using a quasi-newton BGFS energy minimisation (see chapter 3 for more detail) under conditions of constant pressure. The relaxed structure is visualised below, red representing oxygen and blue representing zirconium. When viewing this and future visualisations it is important to remember that the cell edges represent periodic boundaries, thus pairs of ions may be closer across a boundary than through the volume of the cell as visualised in figure 4.1.1.

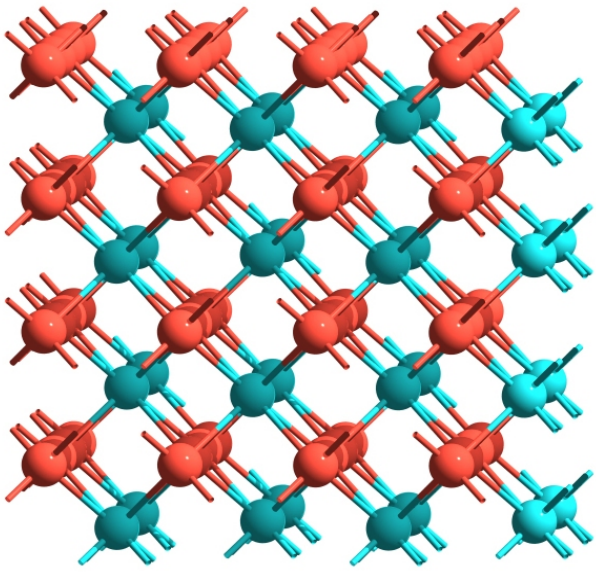

Local energy minimisation of the 2x2x2 super-cell of pure cubic zirconia by interatomic potentials. Oxygen is red, zirconium blue.

(Fig. 4.1.1)

As can be seen from the above visualisations, the structure maintains its highly symmetric, perfectly cubic lattice. The cells angles α, β and γ are all 90° and the lengths of super-cell sides a, b and c are all equal at 10.151Å (See table 4.1.2.). Since this material has unbroken cubic symmetry the model is trapped in the local energy minimum and can not relax to the more thermodynamically favoured monoclinic structure.

The calculated structural and energetic parameters may be compared with both experimentally derived parameters and those calculated by other methods. One such method is DFT (density functional theory). DFT calculations were carried out using VASP (Vienna ab initio simulation package) version 4.6 incorporating the projector augmented wave pseudo-potentials and the PW91 GGA functional (see chapter 3 for more detail). In order to perform valid DFT calculations on the material it was necessary to select appropriate plane wave cutoff and k-point mesh parameters. Both of these parameters were selected by performing calculations with increasing values until the calculated energy is judged to have converged. The energetic convergence of these parameters can be seen in the graphs below as a function of plane wave cut-off energy and k-point mesh respectively.

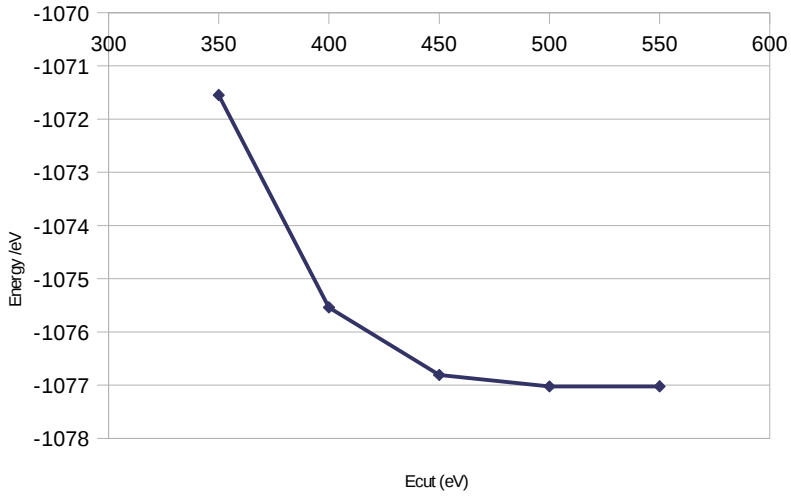

DFT energy as a function of increasing cut-off energy.

(Fig. 4.1.2.)

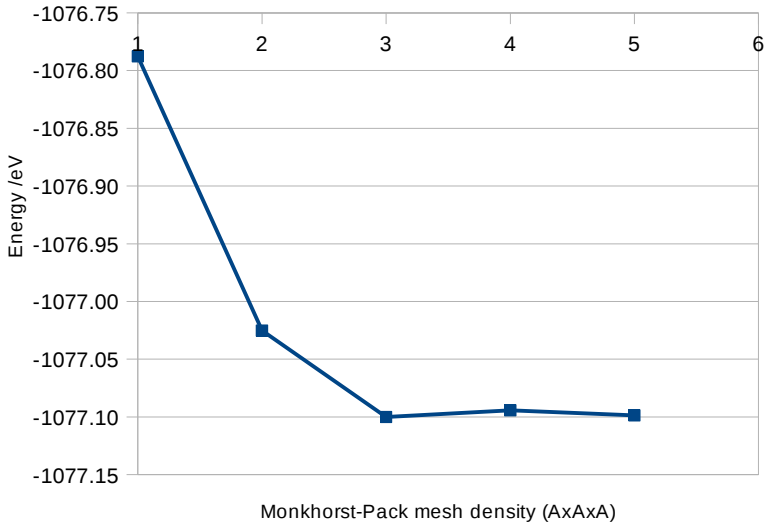

DFT energy as a function of k-point mesh density.

(Fig. 4.1.3.)

On the basis of these calculations a cut-off energy of 500eV and a 4x4x4 k-point mesh were chosen and applied for all subsequent DFT calculations on the bulk supercell.

The perfect cubic structure and symmetry are present in the local minimum found based on DFT calculations. The angles α, β and γ are all 90º. The sides a, b and c of the supercell are all 10.245Å in length, slightly longer than those predicted by interatomic potentials methods. Electronic structure calculations using the HSE06 hybrid exchange functional within the VASP software were also carried out on bulk pure zirconia in preparation for later work and yielded 2x2x2 supercell edge lengths of 10.203Å (see Tab. 4.1.2. below).

Property	I.A. Potentials	DFT	HSE06	Experimental[1-3]
Zr - Zr (Å)	3.59	3.62	3.61	3.59
O - O (Å)	2.54	2.56	2.55	2.56
Zr – O (Å)	2.19	2.22	2.21	2.20
Cell Lengths (Å)	5.08	5.12	5.10	5.07
Cell Angles	90.00	90.00	90.00	90.00

Structural properties of pure bulk cubic zirconia as predicted by differing computational models, compared to experimental observations.

(Tab. 4.1.2)

From the results presented in table 4.1.2 it is apparent that all three computational methods perform well in reproducing the bulk structure of pure cubic zirconia, although all result in a very slightly larger cell than that seen experimentally. The two electronic structure methods (DFT, HSE06) result in calculated structural properties differing in the same direction from the experimental observations.

The electronic structure methods also provide an electron density distribution which can be used assess the charges on ions within the system. Bader charge analysis was applied to partition and integrate the electron distributions (see section 3.8.) and the results are tabulated below (tab. 4.1.3).

Species	DFT Charge	HSE06 Charge	Formal Charge
O	-1.73	-1.79	-2.00
Zr	+3.46	+3.58	+4.00

Bader charges as predicted by DFT and HSE06 electronic structure methods. (Tab. 4.1.3)

Both electronic structure methods produce partial charges less than the formal charges of the ions, although the material is strongly ionic. It is known that the Zr – O bonding has some covalent character (see Chapter 2.) and also that pure plane-wave GGA-DFT has a tendency to excessively de-localise electrons. The HSE06 hybrid method contains a proportion of HF exchange and will favour slightly greater electron localisation relative to GGA-DFT. See chapter 3 for more detail of the methods. These differences explain the slightly greater, and possibly more realistic, ionicity found by the HSE06 method over GGA-DFT, although we note that the system is still strongly ionic.

4.2 Bulk YSZ Modelling

Defects resulting from doping, namely yttrium on zirconium sites and oxygen vacancies, may be configured in several sites within the structure. This section presents results of calculations of the relative thermodynamic stabilities of possible configurations.

A number of possible approaches to analysing bulk defects are used. Within the periodic supercell model both manually selected configurations and automated exhaustive configuration space exploration are used. With all the interatomic potentials modelling work, further parameters are required for the interactions of the yttrium ions. The parameters used are tabulated below (tab. 4.2.1).

Charges

Entity	Charge
Y atom	3.000

Buckingham

Entity	A (eV)	ρ (Å)	C (ev Å^{-6})	Cut-off (Å)
Y atom – O shell	1345.100	0.3491	0.00	10

Partial charge and Buckingham potential parameters add a representation of yttrium to the model of zirconia previously described.

(Tab. 4.2.1.)

It will be noted that the yttrium ion is treated as a rigid ion as discussed in section 3.1. Initially nearest neighbour (NN) and next nearest neighbour (NNN) configurations were selected and analysed as a single defect cluster within a 2x2x2 periodic supercell. The periodic super cell model was also subjected to GGA-DFT modelling. Bader charge analysis was applied to derive estimated charges for each ion in and around the defect cluster as calculated by GGA-DFT, these are displayed below for a 2x2x2 supercell containing a NN configured system.

Element	Charge (ZrO_2)	Min. Rel. Charge	Max. Rel. Charge	Mean Rel. Charge	Range
Zr	+3.46	-0.04	+0.03	+0.01	0.07
O	-1.73	-0.08	+0.13	+0.01	0.21
Y	-	-	-	+2.16	-

Partial Bader charges for ions in a GGA-DFT cell containing a defect.

(Fig. 4.2.1.)

As discussed earlier, Bader charge analysis yields somewhat different charge values than those used in the interatomic potentials modelling. Moreover, ions in the defect region can be seen to have slight variations from those in pure zirconia bulk material. The introduction of an oxygen vacancy and substitution of two zirconium ions by yttrium results in both the alternating layers of slightly increased and reduced electron density, the affect weakening with distance from the defect and a stronger effect observed on the oxygen ions than zirconium. On average, both the oxygen and zirconium become very slightly more positive in the doped material than pure zirconia. Yttrium has a net charge of only +2.156, as opposed to the 3+ formal charge it is typically assigned in models and discussions of its properties. The energy difference as calculated by each method for most stable nearest neighbour and next nearest neighbour configurations are given in the table below.

Method	NNN - NN lattice energy (eV)
interatomic Potentials	-1.07
DFT	-0.82

Energy difference between most stable NNN and NN configurations of a single defect in a 2x2x2 periodic supercell.

(Tab. 4.2.2.)

As can be seen both methods favour the NNN configuration by a difference of very approximatly electron volt. The interatomic potentials method yields a greater difference than DFT. This preference for NNN over NN configurations is in agreement with experimental work[4,5] and a number of previous researchers' calculations[6-10], although there is not agreement as to the precise energy differences found. It should be noted that this energy difference is for the material with an extremely low dopant concentration (a single defect cluster in the 2x2x2 supercell). The differences between arrangements become significantly smaller at higher concentrations, as discussed later.

Another approach taken to explore the energetics of low concentrations of defects was to explore systematically all possible inequivalent arrangements of a single oxygen vacancy and two yttrium ions within the 2x2x2 periodic supercell. All

symmetrically inequivalent configurations were generated with the use of the SOD (Site Occupancy Disorder) program[11] and underwent energy minimisation using the GULP software with the potential model described previously. There were a total of 33 inequivalent configurations. Given below is a visualisation of the most stable arrangements found. Both yttrium ions are in NNN relationships to the oxygen vacancy. This relationship is harder to see and less well defined in the relaxed structure since ions move to compensate for the vacancy.

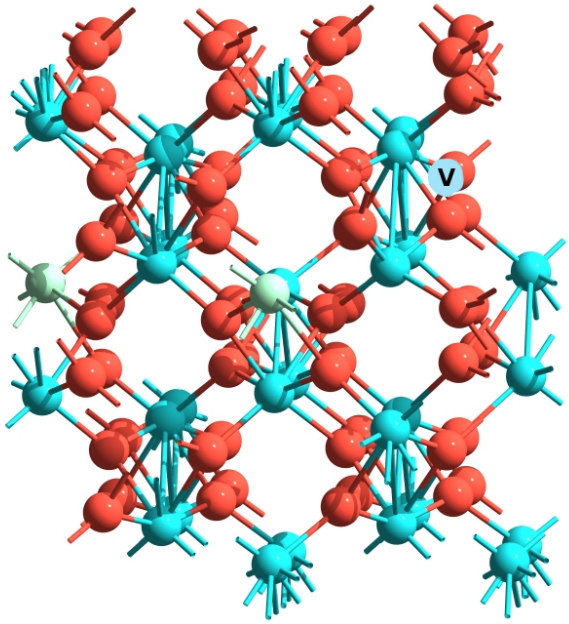

The most stable configuration of a single defect cluster in a 2x2x2 supercell as predicted by interatomic potentials modelling. Oxygen is red, zirconium blue, yttrium green. The oxygen vacancy is in the area of the pale blue circle labelled 'V'. (Fig. 4.2.2)

At this yttrium concentration, the ionic arrangement is significantly and regularly distorted. The overall cell maintains an approximately cubic structure, but with a significant increase in volume. This is consistent with materials at this doping level being only 'partially stabilised' in the cubic phase. The parameters of the relaxed supercell are tabulated below (tab. 4.2.3), along side the pure ZrO_2 supercell for comparison.

	a (Å)	b (Å)	c (Å)	α	β	ɣ	Vol (Å^3)
ZrO_2	10.152	10.152	10.152	90.000	90.000	90.000	1046
YSZ	10.501	9.887	11.112	90.182	89.752	90.441	1154
Δ	0.349	-0.265	0.960	0.182	-0.248	0.441	107.3
%Δ	3.44	-2.614	9.461	0.203	-0.276	0.491	10.25

Structural parameters for a 2x2x2 supercell in the most stable configuration of a single defect cluster (Fig. 4.2.2) and the pure material. Δ represents the change between ZrO_2 and YSZ.

(Tab. 4.2.3.)

An analysis of lattice energies for all configurations gives a range of 4.13eV. The distribution of energies can more easily be seen when expressed graphically as below.

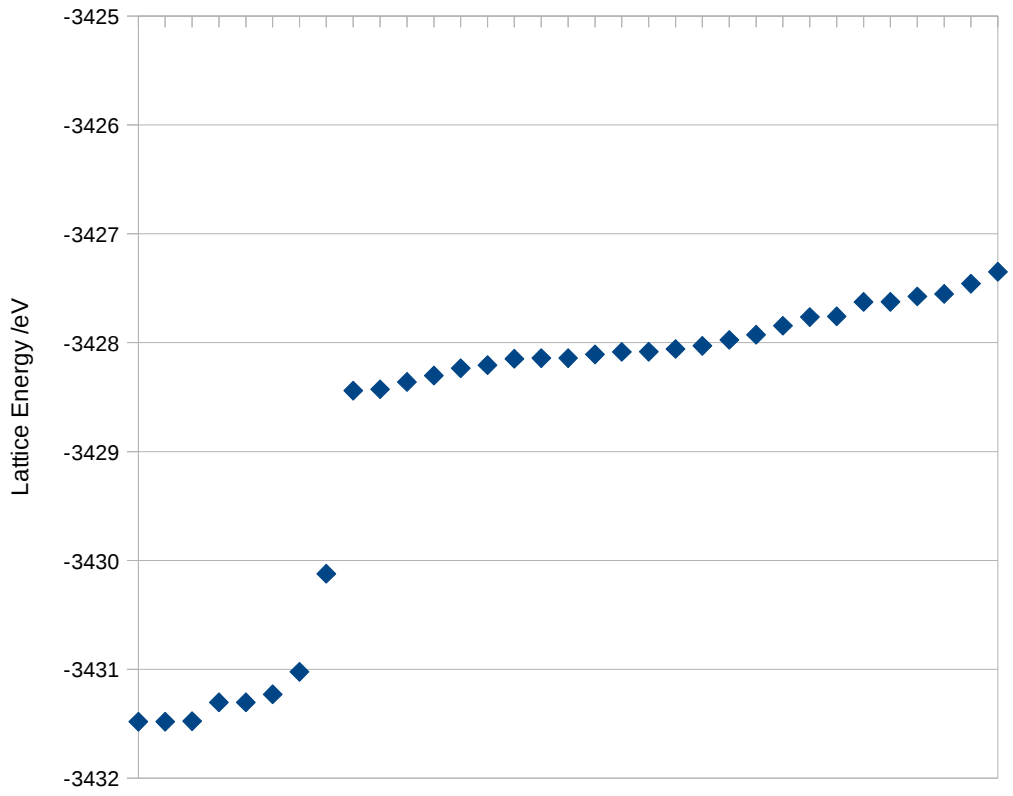

Interatomic potentials model lattice energies (y-axis) of all possible configurations (x-axis) of a single defect cluster within a 2x2x2 supercell.

(Fig. 4.2.3.)

The distribution can be separated in to two groups, each of which contains members of similar lattice energy with the range evenly covered. The more stable

configurations (lattice energy < -3431eV) are NNN and mixed NN/NNN relationships. The configurations in the less stable (lattice energy > -3429eV) group contains the NN arrangement and those with only one or no NN or NNN relationships. The single configuration in neither group (lattice energy -3430eV) contains neither NN or NNN relationships between the vacancy and yttrium ions, however the yttrium ions are in a NN relationship to each other.

In addition to the above calculations which focussed on the preferred configuration of isolated defects in low concentrations, further calculations were carried out to explore higher dopant concentrations. These calculations were all carried out in the 2x2x2 supercell and initial configurations were manually selected. An exhaustive study was not feasible at the higher dopant concentrations owing to the rapid growth in the size of configuration space with number of defects present and computational time.

One defect within the 2x2x2 supercell is equivalent to 6.25mol % $YO_{1.5}$ while three is 18.75% and four 25%. 3 and 4 defects in the 2x2x2 supercell represent dopant concentrations which would be present in fully stabilised YSZ materials. It is worth noting that an exhaustive search of configuration space was performed at 6.25 mole % but at the other concentrations the sampling represents a small proportion of the full configuration space. Results for the most stable configuration found at each concentration are tabulated below (tab. 4.2.4).

Defects in 2x2x2 supercell	Mole % $YO_{1.5}$	Lattice Energy (eV)	Cell Volume ($Å^3$)
0	0.00	-3512	1046
1	6.25	-3431	1154
3	18.75	-3262	1081
4	25.00	-3180	1090

Interatomic potentials lattice energy and cell volume of YSZ materials with differing doping levels.

(Tab. 4.2.4)

The most stable configurations found at 18.75 and 25 mole % $YO_{1.5}$ are visualised below in figure 4.2.4.

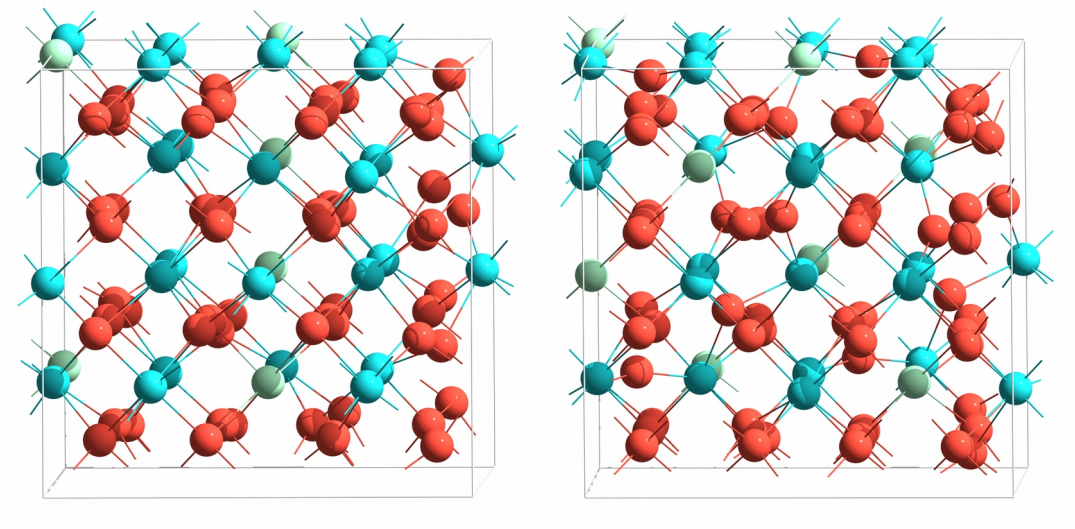

18.5 Mol % $YO_{1.5}$ 25 Mol % $YO_{1.5}$

Visualisations of the most stable YSZ structures found at higher doping levels using the potential model. Red represents oxygen, blue zirconium and green yttrium. (Fig. 4.2.4..)

It is readily apparent that the cation lattice remains relatively close to a perfect cubic arrangement. The cation lattice is much close to perfect cubic geometry than in the partially stabilised 6.25% material shown in Fig. 4.2.2. The oxygen anion lattice undergoes more significant disordering, increasing as the dopant concentration rises. The increased disordering of the oxygen lattice leads to relatively minor energy differences between oxygen arrangements. Low energy differences between arrangements is a necessary factor in the materials oxygen anion conduction capabilities. Further exploration of ionic conduction can be found in Chapter 5.)

Bulk YSZ Conclusions

The study of highly dilute yttrium dopant and oxygen vacancy defect clusters performed using interatomic potentials and DFT techniques suggests that, at least in isolation, the NNN relationship is thermodynamically favoured. Many defect arrangements are possible within an energy range of 1eV within two groups of configurations with a rather larger gap (~2.5ev) separating the groups. The dopant concentration modelled here (6.25 mole % yttria) is significantly lower than that used in the majority of commercial materials. The material deviates from perfect cubic structure with significant disordering of the ionic lattice and undergoes significant lattice expansion.

At higher doping concentrations (18.5 and 25 mole % yttria) the cubic structure stabilises. The cation lattice adopts a nearly perfect cubic arrangement, while the oxygen lattice disorders increasingly with dopant concentration. The disordered oxygen lattice in these structures results in a small energy difference between possible oxygen ion arrangements with respect to the yttrium dopant making the NN / NNN relationships difficult to define within the more complex structure and with no clear conclusion as to relative stability. When it is also considered that, in the majority of applications, these materials will be at relatively high temperatures the energy differences between arrangements may be considered unimportant to the materials overall properties and behaviour. The near equivalence of ionic arrangements is one prerequisite for the oxygen conduction behaviour discussed later in Chapter 5.

References

[1] C.R.A. Catlow, *J. Chem. Soc. Faraday Trans,* 86, 1167, **1990**.

[2] A. Dwivedi, A. Cormack, *Philos. Mag. A.* 61, 1, **1990**.

[3] M. Ruhle, H. Heuher, *Adv. Ceram.* 12, 14, **1984**.

[4] A. Bogicevic, C. Wolverton, G. Crosbie, E. Stechel, *Phys. Rev. B.* 64, **2001**.

[5] T. Welberry, R. Withers, J. Thompson, B. Butler, *J. Solid State Chem*. 100, 71, **1992**.

[6] P. Li, I. Chen, J. Penner-Hahn, *J. Am. Ceram. Soc*. 77, 118, **1994**.

[7] C.R.A. Catlow, A. Chadwick, G. Greaves, L. Moroney, *J. Am. Ceram. Soc*. 69, 272, **1986**.

[8] A. Gallardo-Lopez, J. Martinez-Fernandez, A. Dominguez-Rodriguez., *Philos. Mag. A.* 81, 1675, **2001**.

[9] A. Gallardo-Lopez, J. Martinez-Fernandez, A. Dominguez- Rodriguez, *J. Euro. Ceram. Soc*. 22, 2821, **2002**.

[10] X. Xia, R. Oldman, C.R.A. Catlow, *Chem. Mater.* 21, 3576, **2009**.

[11] R. Grau-Crespo, S. Hamad, C.R.A. Catlow, N.H. de Leeuw, *J. Phys.: Condens. Matter,* 19, 256201, **2007**.

Chapter 5. Ionic Conduction

The ability of YSZ materials to conduct oxygen anions rapidly at high temperatures is crucial to many of their important industrial applications, including SOFCs, oxygen purification and sensing and probably also in catalysis. The bulk conduction behaviour of these materials has been well studied and is discussed in chapter 2. This chapter reports results of calculations analysing the conduction behaviour both in the bulk and near surfaces.

5.1 Bulk Migration and Defects

The structure of zirconia can be visualised as a primitive cube, with oxygen anions at the vertices and a zirconium cation at half the centres. Oxygen migration occurs through an oxygen ion moving from one vertex of the cube to an adjacent vacant vertex site. There is an energy barrier to this process, reaching a maximum as the oxygen ion passes between two adjacent zirconium ions. The migration process is discussed in more detail in chapter 2.

5.1.2 Methodology

The bulk material is modelled as a 2x2x2 supercell within periodic boundary conditions, as in section 4.2. Initial and final structures are constructed starting with the pure zirconia structure by substituting an identical pair of zirconium ions with yttrium and creating an oxygen vacancy at one of two adjacent locations. The initial and final structures are energy minimised to give the end points for the migration of the oxygen ion. An approximate migration pathway is constructed through linear interpolation of a number of points between the relaxed initial and final structures. The interpolated intermediate configurations, 'images', are used as the input for a Nudged Elastic Band (NEB – see chapter 3) calculation which approximates the minimum energy pathway, transition state geometry and activation energy.

The calculations as described above are carried out using either a DFT model using the VASP software package, or GULP with the interatomic potential model described in chapter 3.

5.1.3 Results

Initially a single defect cluster is placed within the 2x2x2 supercell, representing a very low concentration of yttrium (below the threshold for full thermodynamic stabilisation of the cubic phase). In this case NN and NNN models are constructed. In both cases the models are symmetrical with respect to the migration so that the initial and final positions should be at equivalent distances from the yttrium ions.

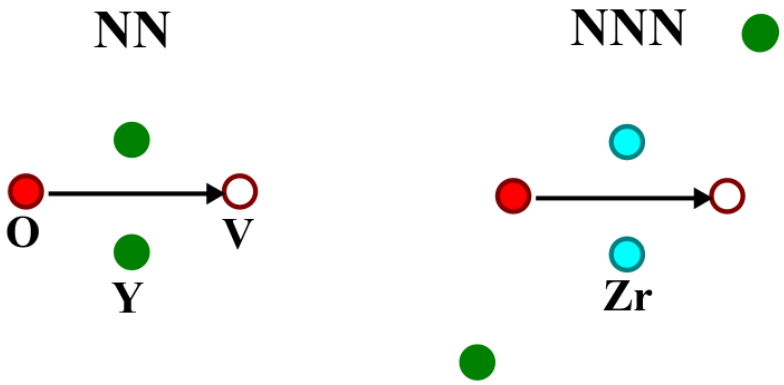

Graphical representation of NN and NNN oxygen ion migration paths.
(Fig. 5.1.3.1.)

NN and NNN interatomic potentials NEB energy profiles, derived using interatomic potential models, of migration pathways within a 2x2x2 bulk supercell with a single V-Y-Y defect cluster are given below (Fig. 5.1.3.2).

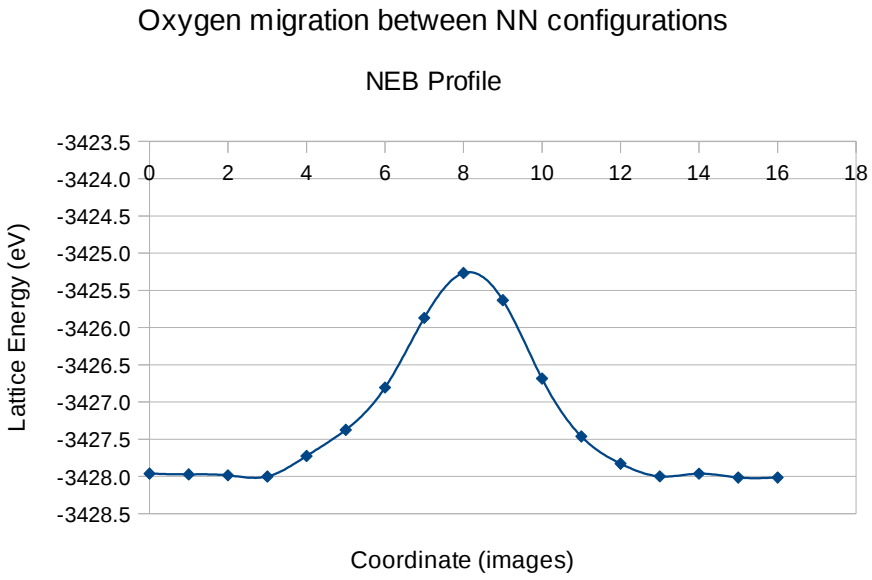

Interatomic potentials NEB energy profile for oxygen migration between NN Y-V-Y configurations.
(Fig. 5.1.3.2.)

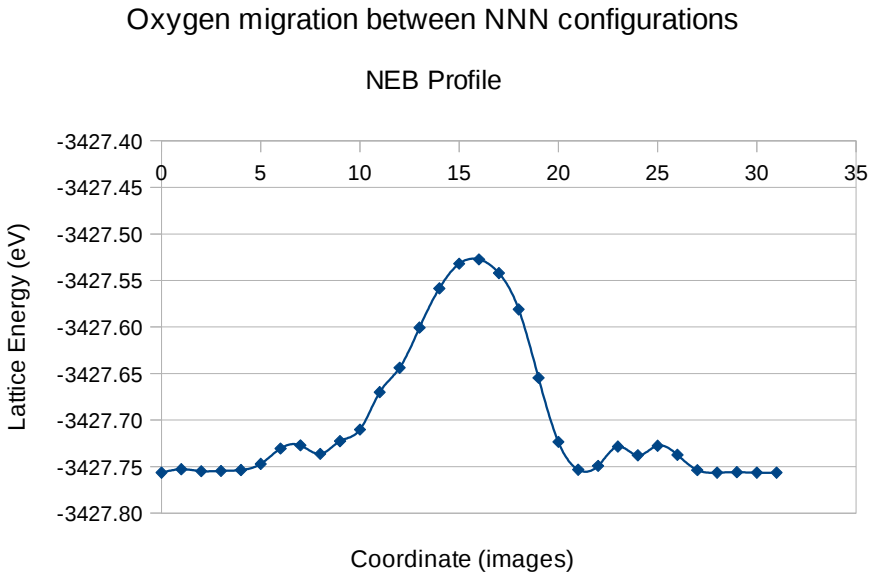

Interatomic potentials NEB energy profile for oxygen migration between NNN Y-V-Y configurations.

(Fig. 5.1.3.3.)

As can be seen, the above NEB profiles are approximately symmetrical about a well defined transition state and activation barrier (the central peak). It will also be apparent from the differing energy scales (Y-axis) that the NN migration pathway has a greatly higher (2.74eV) activation barrier than observed with the NNN configuration (0.23eV) predicted by the interatomic potentials model.

Migrations within fully stabilised cubic YSZ systems were also modelled using interatomic potentials. The initial image for these simulations is the lowest energy 18.75 mole % $YO_{1.5}$ 2x2x2 supercell found in the work described in Chapter 4. Five final positions were then chosen where one oxygen ion is swapped with a neighbouring vacancy and this structure is relaxed under constant pressure conditions. A NEB calculation based on a linear interpolation between the relaxed initial and final configurations is then performed. A number of differences from the highly symmetrical, low yttrium concentration models were observed.

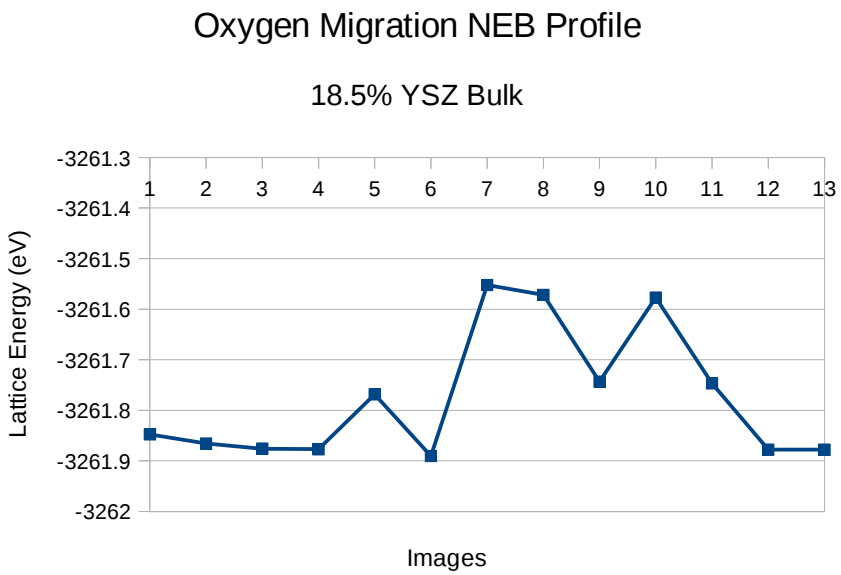

Interatomic potentials NEB energy profile for oxygen migration within 18.75 mole % $YO_{1.5}$ bulk YSZ.

(Fig. 5.1.3.4.)

As can be seen in the above NEB energy profile (fig. 5.1.3.4), migrations within the more complex highly doped structures are less symmetrical and do not always have a single well defined transition state. The profile above possesses two or three distinct peaks, two higher (~0.35eV) and one lower peak (~0.1eV). The five activation energies observed from differing migrations ranged from 0.32eV to 0.79eV.

5.1.4 Discussion

The results presented in this section show that the bulk migration activation energies can cover a wide range of values (~0.2 to 2.8eV). The energy for any given path depends upon the distortions in the lattice and most importantly the proximity of other defects including yttrium ions. The results show that pathways which pass between two adjacent yttrium ions incur a significant increase in activation energy relative to those which pass between zirconium ions with more distant yttrium ions. This finding is consistent with other reported findings[1-5] which suggest that higher concentrations of yttrium can slow the migration of oxygen ions through the material.

It has also been suggested that stable clusters of multiple vacancies and dopant ions can form and trap migration vacancies. The work reported in this section

does not address this issue, although the same technique could be applied to examine the effects of clustering by calculating activation energies for migration paths in clustered defect structures.

The calculations carried out using the 18.75% $YO_{1.5}$ YSZ material show a narrower range of activation energies than found in the lower concentration material. However it should be noted that the structures used did not include any highly clustered defects which may be present in materials at this concentration. It would appear that the more highly stabilised cubic structure, with increased oxygen lattice disordering found at higher Y concentrations acts to remove both the very high and the lowest migration paths found in the low concentration material.

Bulk calculations reported above give some insight as to the effect of dopant proximity, based on tightly controlled structures and migration paths. The range of activation energies found, with the exception of the very high energy of the NN migration path, is consistent with range of values reported in various experimental and modelling studies[1-6]. Comparable energy ranges are found to molecular dynamics studies simulating the time evolution of the systems at finite temperatures employing the methodology described above which uses only static minimisations. The methodology applied here is next adapted to study the effect of surface proximity on oxygen migration.

5.2 Near Surface Conduction

Surface effects on oxygen anion mobility are likely to have implications in areas of catalysis, SOFCs and junctions between YSZ and other metal oxide systems. Although there is extensive discussion of oxygen migration in the bulk[1-6], there is no detailed investigation of the effect of surface proximity on oxygen anion mobility. This section aims to apply interatomic potential modelling, as well as some examples using a DFT approach, to provide insight in to the question of possible surface effects on ionic mobility.

5.2.1 Preliminary Exploration

A preliminary exploration of possible near surface effects was conducted. An oxygen terminated (111) vacuum slab model was constructed, similar to that

described in section 5.2.2, with a slab approximately 24Å thick and 7.5Å wide. Single defect clusters Y-V-Y were introduced in random positions. Migration paths were approximated by linear interpolations between end points, with the migrating ion constrained at equally spaced intervals along the migration path. This method is limited as it assumes perfect linearity of migration paths which does not hold in all cases and can cause spuriously high activation energies to be observed. The results of this work suggested a general trend for lower activation energies near to the surface and are represented graphically below (Fig. 5.1.1).

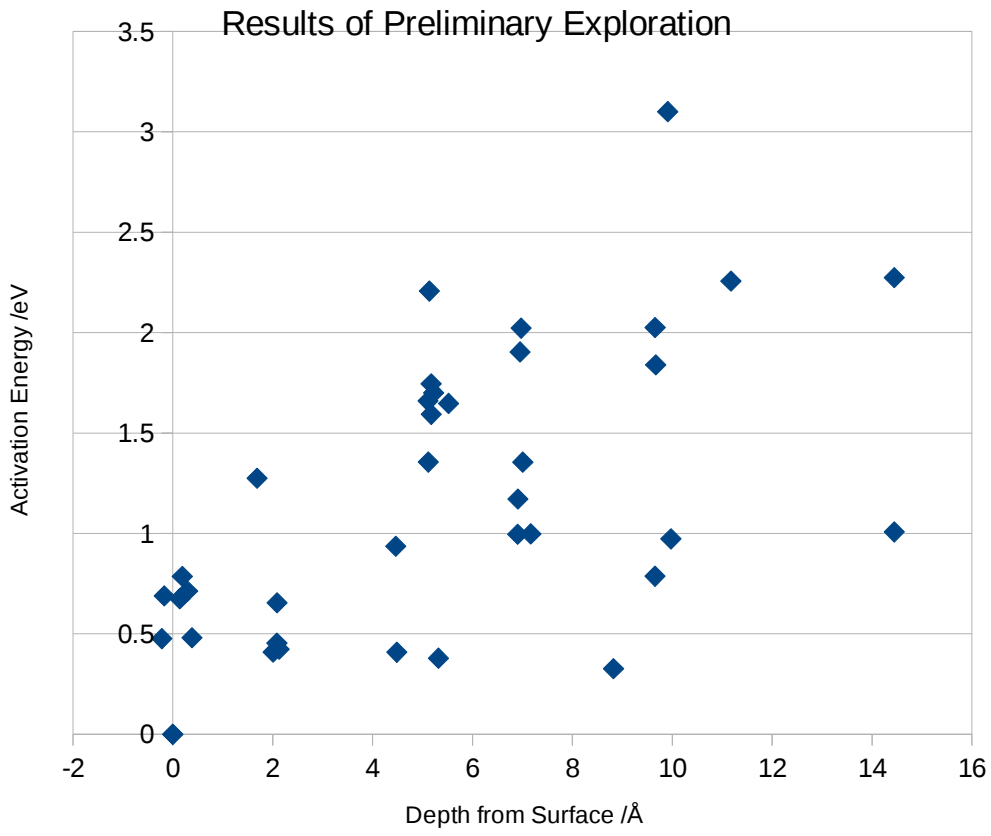

Activation energy as a function of depth, derived from interatomic potentials moddeling. Surface depth was defined as the mean Z distance of the initial and final positions from the surface layer of oxygen ions.

(Fig. 5.1.1)

It will be noted that the range of activation energies seen in Fig. 5.1.1 are far wider and include much higher activation energies that those seen in studies of bulk migration in this material. There are also paths where calculations failed to converge. This is attributable to the limitations of constraining the migrating ion to a perfect linear path. A more sophisticated approach to approximating the migration path and transition state is needed to confirm the trend hinted at by these results.

5.2.2 Refined Methodology

Several studies[7-10] have suggested that the most stable and predominant surface of YSZ is the (111) terrace. There is also evidence to support the presence of step features at intervals on the surfaces of cubic YSZ materials. The work presented in this section is based upon a vacuum-slab model of the oxygen terminated (111) terrace surface of YSZ.

Calculations are performed employing GULP version 3.4 (interatomic potentials) or VASP version 5.3 (DFT). The surfaces of the material are described as a vacuum-slab approximately 24Å thick, 7.5Å wide and with a vacuum gap of 15Å. Confidence that the slab is sufficiently thick can be gained from the negligible net forces acting on the atoms in the lower layers following energy minimisation. This vacuum-slab unit is repeated under 3D periodic boundary conditions. The lowest layer of cations and two lowest layers of anions have had their core coordinates locked in bulk like lattice positions. The coordinates of the shells are also fixed in the lowest but not the second lowest layer of anions in interatomic potential models.

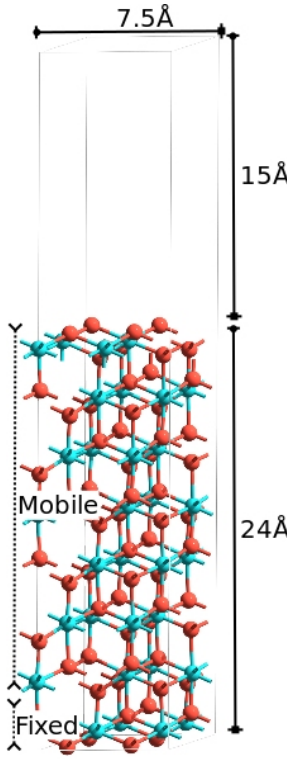

The slab model of YSZ surface.

(Fig. 5.2.1.1.)

The slab is then doped as required and the geometry optimised under conditions of constant pressure using interatomic potentials in the GULP software package. Dopant positions are chosen in or as near as possible to equivalent positions in each of the mobile layers of the material. Initial and final configurations are chosen at a series of depths from the surface, with equivalent relative yttrium positions and the oxygen vacancy swapped with a neighbouring oxygen. Linear interpolation between relaxed initial and final structures is used to generate a set of images (generally 11) which form the input to a NEB transition state search.

5.2.3 Results

The interatomic potentials model and NEB technique were applied to construct an energy profile for a migration between neighbouring oxygen positions at a range of depths from the surface. Below is a typical energy profile (Fig. 5.2.2.1).

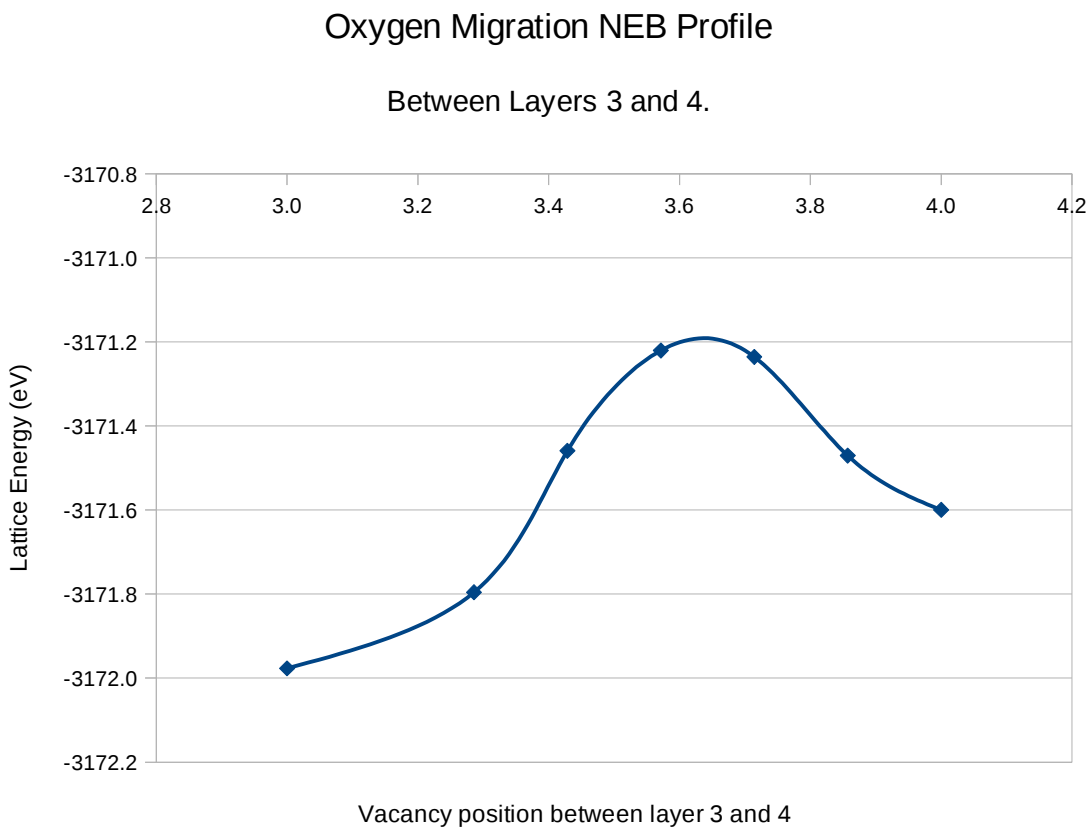

Typical inter-atomic potentials NEB energy profile for oxygen migration near the 111 surface of YSZ. The x-axis units represent evenly spaced images between layers. (Fig. 5.2.2.1.)

As can be seen from the above graph the initial and final positions are not of equivalent energy and thus the forward and reverse activation energies differ somewhat. There is a single well defined activation barrier between the initial and final configurations.

The energies for migrations at different depths with consistent relative yttrium placement are tabulated below. Depth relates to the vacancy and is counted in layers of oxygen from the surface (layer 0).

Oxygen Layers	Forward (eV)	Reverse (eV)
0 to 1	-	-
1 to 2	0.27	0.32
2 to 3	0.33	0.42
3 to 4	0.66	0.38
4 to 5	0.33	0.65
5 to 6	0.54	0.68

Activation energy of oxygen migration between different layers in YSZ. Layers 0 and 1 optimise to the same structure.

(Tab. 5.2.2.1)

The results are plotted graphically below (fig. 5.2.2.2).

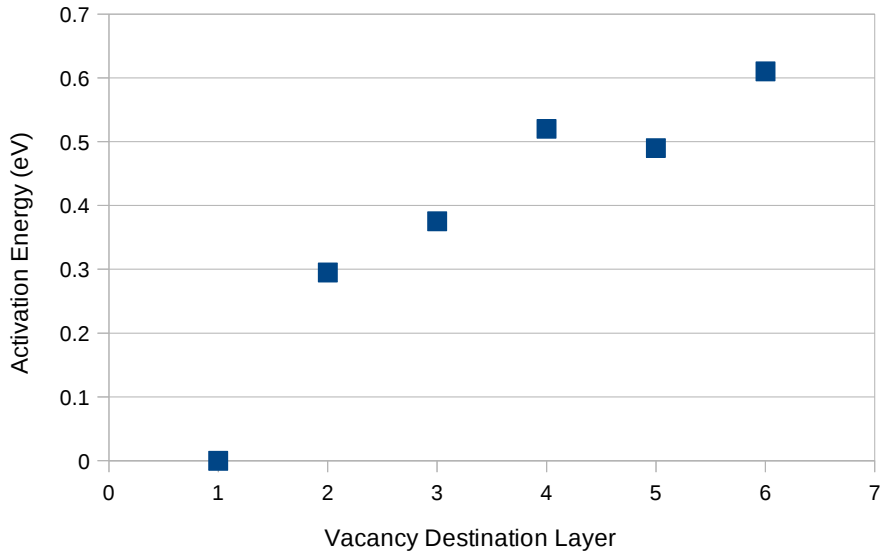

Activation energy (average of forward and reverse) plotted against depth from the surface.

(Fig. 5.2.2.2)

As can be seen in figure 5.2.2.2, activation energy appears to increase with depth from the surface within this series of results. These calculations show no difference between the optimised structure with a vacancy originating in layers 0 or 1. The vacancy will migrate with no activation barrier to the first subsurface layer (layer 1), with the vacancy most stable in the first subsurface layer.

DFT has also been applied to a sample of three migrations in the top oxygen layers using equivalent arrangements to the potentials based calculations and with results similar to those found using the inter-atomic potentials. Oxygen vacancies created in layers 0 and 1 relax into equivalent structures, with the vacancy resting in relaxing without barrier in to the first subsurface layer. Migration between layers 1 and 2 found an activation energy of 0.41eV, slightly higher than with the potentials model. The equivalent migration in between layers 5 and 6 yielded an activation energy of 0.61eV. The DFT calculations were performed to provide increased confidence in the results based on inter-atomic potentials and support the same conclusions.

5.2.4 Discussion

The range of activation energies found in the preliminary experiments using a fixed linear path model falls well outside reasonably expected values based on reported[1-6] experimental and computational studies. The way in which the migrating ion interacts with the lattice, which is distorted around its forced linear path, results in greater lattice disruption and shorter inter-atomic distances at the transition state than might be expected to be realistic or are found using the NEB method. The preliminary results do suggest a decreased activation energy nearer the surface, but a more sophisticated approach was needed to further investigate any effect.

The results of NEB calculations also appear to show a trend of reduced activation energies as the surface is approached. The activation energies fall within a reasonably expected range, with the deeper migrations in the range of 0.4 to 0.8eV as is generally found for bulk YSZ materials in experimental and computational

investigations[1-6]. The values found should not be directly compared to the two special cases of bulk migration explored in this chapter since they are unusual, being in carefully controlled isolated defect arrangements. The nearer surface paths (layers 2 and 3) show reduced activation energies of less than 0.4eV, which would suggest that there is indeed a reduced activation energy requirement for ionic conduction very close to the surface of YSZ materials.

It must be noted that this model takes no account of yttrium surface segregation. Ins the model systems explored yttrium is distributed the slab in an equivalent position relevant to the vacancy, without any preference for the surface layers. There is good evidence[11-15] (see chapter 2) that surface segregation of yttrium does occur in YSZ materials, enriching the near surface region relative to the bulk. There is also evidence, both from this study (section 5.1) and the work of others[14-18] that high yttrium concentrations can 'trap' oxygen vacancies, greatly increasing the activation energy for them to migrate. It may be the case that the effects of enhanced mobility at surfaces and yttrium segregation leading to reduced mobility are in competition with the overall effect depending on the yttrium concentration and degree of segregation.

The results of DFT calculations are comparable with the findings discussed above, suggesting a reduced migration activation energy at the (111) terrace surface relative to the bulk. Partitioning and summation of charges is performed using the Bader method (see chapter 3), which shows that the surface is slightly less ionic than the bulk. The following numbers all refer to pure ZrO_2 (111) surfaces or bulk. Oxygen has a partial charge of -1.67 in layer 0 compared to -1.73 in the bulk, while zirconium has a partial charge of +3.43 in the first layer from the surface and +3.46 in the bulk. Reduced ionicity can be explained as an effect of reduced coordination at the surface and also slight geometry changes. The Bader analysis also shows a slight change in the charge of a migrating oxygen ion. For the NNN migration within the bulk YSZ system the migrating oxygen ion is more negative at the approximate transition state relative to the end points by -0.04. The oxygen ion is at its closest approach to two zirconium ions and draws more electron density away from them as opposed to sharing more election density with them through covalent interactions which would reduce the charge.

Both DFT and potentials models show that oxygen vacancies are not stable in the terminating surface oxygen layer (layer 0), instead they will change places with an oxygen from the layer below (layer 1) without an activation barrier. Surface cations have reduced coordination numbers at the surface relative to the bulk (7 vs 8). The proximity of vacancies can reduce the coordination further resulting in an energetically unfavourable arrangement.

5.3 Conclusions

The results presented in this chapter strongly suggest that, at least when yttrium segregation is not pronounced, there is a reduction in the activation energy for oxygen vacancy migration as the surface is approached. The same conclusion is suggested using both a large random sampling with fixed linear paths and a carefully constructed set of NEB calculations, with yttrium in equivalent positions relative to each migration path.

Close proximity to yttrium (NN relationship) is shown to greatly increase the activation energy in the bulk, thus trapping the vacancy. The trapping of vacancies would appear to account for the reduction in overall oxygen conduction rates reported in the literature as yttrium concentration is increased[1-5]. Yttrium surface segregation may act through this mechanism to counter the increased surface mobility reported in this chapter.

It is observed, in both interatomic potentials and DFT models, that oxygen vacancies in the first and second oxygen layer will be lead to the same configuration spontaneously and without activation barrier once energy minimisation is applied.

References

[1] A. Ioffe, D. Rutman, S. Karpachov, *Electro. Chem. Acta.* 23, 141, **1978** .

[2] S. Badwal, *Solid State Ionics*. 52, 23, **1992**.

[3] R. Krishnamurthy, Y. Yoon, D. Srolovitz, R. Car , *J. Am. Ceram. Soc*. 87, 1821, **2004**.

[4] M. Khan, M.S. Islam, D. Bates, *J. Mater. Chem*. 8, 2299, **1998**.

[5] M. Kilo, R. Jackson, G. Borshardt, *Philos. Mag.* 83, 3309, **2003**.

[6] V. Zavodinsky, *Phys. Solid State.* 46, 453, **2004**.

[7] G. Balducci, J. Kaspar, P. Fornasiero, M. Graziani, M.S. Islam. J. *Phys. Chem. B.* 102, 557, **1998**.

[8] S. Gernard, F. Cora, C.R.A. Catlow, *J. Phys. Chem. B.* 103, 10158, **1999**.

[9] A. Bernasik, K. Kowalski, A. Sadowski, *J. Phys. Chem. Solids.* 63, 233, **2002**.

[10] X. Xia, R. Oldman, C.R.A. Catlow, *J. Mater. Chem*. 22, 8594 , **2012**.

[11] X. Xia, R. Oldman, C.R.A. Catlow, *Chem. Mater.* 21, 3576, **2009**.

[12] J. Zhu, J. G. van Ommen, J. Henny, M. Bouwmeester, L. J. Lefferts, *J. Catal*. 233, 434, **2005**.

[13] A. Eichler, G. Kresse, *Phys. Rev. B.* 69, **2004** .

[14] G. Ballabio, M. Bernasconi, F. Pietrucci, S. Serra, *Phys. Rev. B.* 70, **2004**.

[15] C. Stanek, R. Grimes, M. Rushton, K. McClellan, R. Rawlings, *Philos. Mag. Lett.* 85, 445, **2006**.

Chapter 6. Surfaces and Oxidant Activation

This chapter addresses the catalytic reactivity of YSZ materials, examining the surfaces and their physical and chemical interactions with oxidant species likely to be present in a methane reforming reactor. Surface features of the material which are potential catalytically active sites are discussed and characterised. The interactions with oxygen, water and carbon dioxide are investigated and discussed and the resulting activated species characterised.

6.1 The Surfaces

The surfaces of YSZ materials are discussed in chapter 2. There is good evidence[1-4], from experimental and simulation work, that the predominant surfaces will be (111) oxygen terminated terraces, which may include relatively low energy step defects. The (111) terrace and a step defect surfaces are those which will be used in this thesis. The step configuration pictured (Fig. 6.1.1) is the lowest energy topographic 3D surface arrangement predicted by Xia et al[4].

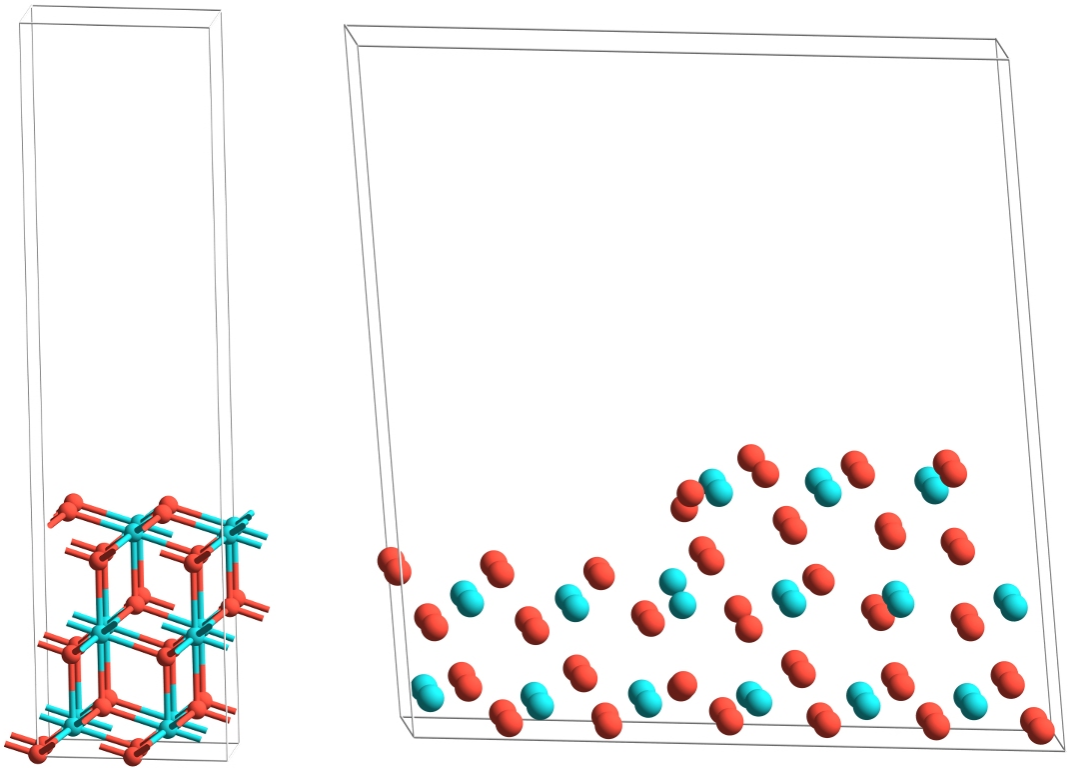

The (111) terrace (left) and step (right) surfaces of cubic zirconia. Oxygen is red, Zirconium blue.

(Fig. 6.1.1)

The catalytic properties of surfaces of yttrium doped (YSZ) materials are to be modelled, requiring the surface features likely to result from introduction of yttrium ions and oxygen vacancies to be determined. Xia et al[5] have studied preferred arrangements of Y-V-Y defect clusters in the surface region, providing a

good starting point for this work. Calculations of surface defect arrangements were performed to confirm the model of Xia et al[5] and explore the stability of different arrangements in the surface model.

A systematic exhaustive exploration of possible arrangements of a single Y-V-Y defect within the (111) terrace surface slab model was performed using the interatomic potentials model introduced in chapters 3 and 4. The Site Occupancy Disorder (SOD)[6] package was used to generate all possible configurations. As the surface slab does not correspond to a symmetry group recognised by the SOD package redundant symmetrically equivalent configurations were generated. However, the total number of configurations was still manageable, and when oxygen vacancies were restricted from being placed in the lowest fixed layer, a total of 264 structures were calculated. The configurations were geometry optimised using the BFGS scheme under constant pressure conditions using the GULP software package (see chapter 3 for details) and their lattice energies calculated and graphed below (Fig. 6.1.2).

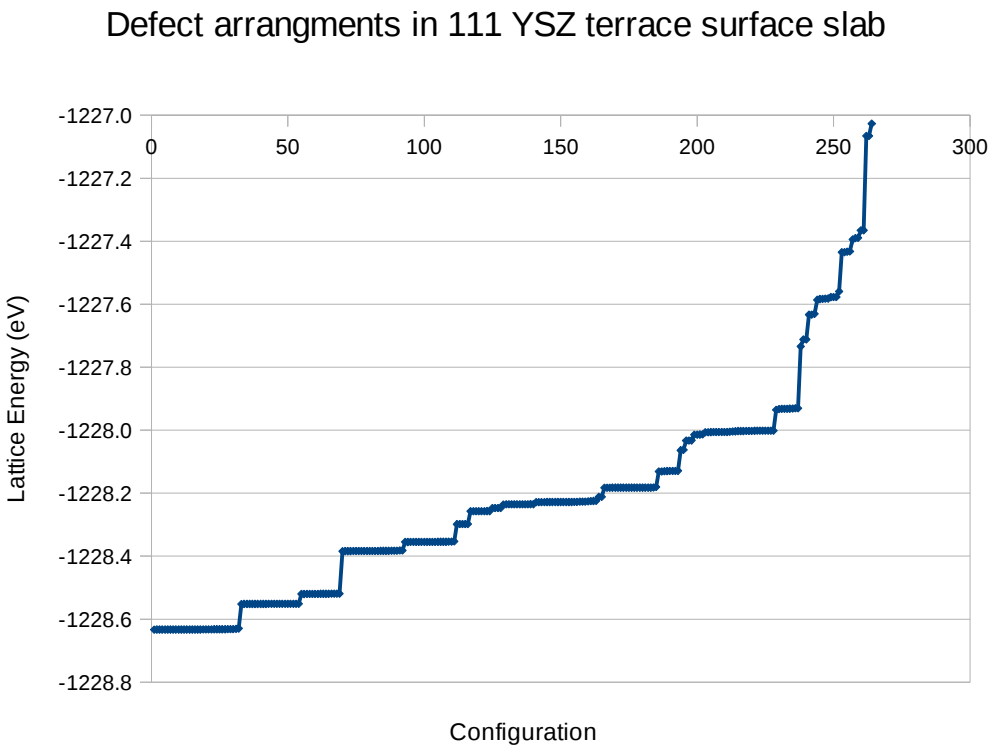

Interatomic potentials lattice energies of all possible dopant configurations in the (111) terrace vacuum-slab cell.

(Fig. 6.1.2)

It can be seen that the energies for all possible configurations span a range of approximately 1.5eV. The results displayed in Fig. 6.1.2 contain symmetrically equivalent structures due to a limitation in how the SOD software handles surfaces. The most stable arrangements all place the vacancy in the top two oxygen layers and the yttrium ions in NN or NNN relationships to the vacancy. The reasons for the preference for NN and NNN relationships as well as the preference for the vacancy to be near the surface are discussed in chapters 2 and 4. The surface models used in subsequent work were chosen for their relative stability and are optimised using GGA DFT as implemented in the VASP software package. The surface models selected are visualised in figure 6.2.1.

6.2 Potential Active Sites

The oxygen terminated 111 terrace and step surfaces of YSZ present several sites which may have roles in catalytic activity. This section will discuss their properties before further sections explore their interactions with a variety of substrate molecules.

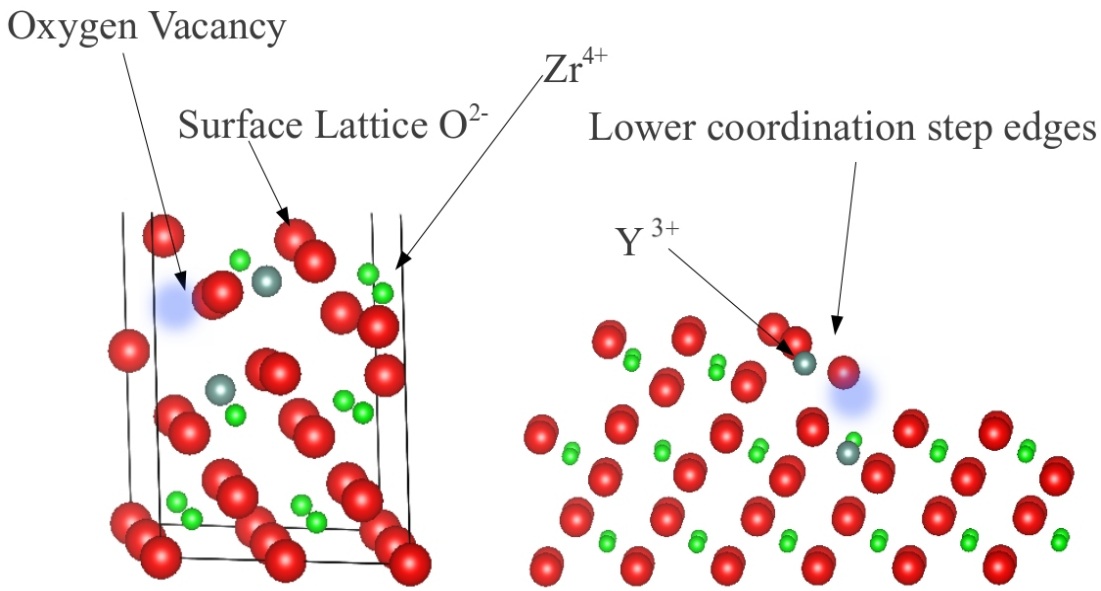

The surface sites presented at the 111 terrace and step YSZ surfaces. Zirconium is green, oxygen red, grey yttrium. Transparent blue regions are approximate vacancy locations.

(Fig. 6.2.1)

The simplest surface sites are the zirconium and oxygen ions present on any zirconia or YSZ surface. The zirconium and oxygen ions in this material are formally described as Zr^{4+} and O^{2-} respectively, the real electron density distribution will differ from the formal charges and will not be constant between the surface and the bulk material. In order to investigate the charge distributions around surface sites electronic structure calculations were performed on the pure ZrO_2 terrace and step surface slab models.

The surfaces are modelled as a vacuum-slab system, as described in previous chapters, applying DFT with a GGA functional (PW91[7]). A plane wave cut off energy of 500eV for the plane wave basis set and 3x3x1 Monkhorst-Pack k-point

spacing is used for all DFT surface models reported here. Calculations are carried out using the VASP[8-9] software package using the included PAW pseudo-potentials (see chapter 3). The structures are geometrically optimised by means of a conjugate gradients energy minimisation method, with the lowest oxygen and zirconium layers fixed in positions equivalent to those in the bulk. Calculated electron density distributions are analysed using the Bader technique (see chapter 3 for more information) to partition the distribution and give ionic charges for the various surface ions.

The charges of the terrace surface derived by Bader analysis show a slight reduction in ionicity at the surface. The first layer of oxygen atoms has a mean charge of -1.67, compared to -1.73 in the bulk material. The first layer of zirconium has a charge of +3.42, slightly lower than the bulk value of +3.46. The subsequent layers then oscillate being slightly above or slightly below the bulk values, with the difference being smaller deeper in to the slab. In order to determine the extent of this effect it would be necessary to model a thicker slab, since the apparent decay of the alternating layers of increased or reduced ionicity is based on a thin two sided slab model, so there are insufficient layers to give any meaningful quantitative analysis of the effect.

The process outlined above for ZrO_2 surfaces was repeated for YSZ surfaces using the same parameters for electronic structure calculations. The oxygen vacancy and corresponding yttrium ions are crucial features; their effect on electron density is discussed and depicted below (Fig. 6.2.2).

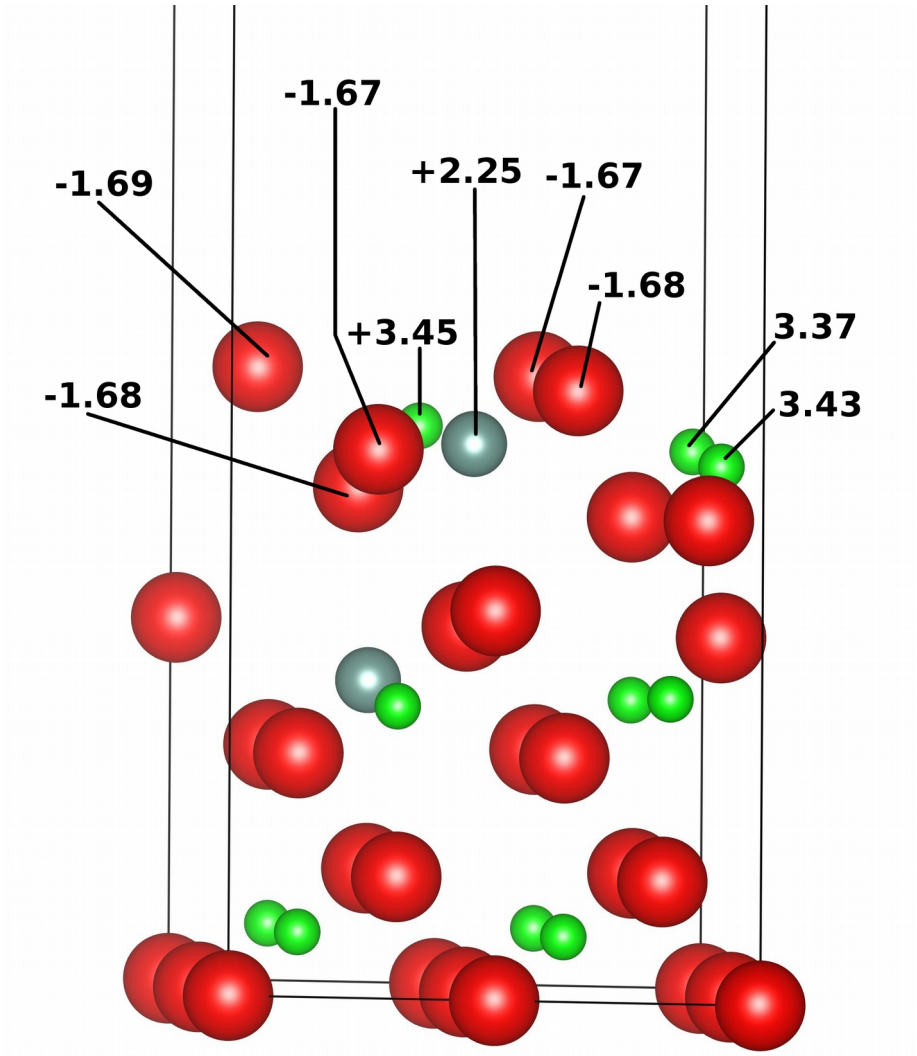

Partial charges from GGA-DFT modelling and Bader analysis in the region near a terrace surface oxygen vacancy. Oxygen is red, zirconium green and yttrium grey. (Fig. 6.2.2)

As can be seen, the introduction of dopants and a vacancy does have some effect on the charge distribution. However, the effect is relatively small with the variation not exceeding ±0.02 for the oxygen anions and ±0.05 for the zirconium cations. The small disruption to electron density is as would be expected in a stable surface, whereas large changes would indicate unfavourable electronic states for the ionic species present. The activity of the surface sites is not readily apparent from a simple analysis of their ground state charge distribution and is better probed through examination of their interactions with substrate molecules.

The HSE06 hybrid functional enhanced DFT technique was applied to the YSZ surface slab model. The HSE06 functional was used with the PBE GGA DFT functional augmented with 25% HF exchange within a range separation screening parameter of 2.07Å. The PAW pseudo-potentials developed for use with the PBE functional in the VASP software package were used.

Since HSE06 predicts slightly different bulk lattice constants from PW91 GGA DFT (5.10Å vs 5.12Å – see section 4.1) it was necessary to construct and optimise a model of the bulk lattice before using the output configuration to cleave the appropriate surface. The surface model, once optimised, shows a similar but not identical surface geometry to GGA-DFT. The charge distribution of the surface was subjected to a Bader analysis, the results of which are labled for surface ions on the visualisation (fig. 6.2.3) below.

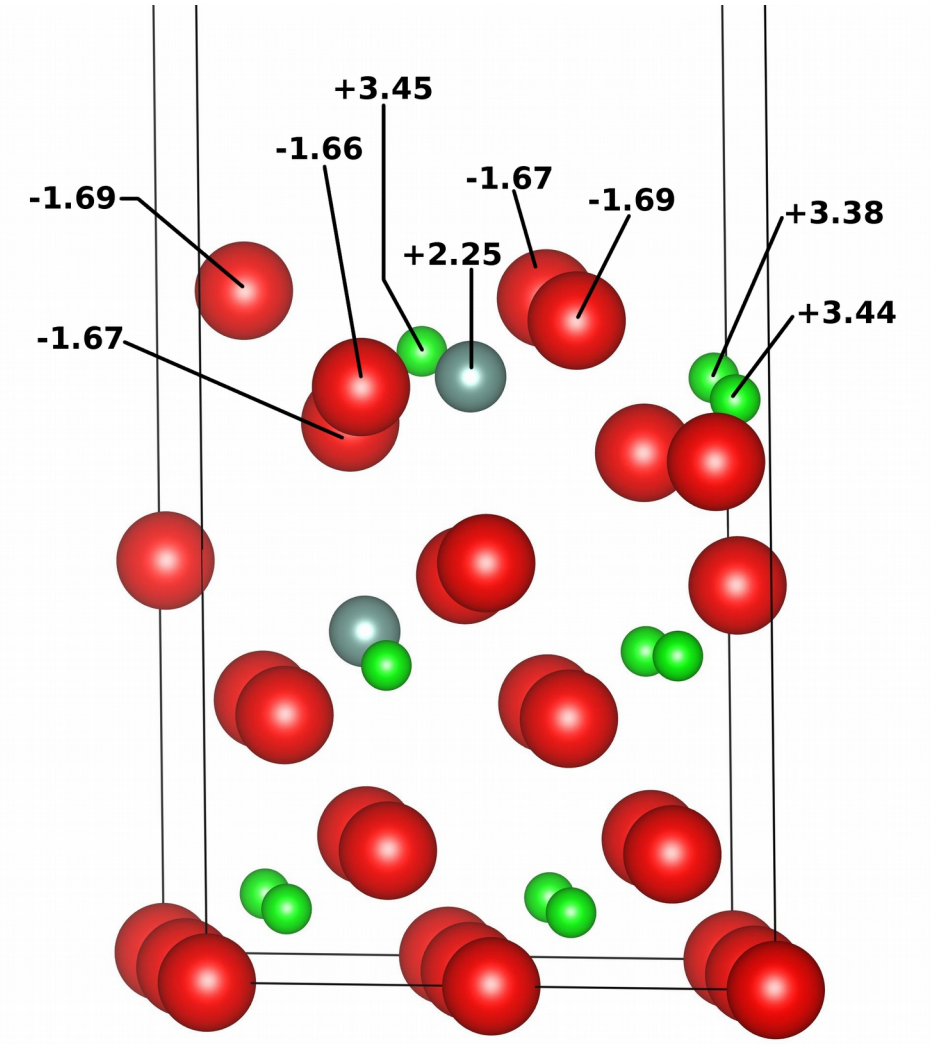

Partial charges from Bader analysis in the region near a terrace surface oxygen vacancy as predicted by the HSE06 hybrid functional. Oxygen is red, zirconium green and yttrium grey.

(Fig. 6.2.3)

As can be seen from a comparison of figures 6.2.2 and 6.2.3, generated from GGA DFT and HSE06 models respectively, the two methods yield very similar configurations and electronic distribution for the YSZ surface vacuum-slab model. The maximum ionic Bader charge difference found in this model is ±0.02 electron equivalents. The differences in the models are too small to draw conclusive trends, but it does appear that HSE06 tends to predict a very slightly more ionic electronic structure, oxygen anions on average being marginally more negative in the HSE06 model and the converse being true for zirconium and yttrium cations. Greater differences between the models may become apparent when adsorbed species and reactivity are considered.

6.3 Oxidants

Autothermal reforming may involve a number of potential oxidants. The most obvious is molecular oxygen, introduced as one of the feed gasses. It will largely be consumed in partial or complete combustion reactions in the gas phase before reaching the catalyst bed, but its interactions with the YSZ surface are still of great interest. Water (steam) is present, both as a feed gas and as a product of combustion. Water can act as a source of oxygen and yield one of the product gasses, hydrogen. Carbon dioxide is likewise present in the reacting gas mixture as it flows over the catalyst bed as a product of combustion. In order to yield CO as a product CO_2 must have an oxygen removed by another reaction. Both water and carbon dioxide are very stable molecules and their activation over catalytic surfaces is of great interest in steam reforming, dry reforming and various carbon capture processes.

6.3.1 Oxygen

The interactions of gas phase oxygen with YSZ surfaces has been modelled using DFT techniques by Xia et al[4] and others have carried out experiments[10-11], as discussed in chapter 2. There is good evidence to support favourable physisorption of molecular oxygen from the gas phase on ZrO_2 and YSZ terraces and steps and a strong physisorption on some Y-V-Y defect configurations. There is also evidence supporting the creation of superoxide like species from molecular oxygen at YSZ step edge vacancies and some terrace Y-V-Y configurations. The configurations explored by Xia et al[4] provided the starting point for exploration of the surface oxygen species in this thesis.

The interactions between molecular oxygen in the gas phase and surface oxygen vacancies have been studied using both GGA-DFT and HSE06 hybrid DFT. A vacuum-slab model of the surface is used, and for GGA-DFT the same parameters as previously described are applied. Two dopant configurations in the terrace and one in the step have been considered. The step and one of the terrace configurations give rise to superoxide like (O_2^-) species, while the second terrace configuration simply allows for a fairly strong physisorption. The two superoxide surface species are shown below, with the O-O distance labelled and an unpaired electron density

isosurface showing unpaired electron density (Fig. 6.3.1).

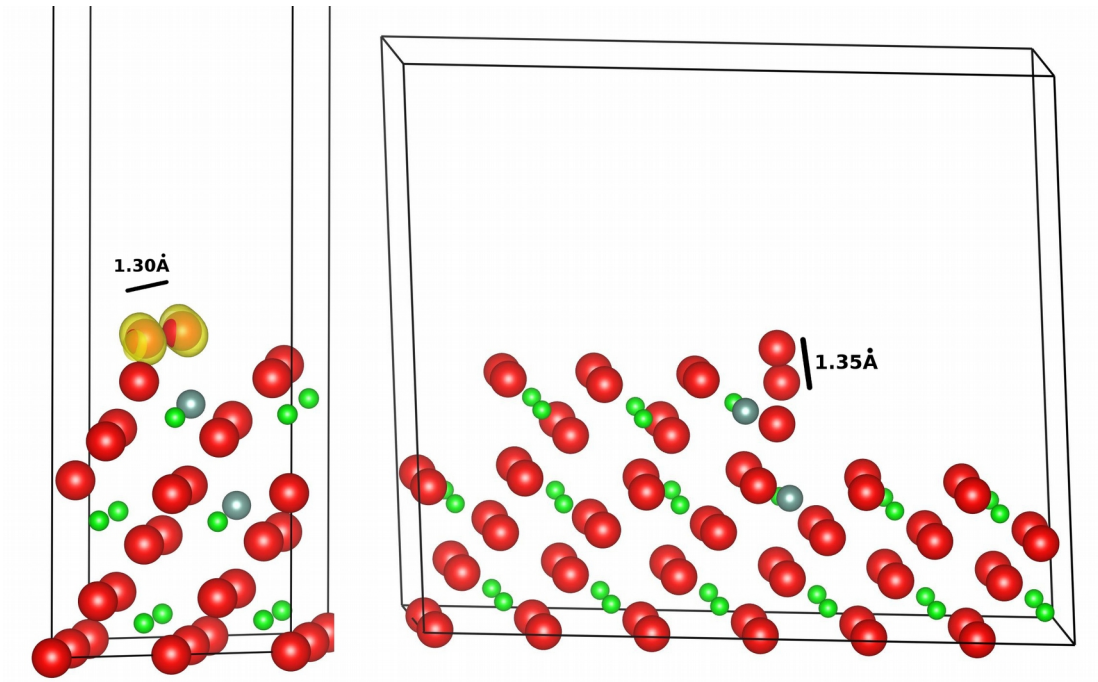

Superoxide like species on YSZ terrace as predicted by GGA-DFT (left, with electron spin density isosurface) and step (right, without spin isosurface). (Fig. 6.3.1)

As can be seen, an approximately toroidal region of unpaired electron density can be seen around each atom in the superoxide ion. This electron density can be attributed to the occupation of a π^* antibonding orbital with electron density transferred form the surface vacancy region. The occupation of the antibonding orbital is also responsible for the lengthening of the O-O bond from approximately 1.21Å in molecular O_2.

A Bader analysis was performed on the electron density distribution for the superoxide containing terrace system. The O_2 species has an overall charge of -0.57, somewhat less than the charge of -1 that is formally assigned to the isolated superoxide ion. However, it is clear that there has been substantial electron density transfer from the surface to the oxygen molecule. In the case of the step system the Bader charge on the superoxide like species is higher at 0.91 and in combination with the greater O – O bond length, is indicative of the complete transfer of a single electron to create a true superoxide species.

It can be concluded that gas phase molecular oxygen can be reduced to

superoxide by electron transfer from oxygen vacancy sites present in some YSZ configurations. The overall reaction energies were found to be favourable (-0.47eV and -0.73eV for the terrace and step respectively). These results are in agreement with the work of Xia et al[4] who's models they are aim to replicate as a foundation for further work.

The HSE06 hybrid functional with 25% HF exchange contribution and a range separation parameter of of 2.07Å was applied to oxygen adsorption over the 111 YSZ terrace surface. The surface model described in section 6.2 was used, with an oxygen molecule placed above the vacancy in an equivalent position to that predicted by the GGA DFT model described elsewhere in this section. The model was then geometry optimised, yielding results significantly different from those of the GGA DFT model. It should be noted that the structural optimisation convergence criteria for this model were relaxed to 0.025eV in order to reduce the computational resources required for this demanding model. The O – O bond length is 1.23Å, slightly greater than that of molecular oxygen (1.21Å) but significantly less than seen for the superoxide like entities predicted by GGA DFT models. The nature of the O_2 species can be better understood by visualising the unpaired electron density distribution, such a diagram is provided below in figure 6.3.2.

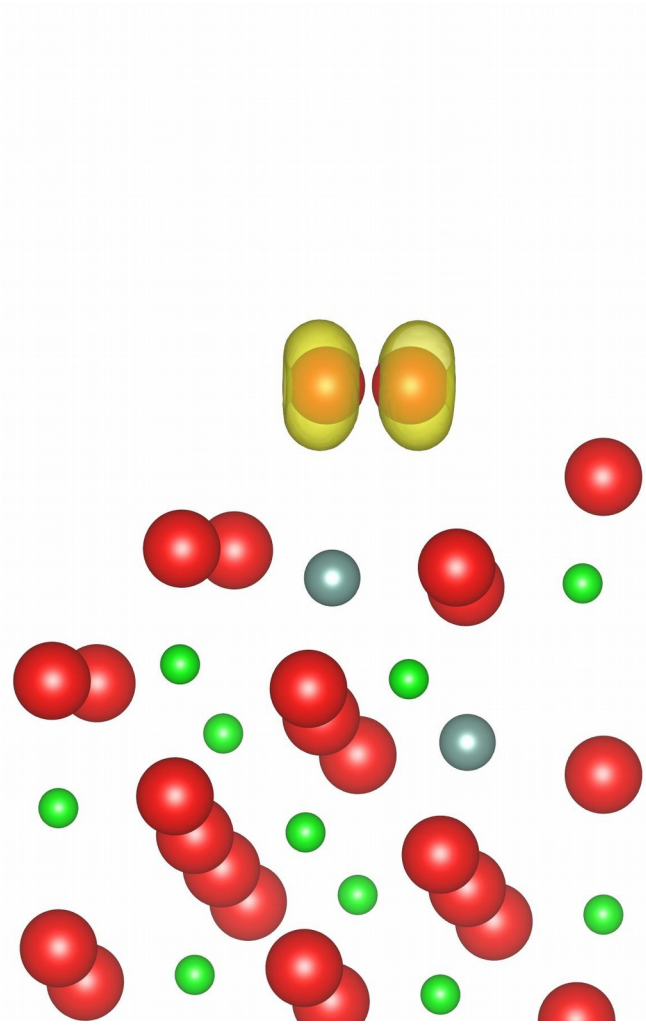

Unpaired electron density isosurface (yellow regions) and structure of superoxide like oxygen species on YSZ as predicted by the HSE06 hybrid functional DFT. Oxygen is red, zirconium green and yttrium grey.

(Fig. 6.3.2)

Figure 6.3.2 shows distinctly the two parallel toroidal regions on unpaired electron density, one on each oxygen of the O_2 entity. These regions represent electron density in the O – O anti-bonding orbital and are characteristic of a superoxide like radical species. However, when compared with those predicted by GGA-DFT at the same density isosurface level the regions are somewhat smaller. It is also worthy of note that the GGA-DFT model predicts significantly greater unpaired electron density distributed between several oxygen ions in the system relative to HSE06 hybrid DFT.

A Bader charge analysis was performed on the HSE06 model electron density distribution. The Bader analysis assigns a charge of -0.14 to the O_2 entity. The charge

is further supporting evidence that the HSE06 hybrid DFT method yields a significantly less reduced O_2 species than GGA-DFT. Due to the computational expense of HSE06 hybrid DFT calculations on this type of system it has not been possible characterise as wide an array of reactions using the methodology as with GGA-DFT. In most subsequent cases GGA-DFT is the sole electronic structure method employed in generating the results presented.

According to the GGA-DFT model, the adsorption of molecular oxygen and creation of the superoxide like species occurs without a distinct activation barrier. It may be reasonably assumed that if molecular oxygen is present in the gas phase at reaction temperatures it will readily form superoxide like adsorbed species over surface oxygen vacancy sites. The reactions in which surface oxygen species participate are discussed in subsequent sections.

6.3.2 Water

Water is a significant source of oxygen in autothermal reforming, as well as steam reforming of methane (SRM) and water-gas shift (WGS) processes. Additional water can be produced as a product of combustion before the gas reaches the catalyst bed in an ATR. The interactions between water and the YSZ surface features are discussed in this section. Water is a polar molecule, the oxygen drawing some electron density from the hydrogen. The polar water will interact with most ionic materials, aligning to maximise the proximity of oxygen to cations while positioning the hydrogen close to anions. In the case of pure ZrO_2, it would be expected that oxygen would adsorb with the oxygen above zirconium and the hydrogen aligned with surface oxygen. Due to the mismatch between inter-ionic distances and water bond lengths and angles, it would also be expected that the alignment would be imperfect and that some distortion of the water molecule would occur. In the case of YSZ the presence of vacancies further complicates the situation. Modelling work was therefore carried out to explore the water – YSZ interactions.

The vacuum-slab surface model was used as in previous sections and calculations carried out using GGA-DFT as implemented in the VASP software package with the same parameters as in previous sections (500eV cut-off, 3x3x1 K-point mesh). Surface sites were probed by constructing the input coordinates with

a water molecule close (~1.5Å) to the site of interest and then carrying out a geometry optimisation. A model with the water molecule in the centre of the vacuum gap was used as a reference. The reference model results in a symmetrical O-H bond length of 0.97Å and a H-O-H bond angle of 104.5º, close to the accepted experimental values of around 0.96Å[12] and 104.5º[12]. A Bader analysis of this structure confirms that the model molecule has no overall charge and that much of the electron density being resident on the oxygen.

Water can undergo a several different interactions with the surface, the strongest that has been found having a reaction energy of -0.98eV. The interaction site and adsorbed species is visualised below (Fig. 6.3.2.1).

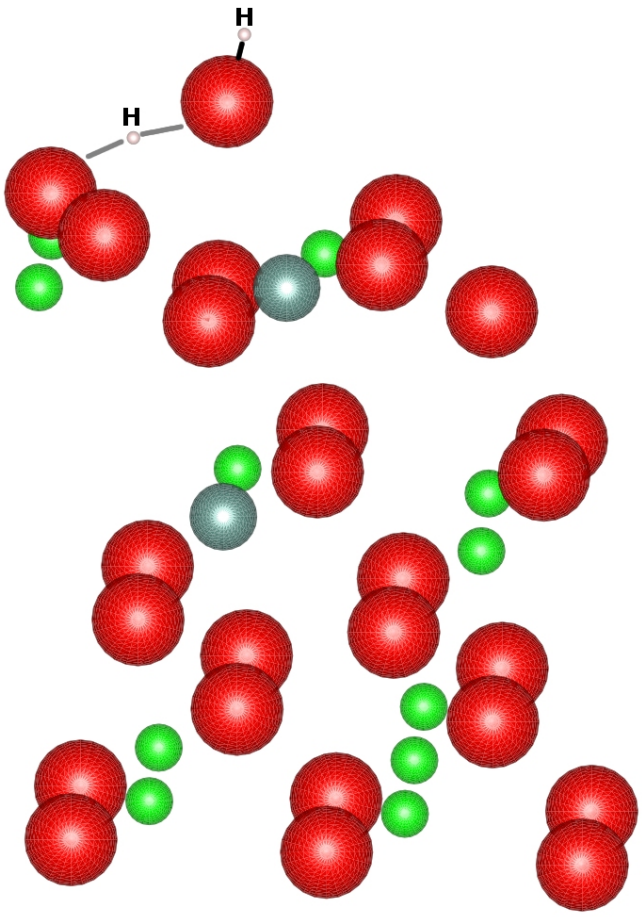

Visualisation of water derived species on YSZ terrace surface from GGA-DFT. Oxygen is red, zirconium green, yttrium grey and hydrogen light brown. (Fig. 6.3.2.1)

The structure visualised in Fig. 6.3.2.1 has the O-H bond lengths within the original water molecule that are no longer symmetrical; the bond to the hydrogen furthest from the surface is almost unchanged at 0.97Å while the other bond has lengthened to 1.22Å and this hydrogen is shared fairly evenly with a surface oxygen ion. The O-H bond length between the surface oxygen and the shared hydrogen is 1.21Å. The H-O-H angle in the water residue is 114.9º and the O-H-O-H arrangement forms a dihedral at 145.7º. When subjected to a Bader analysis it can be seen that single bonded hydrogen has almost no electron density assigned by GGA DFT, much as in the isolated water molecule. The shared hydrogen has a much increased electron density, with a partial charge of +0.62. The central oxygen has a partial charge of -1.77, 0.32 less negative than in the isolated model. According to the Bader analysis of the electron density distribution generated by the DFT model, a total of 0.06 electrons have been transferred to the water molecule from the surface oxygen. Electrons being shared through covalent interactions are harder to quantify, but will play a significant role in the bonding. This interaction could be considered as too strong (0.98eV) to be properly characterised as a hydrogen bond since it is the complete sharing of a hydrogen, the shared hydrogen is actually marginally closer to to the surface oxygen. It has not been determined which of the hydrogen sharing O – H bonds is the stronger.

The NEB method was applied to the hydrogen sharing interaction, with a set of 7 evenly spaced linearly interpolated images moving the water molecule from 2Å above the surface to the final hydrogen sharing state seen in figure 6.3.2.1. The output did not show an activation barrier, but rather a very flat energy profile, followed by a monotonic increase in stability as the water is moved closer to the surface. The energy profile indicates that there is no substantial barrier to the hydrogen sharing interaction, it will occur readily if water approaches the surface site closely in the correct orientation.

Water will also form weaker hydrogen bonding interactions with the surface without any significant activation barrier, found by energy minimisation if its initial position is closer then ~2.5Å to a suitable surface site. A typical hydrogen bonding interaction is visualised below (Fig. 6.3.2.3), the strengths of these exothermic interactions vary from approximately 0.2 to 0.5eV depending on the location on the surface.

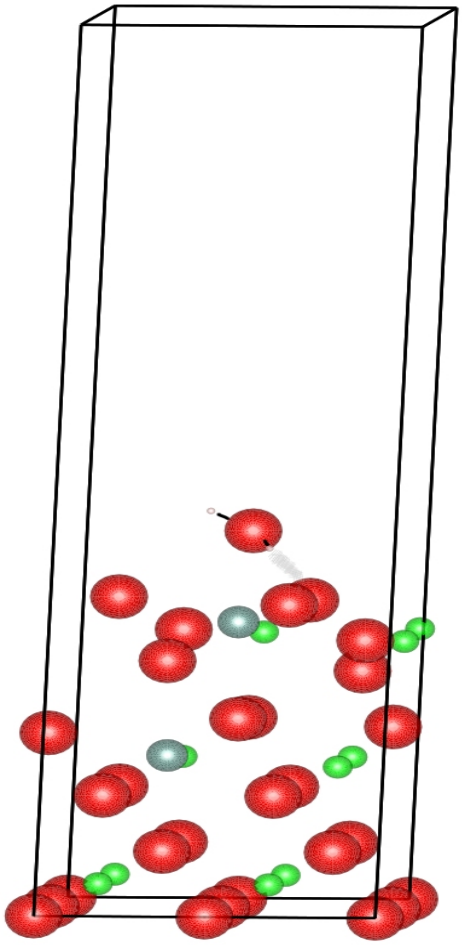

Visualisation of a water molecule hydrogen bonded to terrace YSZ surface oxygen as predicted by GGA-DFT. Oxygen is red, zirconium green, yttrium grey and hydrogen light brown.

(Fig. 6.3.2.3)

The O-H bonds in this case are 0.97Å and 1.02Å for the non-bonding and hydrogen bonding hydrogen atoms respectively. The length of the hydrogen bond is 1.66Å and the H-O-H angle is 108.5°. This is a fairly typical hydrogen bond between a metal

oxide material and water.

6.3.3 Carbon Dioxide

Carbon dioxide is present in significant quantities in the gas reaching the catalytic bed in an autothermal reformer, produced by combustion in the initial reactor space. In dry reforming CO_2 is the primary oxidant. The interactions between CO_2 and YSZ surface sites are significant for the understanding of reforming processes, especially dry reforming, over these materials.

In order to probe the interactions between carbon dioxide and YSZ surface features a molecule of carbon dioxide was placed in a grid of positions over a slab model of the YSZ (111) terrace surface. The structures were then geometry optimised using GGA DFT and conjugate gradients energy minimisation as implemented in the VASP software package. A system in which carbon dioxide is placed in the vacuum gap distant from the surface was constructed to provide a reference energy.

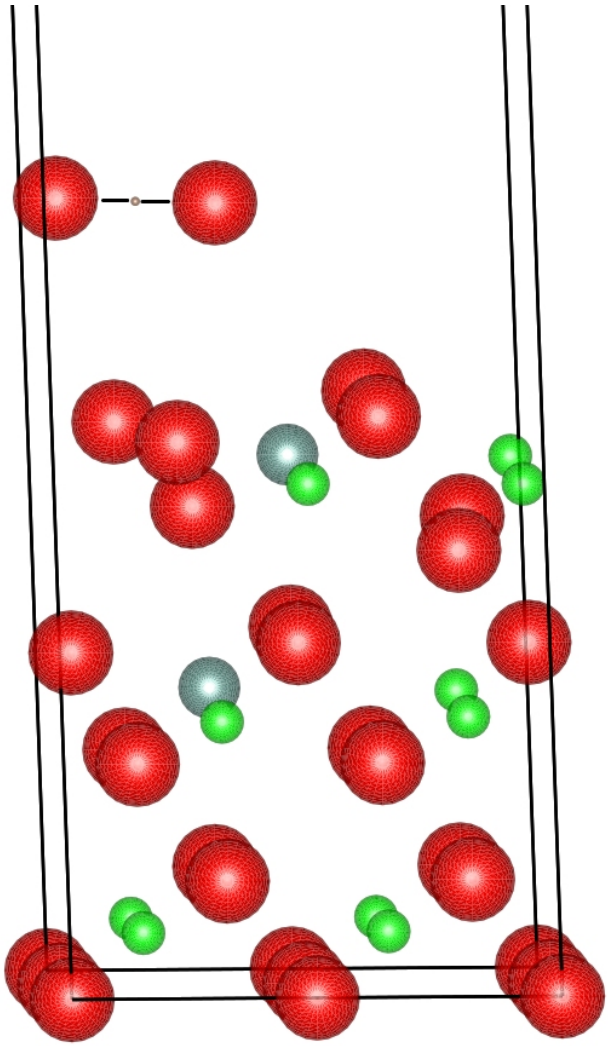

Visualisation of the GGA-DFT relaxed reference structure, with carbon dioxide distant from the YSZ (111) terrace surface slab. Oxygen is red, zirconium green, yttrium grey and carbon light brown.

(Fig. 6.3.3.1)

As can be seen in figure 6.3.3.1, carbon dioxide is a linear molecule with an O–C–O angle of 180°. Symmetrical O-C distances of 1.176Å are predicted by the DFT model, slightly longer than the experimental values of 1.163Å[13]. A relaxed equilibrium distance of approximately 2.5Å above the surface is found, with the molecule's long axis being aligned approximately parallel with the plane of the surface, the carbon approximately centred above a surface oxygen ion and the two oxygen atoms aligned towards surface zirconium ions. The arrangement observed here could be regarded as a physisorbed state, being approximately 0.12eV more stable than a position approximately 6.5Å from the surface.

By moving the initial carbon dioxide position closer to the surface than the 2.5Å found for the physisorbed species it is possible to find stronger favourable carbon dioxide – surface interactions. The relaxed structure resulting from a strong carbon dioxide – surface interaction is visualised below.

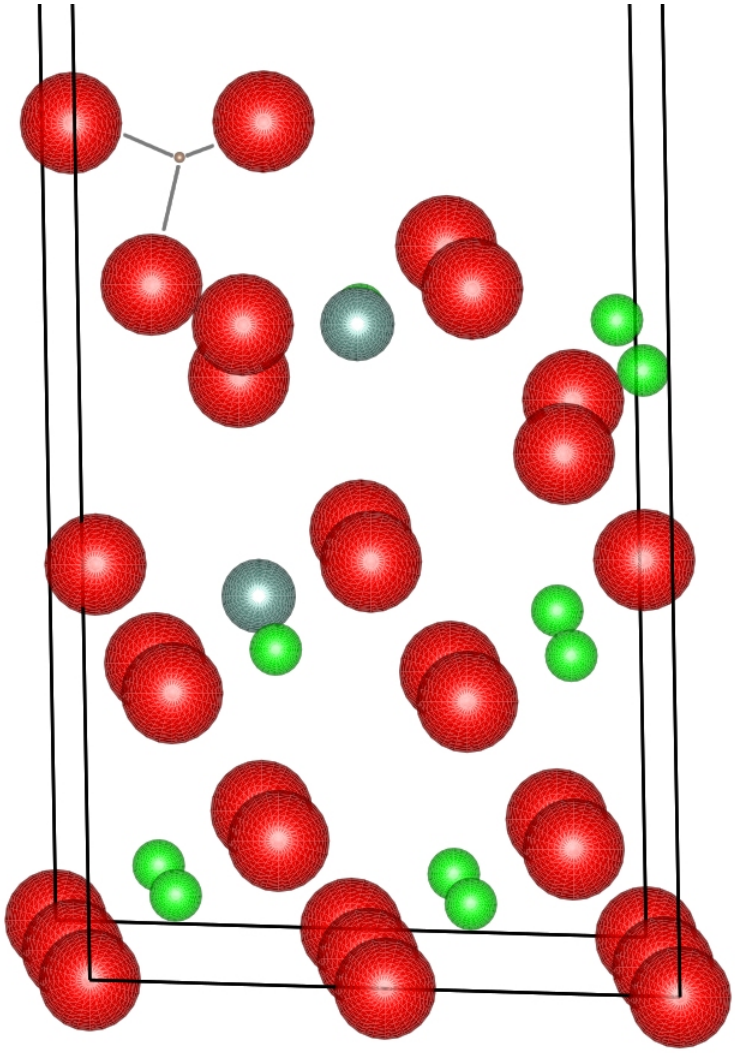

Visualisation of a GGA-DFT relaxed structure formed by carbon dioxide – YSZ surface interaction. Oxygen is red, zirconium green, yttrium grey and carbon light brown.

(Fig. 6.3.3.2)

As can clearly be seen, the resultant species is significantly different from the originating carbon dioxide molecule. The carbon now has strong interactions with three oxygen atoms; two are part of the initial carbon dioxide molecule while the third is a surface oxygen anion. The distance between the carbon and initial two

oxygen atoms has lengthened to approximately 1.25Å from 1.18Å in the physisorbed molecule and a third oxygen in the YSZ surface is at a distance of 1.41Å. The bond angles have change significantly from a linear molecule to an approximately triangular planer species. The O – C – O angle between the two original oxygen atoms is approximately 113° and between either of the original oxygen atoms and the surface ion is approximately 133°. The species seen here resembles a perturbed carbonate (CO_3^{2-}) ion, with symmetry reduced by the surface originated oxygen bond being longer and the angles not being equal.

In order to understand better the electronic properties of the carbonate like species, a Bader analysis can be used to partition the electron density distribution and estimate partial charge values for each atom in the system. The overall charge on the surface CO_3 entity is found to be -1.77, while the initial CO_2 molecule is neutral. This shows that along with the third oxygen, the entity has acquired additional charge density from the surface. The isolated carbonate species is formally described as 2-, close to the charge found in this surface entity. However, in the case of the chemisorbed species, the surface oxygen atom remains embedded and so not all of its electron density will be shared with the CO_2 fragment. If removed from the surface, the species would be a typical carbonate anion and adopt an equilateral triangular planer configuration. The chemisorbed carbonate-like species may be regarded as an 'activated' form of carbon dioxide and may play an important role in further reactivity. An electron density plot illustrates the shared electron density (bonding) between the CO_2 residue and a surface lattice oxygen. Such a plot is provided below in figure 6.3.3.3.

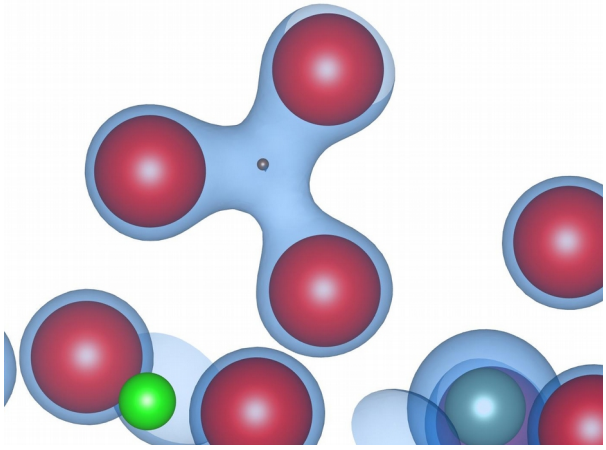

Enlargement of CO_3 entity formed from CO_2 on YSZ. Oxygen is red, zirconium green, yttrium grey and carbon light brown. The blue regions are an electron density isosurface as predicted by GGA-DFT.

(Fig. 6.3.3.3)

The electron density plot (fig. 6.3.3.3) shows sharing of electrons between the central carbon and three oxygen atoms. The upper two are part of the original CO_2, while the lower one is a surface oxygen ion neighbouring an oxygen vacancy.

The formation of the carbonate-like surface species from physisorbed molecular carbon dioxide is exothermic, the chemisorbed entity being 0.77eV more stable than the physisorbed. The presence of an activation barrier may be deduced from the fact that the physisorbed species is stable and does not spontaneously relax to the chemisorbed when energy minimisation techniques are applied. In order to assess the activation energy required, and therefore the feasibility of forming the chemisorbed entity in catalytic systems, it is necessary to find the transition state(s) and their energies relative to the reactants. A transition state search has been carried out by applying the NEB technique (see chapter 3).

NEB transition state searches result in energies and geometries for each of a set of 7 linked images on a possible reaction path between two end points. The optimised images can be loosely regarded as steps along a reaction coordinate. The energies for the transition from physisorbed to chemisorbed systems are represented graphically below (fig. 6.3.3.4).

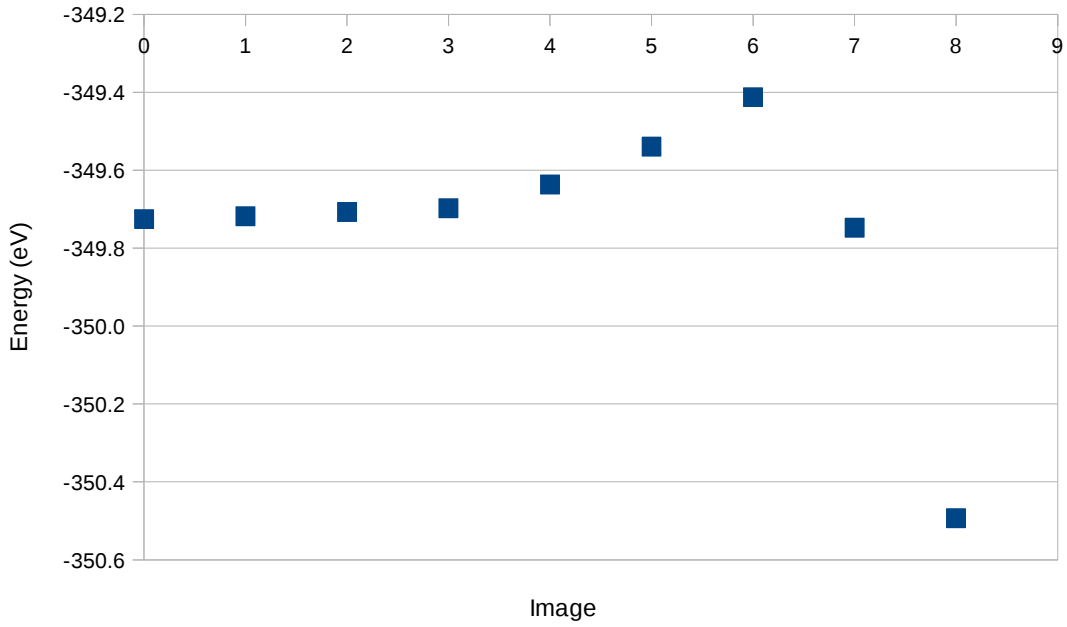

NEB energy profile

(Fig. 6.3.3.4.)

As can be seen the energy profile shows a distinct peak which can be regarded as an activation energy and the corresponding structure as the approximate transition state. The forward activation energy is 0.31eV and the reverse 1.08eV. The transition state structure is visualised below in figure 6.3.3.4.

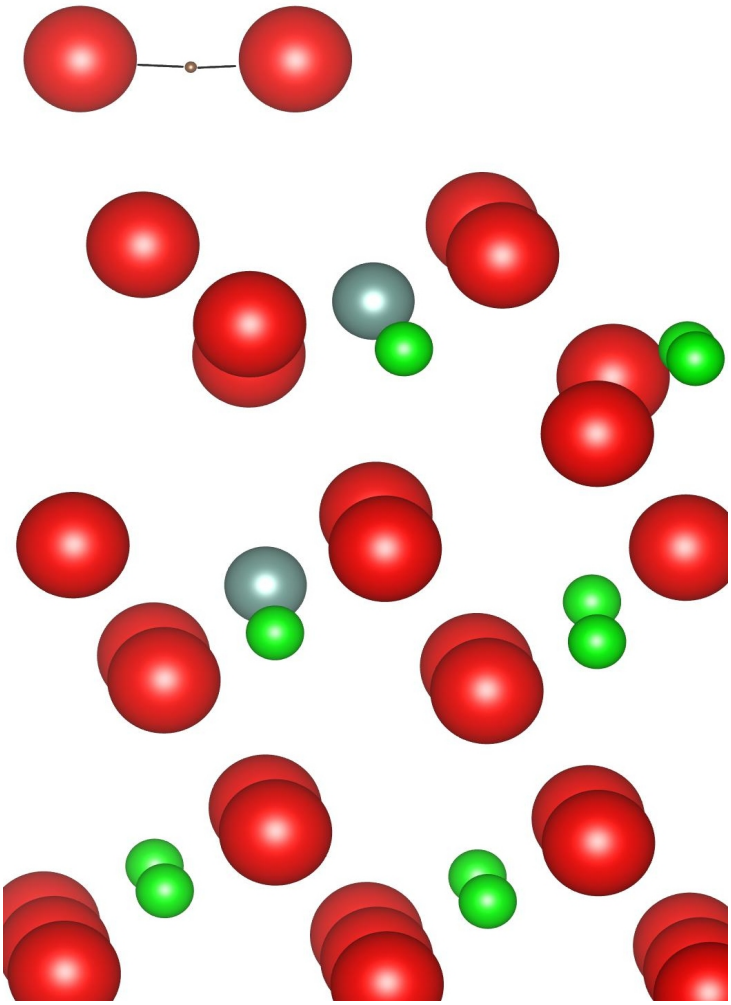

GGA-DFT transition state structure. Oxygen is red, zirconium green, yttrium grey and carbon light brown.

(Fig. 6.3.3.5)

By comparison of the transition structure (Fig. 6.3.3.5) with the initial (Fig. 6.3.3.1) and final (Fig. 6.3.3.2) it is apparent that the transition state geometry of the CO_2 species is much closer to the initial free CO_2 than to the carbonate-like product. At the approximate transition state the CO_2 molecule has simply been forced close to the surface, well beyond its equilibrium distance.

A Bader analysis of the approximate transition state shows that at this point very little electron density has been transferred, the CO_2 molecule having a charge of only -0.02. The subsequent structure (image 7) shows that the CO_2 species has assumed a bent geometry and received electron density from the surface oxygen, looking more like a carbonate species than molecular CO_2. It would appear that the activation barrier is associated with forcing the molecule close enough to surface oxygen for the electron transfer to occur.

6.4 Summary

In this chapter models of the surface features of YSZ materials have been reported, with particular attention paid to sites of potential catalytic significance. The charge distribution around surface vacancies and dopants has been described. The interactions between the surface and oxidant molecules present in methane reforming reactors have been described and modelled. Surface oxygen vacancy regions are able strongly to adsorb and activate oxygen, water and carbon dioxide.

Oxygen receives additional electron density, becoming a superoxide like radical species. Water will hydrogen bond to any oxygen site on the surface, and will undergo a full hydrogen sharing interaction near the surface vacancy site. Carbon dioxide receives electron density from the vacancy region, forming a carbonate-like species with a neighbouring surface oxygen. In each case electron density is transferred from the vacancy region via neighbouring surface ions to the adsorbate molecule in an exothermic process. The energetics of the interactions between each oxidant molecule and the surface are summarised in the table (Tab. 6.8.1) below, forward activation energy is defined as going from the gas phase to the adsorbed species.

Adsorbate	Enthalpy (eV)	Forward Activation Energy (eV)
O_2	-0.47	-
H_2O	-0.98	-
CO_2	-0.77	0.31

Summary table of oxidant adsorption energetics on 111 YSZ terrace surface. (Tab. 6.8.1)

From the predicted exothermic nature of the interactions and the activation energies considered relative to the temperatures typical of ATRs it is reasonable to assume that these interactions will occur in the real catalytic systems under reaction conditions. It should however be noted that molecular oxygen is unlikely to be present in any significant quantity in the gas mixture reaching the catalyst bed due to the input ratios and the large combustion volume between the gas injection and the catalyst bed. Molecular oxygen and its interactions may be much more significant in the first bed of the two bed experimental system employed by Zhu et al[14] since the gasses reach the catalyst bed immediatly and at lower temperatures than in a commercial ATR design. The role of 'activated' oxidant species in methane oxidation catalysis is explored in the following chapter (Ch. 7.).

References

[1] G. Balducci, J. Kaspar, P. Fornasiero, M. Graziani, M.S. Islam, J. *Phys. Chem. B.* 102, 557, **1998**.

[2] S. Gernard, F. Cora, C.R.A. Catlow, *J. Phys. Chem. B.* 103, 10158, **1999**.

[3] A. Bernasik, K. Kowalski, A. Sadowski, *J. Phys. Chem. Solids.* 63, 233, **2002**.

[4] X. Xia, R. Oldman, C.R.A. Catlow, *J. Mater. Chem*, 22, 8594 , **2012**.

[5] X. Xia, R. Oldman, C.R.A. Catlow, *Chem. Mater,* 21, 3576, **2009**.

[6] R. Grau-Crespo, S. Hamad, C.R.A. Catlow, N. de Leeuw, *J. Phys. Condens. Matter.* 19, 256201, **2007**.

[7] J. Perdew, Y. Wang, *Phys. Rev. B.* 45, 13244, **1992**.

[8] G. Kresse, J. Furthmüller, *Comput. Mat. Sci.* 6, 15, **1996**.

[9] G. Kresse, J. Furthmüller, *Phys. Rev. B.* 54, 11169, **1996**.

[10] E. Giamello, M. Volante, B. Fubini, F. Geobaldo, C. Morterra, *Mat. Chem. & Phys*. 29, 379, **1991**.

[11] A. Martínez-Arias, M. Fernández-García, C. Belver, J. Conesa, J. Soria, Catal. Lett. 65, 197, **2006**.

[12] R. Cook, F. Delucia, P. Helminger, *J. Mol. Spect.* 53, 62, **1974**.

[13] N. Greenwood, A. Earnshaw, *Chemistry of the Elements*. **1997**.

[14] J. Zhu, M. Mujeebur Rahuman, J.van Ommen, L. Lefferts, *Appl. Catal. A.* 259, 95, **2004**.

Chapter 7. Methane Reforming

This chapter explores the mechanisms by which methane can be activated and oxidised over YSZ materials. The calculations presented in this chapter primarily employ GGA-DFT electronic structure methods implemented in the VASP software package. The first, and likely rate limiting, step in the oxidation process is the first dehydrogenation from the highly stable methane molecule. The ways in which this can be catalysed by YSZ materials are explored in detail. Some subsequent reactions and product release mechanisms are also explored. The implications for catalysis over YSZ materials are discussed.

7.1 Methane Activation

Methane is a highly symmetrical and stable molecule, with the first C-H bond dissociation energy being 4.5eV[1]. Activating methane is thus a somewhat difficult process, requiring a combination of high temperatures and effective catalysts. This section deals with the activation of methane over YSZ materials and activated surface adsorbate species. Unless specifically stated otherwise, all models in this chapter use the 111 terrace YSZ vacuum slab model as described in chapters 3 and 6. Since these systems may involve electron transfer and radical species, unless otherwise stated all systems are modelled using spin polarised GGA-DFT with full electronic relaxation and geometry optimisation performed using a quasi-newton method as implemented in the VASP software package[2-4]. The PW91 functional and PAW pseudopotentials[5] supplied with the software package were used in all GGA-DFT calculations.

7.1.1 Methane Over Bare Zirconia Materials

The surfaces of zirconia and YSZ materials described in previous chapters present oxygen anions and cationic zirconium and yttrium. The potential for these sites to catalyse the breakdown of methane has been explored by constructing DFT model systems in which methane is placed close to various surface sites. All calculations in this section were carried out using DFT with the PW91 exchange-correlation functional and PAW pseudopotentials as implemented in the VASP software package.

The only interaction found with the pure zirconia (111) oxygen terminated surface is a weak physisorption. The structure after energy minimisation is visualised below in figure 7.1.1.1.

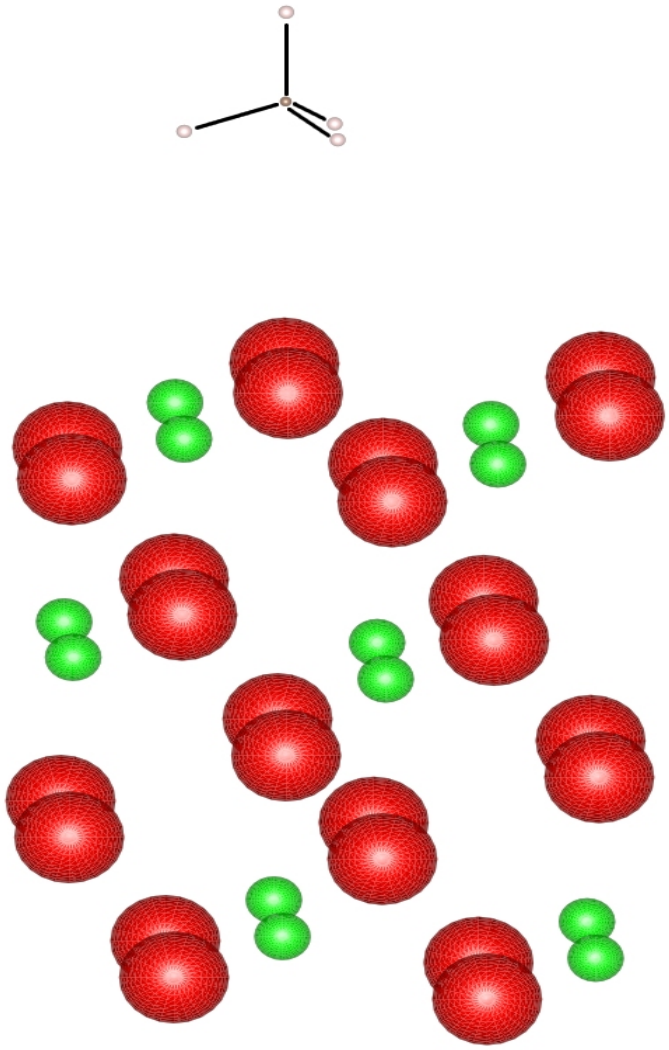

GGA-DFT model of methane physisorption over ZrO_2. Red is oxygen, green zirconium, brown carbon and light grey hydrogen.

(Fig. 7.1.1.1)

The methane molecule remains very close to its geometry in the vacuum, with bond lengths very close to 1.09Å and angles of 109.5º. It can be seen that the molecule adsorbs as a tripod with hydrogen atoms close to surface oxygen. The $O_{(surface)}$ - $H_{(methane)}$ distance for all three surface facing hydrogen atoms is nearly identical at approximately 3Å.

The physisorption occurs from the gas phase without any detectable activation barrier and is very slightly thermodynamically favourable (<0.05eV) relative to the centre of the vacuum gap. The extremely low energy change and relatively large equilibrium distance suggests that methane does not have a strong physical affinity for the ZrO_2 surface and any attraction is unlikely to be relevant under catalytic reaction conditions.

It should be noted that the DFT model used does not provide any means of representing dispersion forces which play a very significant role in many physisorption processes. As a result the energy predicted here is likely to be a significant underestimate of the real physisorption energy. It is possible to use dispersion corrected DFT techniques, for example the schemes devised by Grimme et al[6], to achieve more realistic representations of physisorption. Since the focus here is on high temperature catalysis, accurate determination of weak physisorption energies is not in the scope of this work. Physisorption energies will not be sufficiently large to be significant under reaction conditions.

On the model YSZ surface methane is also found to physisorb in a different configuration from on pure zirconia, with the methane somewhat tilted from the even tripodal configuration in Fig. 7.1.1.1. The interaction is again extremely weak and no reactivity is found over oxygen, yttrium, zirconium or vacancy sites with initial separations of as close as 1Å.

7.1.2 Activation by Surface Oxygen Species

As reported in chapter 6, the YSZ surface is able to stabilise superoxide species from molecular oxygen over oxygen vacancy sites in a slightly exothermic adsorption process. The YSZ surface containing a superoxide species can be seen as being activated. The surface containing the superoxide like entity was probed by positioning methane over the superoxide, a neighbouring oxygen and a surface zirconium site. The system was then geometrically optimised using a quasi-Newton optimisation method and GGA-DFT. It was found that the surface lattice oxygen neighbouring a vacancy which hosts a superoxide entity will abstract one hydrogen from methane, resulting in a surface OH group and a CH_3 species. This methane dissociation is slightly exothermic, the products being more stable than the reactants by 0.22eV. The optimised structure for this system is visualised below in figure 7.1.2.1.

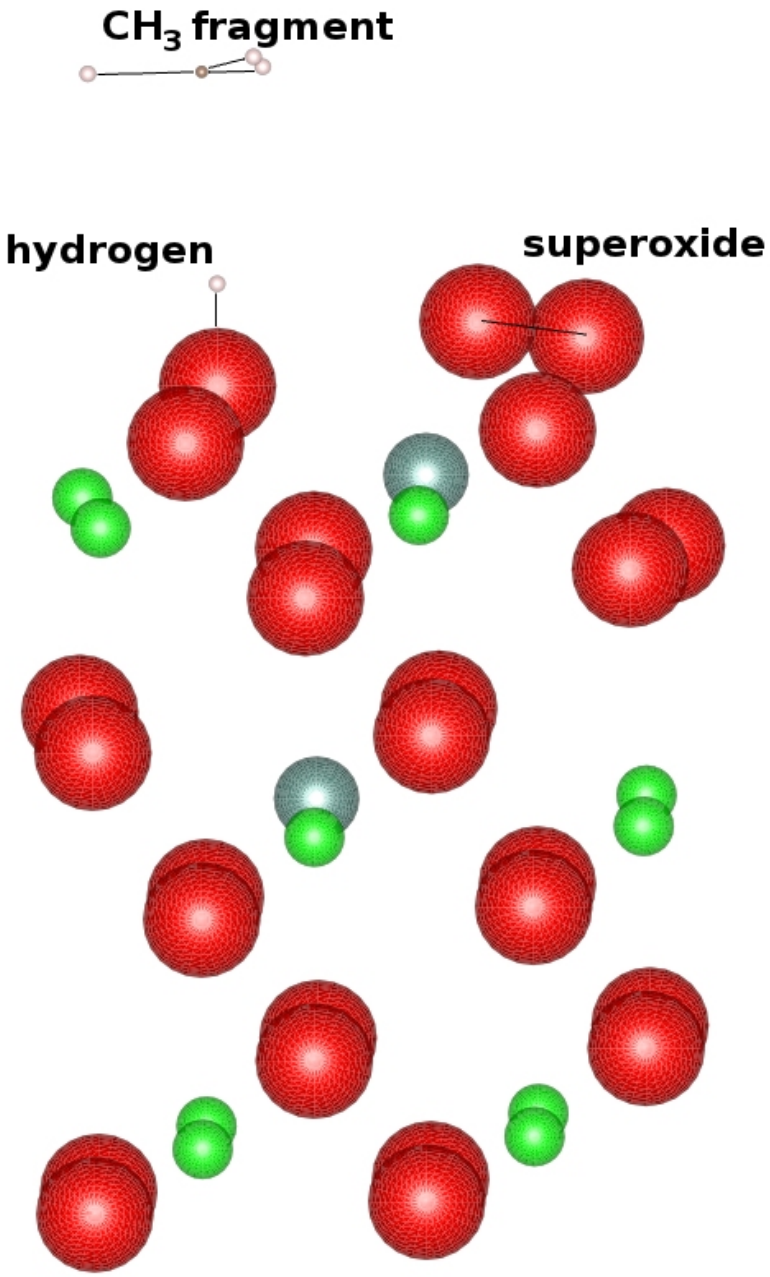

GGA-DFT model of products of methane dissociation over O_2/YSZ. Red is oxygen, green zirconium, blue yttrium, brown carbon and light grey hydrogen.
(Fig. 7.1.2.1)

The CH_3 entity adopts the triangular planar geometry typical of a methyl radical, with C - H bond lengths of 1.09Å and H - C - H angles of 120.0º. The newly created O - H bond has a length of 0.99Å. The location of the CH_3 entity at the local energy minimum is directly above the newly created surface OH group at a distance

of 2.1Å. The triangular planar geometry is characteristic of a methyl radical, indicating that the C-H bond is broken by homolytic cleavage to leave a single unpaired electron on the CH_3 fragment and transferring the proton as neutral atomic hydrogen. Visualising the unpaired electron density can be helpful in confirming the nature of the surface entities present, radical species would be expected to show significant unpaired spin density in characteristic patterns. Such a visualisation is provided in figure 7.1.2.2 below.

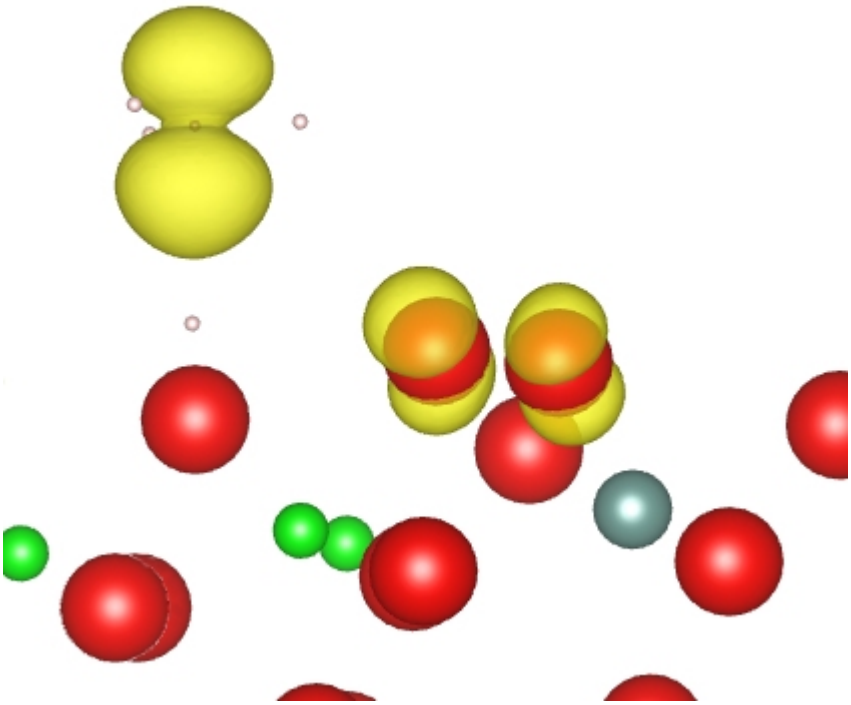

Enlargement of methane dissociation products on O_2/YSZ showing unpaired electron density isosurface (yellow) from GGA-DFT. Red is oxygen, green zirconium, blue yttrium, brown carbon and light grey hydrogen.

(Fig. 7.1.2.2)

As can be seen from the yellow regions (spin density isosurface) in figure 7.1.2.2 (above) there is significant unpaired electron density present on the CH_3 fragment, further confirming its identification as a methyl radical. The two significant lobes of unpaired density occupy regions above and below the plane of the triangular molecule, occupying a carbon 2p orbital. It is also apparent that the superoxide entity still has significant unpaired electron density, in fact the size of the lobes encompassed by the isosurface drawn at the same level has slightly increased

and the O – O bond has lengthened by 0.05Å to 1.36Å indicating that it has gained a small amount of electron density.

The electronic structure can be further understood by performing a Bader analysis, this was carried out for the methane on the superoxide/YSZ system, the results of which are tabulated below in table 7.1.2.1.

Entity (reactant / product)	**Charge (Reactants)**	**Charge (Product)**
O / OH	-1.68	-0.89
CH_4 / CH_3	0.00	0.04
O_2 / O_2	-0.57	-0.95

Bader charges on entities in the methane on O_2/YSZ system before and after methane dissociation.

(Tab. 7.1.2.1)

From the Bader analysis it is possible to deduce or confirm much about the electronic movements in the reaction which has occurred. Both the initial methane molecule and the resulting CH_3 fragment are approximately neutral, suggesting that the abstracted proton had been accompanied by one electron. The H_3C – H bond undergoes homolytic cleavage, one electron from the bond moving with the proton, the other remaining part of the CH_3 entity. The surface OH group has a charge of slightly less than -1, equivalent to the HO^- hydroxide anion. Breaking the charge distribution down further, the oxygen has a charge of -1.88 while the hydrogen is approximately +1 (a proton). Since the abstracted hydrogen is neutral and the surface oxygen initially has a charge of -1.68, electron density equivalent to approximately 1 election has to be accounted for. The superoxide species has accepted part of the density in to the anti-bonding orbital, its charge changing from from -0.57 to -0.95 and the remaining density, equivalent to approximately half an electron has been redistributed between the surface layer anions.

In order gain further knowledge of the mechanism of the methane dissociation reaction it is necessary to examine configurations intermediate to the reactants and products. Modelling of intermediates will also allow a reaction energy profile and activation energy to be estimated. Achieving an estimate of activation energy is highly desirable since it indicates whether a thermodynamically favourable

state is likely to be kinetically accessible under reaction conditions. A very large activation barrier may indicate that there is no accessible mechanism operating between the two states, potentially ruling a transformation out of a reaction scheme regardless of the relative stabilities of the two endpoints. In order to achieve an approximation of the intermediate configurations a set of intermediate input coordinates were generated. The set of initial configurations was generated by fixing the abstracted hydrogen at a set of regularly spaced points along a linear path between the reactant location and the product location. The remainder of the system was allowed to relax to the local energy minimum geometry at each point. A further set of configurations was then calculated between the highest two points in order to achieve a denser sampling of the critical region. The resulting energies are plotted below in figure 7.1.2.3.

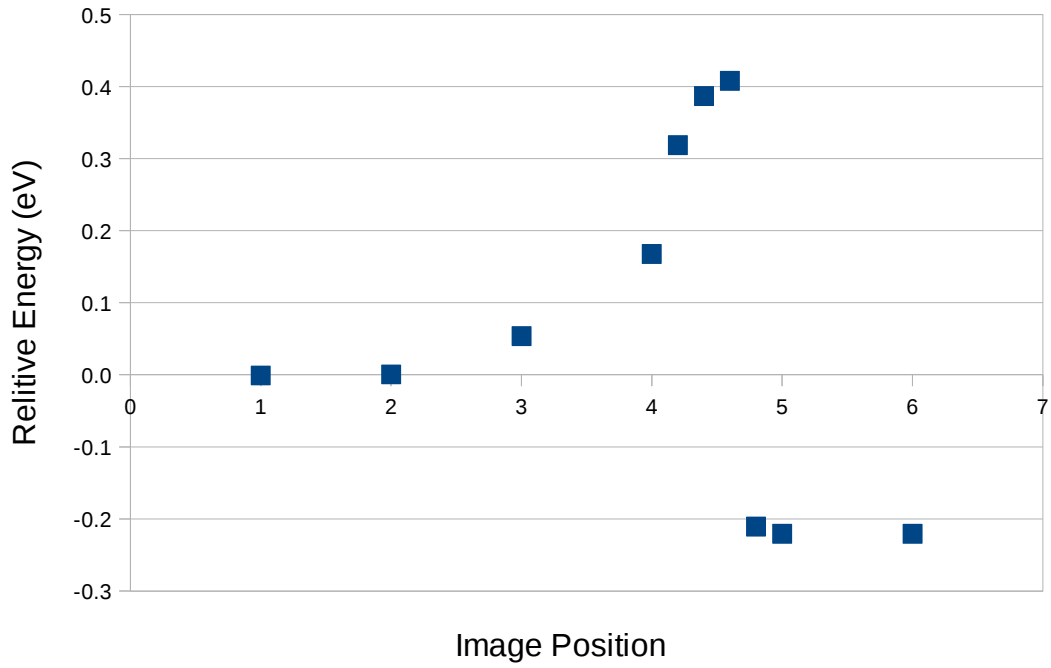

Constrained minimisation energy profile for methane dissociation over O_2/YSZ. (Fig. 7.1.2.3)

The above graph (fig. 7.1.2.3) shows a distinct activation barrier of approximately 0.41eV (0.63eV reverse). The energy maximum occurs between

images 4 and 5 of the initial series, image 4.6 of the more densely spaced second series. The structure at this separation may be considered a reasonable approximation to the transition state. The images represent evenly spaced initial O – H separations between the optimised reactant and product structures. It may be more meaningful to plot the energy as a function of final O – H or C – H separation after the constrained optimisation, the plotted point furthest to the right on both graphs contains two superimposed data points of almost identical values as the product structure.

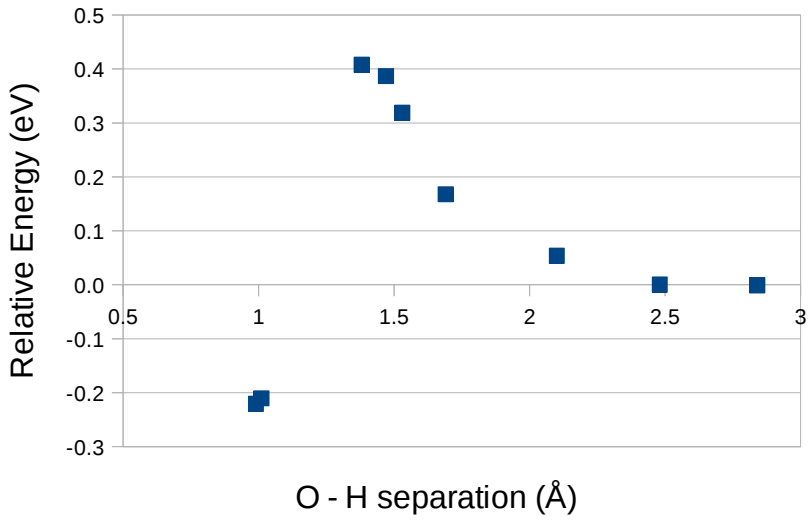

Energy as a function of O – H separation.

(Fig. 7.1.2.4)

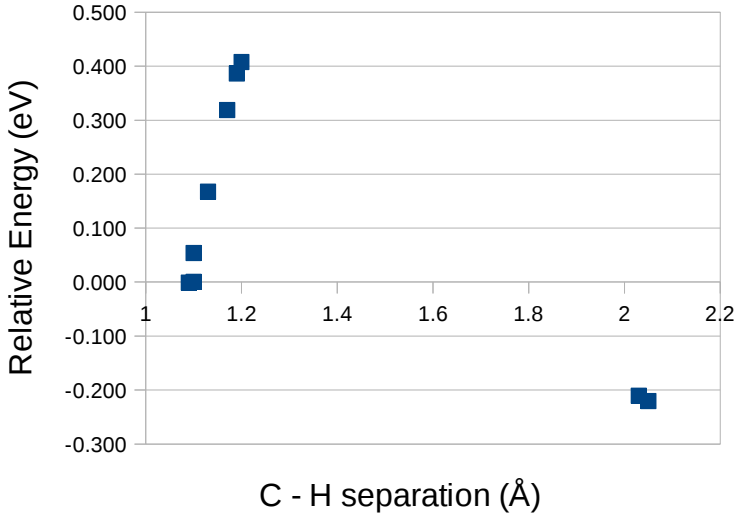

Energy as a function of H_3C – H separation.

(Fig. 7.1.2.5)

As can be seen in figure 7.1.2.4 the shift in energy is very sudden with respect to hydrogen position. Figure 7.1.2.5 shows a sharp discontinuity and wide separation in the relationship between energy and H_3C – H distance. The hydrogen position is externally fixed and the position of the oxygen is fairly tightly constrained by the lattice in which it is embedded, whilst the CH_3 fragment is free to move once its bond to the abstracted hydrogen is broken. The breaking of the C – H bond thus occurs suddenly, with a clear relationship between the energy and bond length as it extends. The longest C – H bond which is more stable than the broken form is approximately 1.2Å, with the CH_3 fragment moving away immediately once the bond is broken. The approximate transition state is visualised below in figure 7.1.2.6.

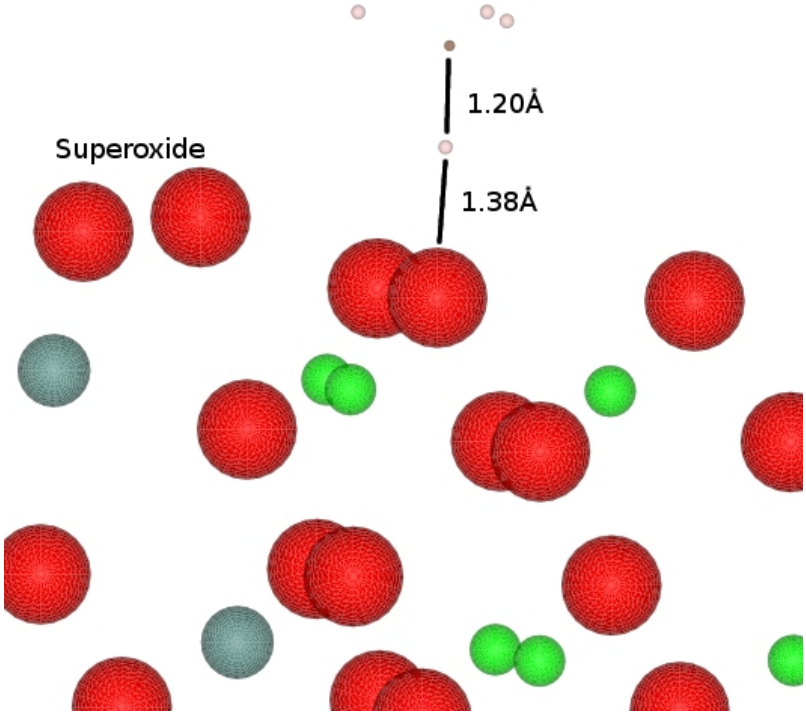

Approximate GGA-DFT transition state of methane dissociation over O_2/YSZ. Red is oxygen, green zirconium, blue yttrium, brown carbon and light grey hydrogen. (Fig. 7.1.2.6)

The transition state depicted in figure 7.1.2.6 shows hydrogen somewhat shared between the CH_3 group and the surface oxygen. The transferring hydrogen is 1.38Å from the surface oxygen and 1.2Å from the central carbon of the methane fragment. The geometry of the methane fragment is relatively unchanged, the H – C – H angles which include the transferring hydrogen are 108.0º while those between the hydrogen atoms of the CH_3 fragment are 110.7º. When compared to methane (109.5º) and the methyl radical (120º) it can be seen that the geometry is much closer to methane. This is consistent with the increase in energy as the C – H bond lengthens and the sudden change to a product like configuration and energy level as the bond is broken, forming the planar methyl radical.

In order to better understand the electronic structure of the approximate transition state, the unpaired electron density may be visualised as well as a Bader

charge analysis performed. The unpaired electron density is rendered as an isosurface (yellow) in the model below (fig. 7.1.2.7). The Bader charges for selected entities are labelled on the figure.

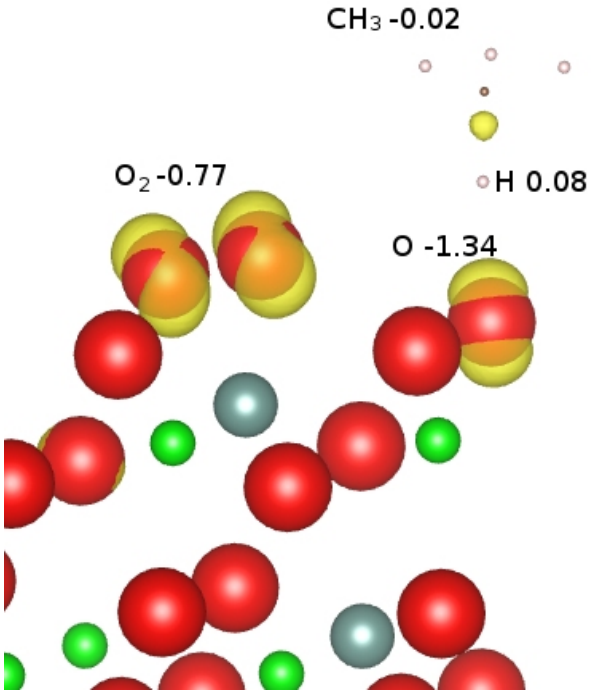

Enlargement of GGA-DFT unpaired electron density isosurface (yellow) on the transition state structure. Red is oxygen, green zirconium, blue yttrium, brown carbon and light grey hydrogen.

(Fig. 7.1.2.7)

The electronic structure of the approximate transition state shows the H_3C – H bond beginning to split. Interestingly, the unpaired electron density and Bader charges tell of competing bond breaking processes. The Bader charges indicate a slight polarisation of the bond, with electron density moving away from the hydrogen and towards the CH_3 fragment. The weak polarisation seen is probably induced by the proximity of the electron cloud of the surface oxygen and the nearest end of the methane molecule mutually repelling. Further evidence of the mutual repulsion of electrons at this distance is seen in the change of the surface oxygen, becoming more positive as density equivalent to 0.34 of an electron is moved to other surface ions. If the polarisation were to continue then the bond would split heterolytically, with hydrogen being transferred to the surface as a proton and the CH_3 fragment assuming

a negative charge. However, the isosurface indicates that homolytic cleavage is beginning. It can be seen that there is unpaired electron density in the region of the cleaving C - H bond and on the accepting surface oxygen. The neighbouring superoxide like species can be seen from the Bader charges to be accepting a large portion of the electron density lost form the reacting surface oxygen ion, becoming a full rather than partial superoxide in the final product configuration.

Analysis of the charge data and unpaired electron density distribution of the reactants, transition structure and products allows for mechanisms to be proposed. On the basis of the DFT model the reaction mechanism in figure 7.1.2.8 has been constructed.

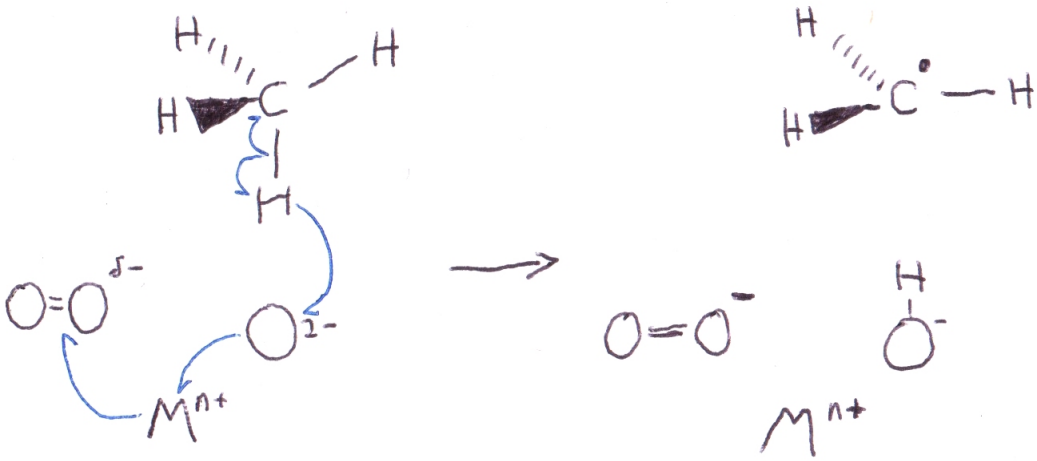

Simplified proposed mechanism of hydrogen abstraction.
(Fig. 7.1.2.8.)

While the diagram above somewhat oversimplifies the movement of electrons within the YSZ material it is consistent with the findings of the DFT models. The H_3C – H bond undergoes homolytic cleavage, transferring neutral hydrogen to the surface oxide ion. The additional electron density does not remain on the OH group, but is instead transferred, leaving the hydroxyl group with an overall -1 charge. The majority of the electron density is accepted by the superoxide like O_2 entity, which then has a full -1 charge and correspondingly a slightly greater bond length. The remainder of the electron density in the DFT model is shared among the other surface ions. In this way the superoxide like species acts as an electron acceptor for neighbouring surface oxygen ions, thereby activating the surface towards methane.

Although the modelling work reported in this section indicates that a YSZ surface activated with superoxide like adsorbed oxygen will readily catalyse hydrogen abstraction from methane with a relatively low activation barrier, it should be noted that in the majority of real catalytic systems this mechanism is unlikely to form the primary means of methane activation. In an ATR the large combustion zone and gas mix means that very little molecular oxygen is likely to survive to reach the catalyst surface. It is however a plausible mechanism for the initial methane activation in the model system described by Zhu et al[7-8] in which the two bed

catalyst set-up and lack of a large combustion void means that molecular oxygen is far more likely to be present on the YSZ surface. In industrial autothermal reforming, the catalyst material is composed of metallic particles (nickel or platinum group metals) on a YSZ support. In this case, it is likely that initial methane activation occurs with the aid of the metallic particles, with YSZ conducting oxygen to the metal-support interface and catalysing many subsequent reactions as well as reforming reactions of combustion fragments.

7.1.3 Hybrid DFT Model of CH_4 Activation

The model presented in the previous section (7.1.2) has been replicated, applying the HSE06 hybrid functional DFT electronic structure method (see chapter 3) in place of the PW91-GGA-DFT method. The HSE06 model was employed with 25% HF exchange within a range parameter of 2.07Å and implemented by the VASP software package. It was necessary to use a reduced plane-wave cut-off energy (450eV) and relaxed structural convergence criteria (0.025eV) in order to somewhat mitigate the much higher computational complexity of hybrid functional DFT. It is therefore reasonable to expect a modest reduction in precision for these calculations over the GGA-DFT model, but good qualitative and useful quantitative information may still be extracted. The model was built by optimising bulk cubic zirconia, then cleaving and optimising the surface, followed by doping and re-optimisation to yield a YSZ surface model. Molecular oxygen was then added above the surface oxygen vacancy site and a further optimisation carried out to yield the model described in section 6.3.1. That model is employed here to further investigate the methane hydrogen abstraction reaction seen in the GGA-DFT model (section 7.1.2).

The initial structure has a very similar geometry to that predicted by the GGA-DFT model. The main difference is that the O_2 entity is significantly less reduced, showing a shorter bond length and much reduced Bader charge. The differences in the oxygen state is discussed in section 6.3.1. The optimised initial structure, with methane distant from the YSZ surface, predicts C – H bond lengths of 1.09Å, equivalent to both the GGA-DFT model and reference data. The optimised product structure, with the hydrogen transferred to the surface oxygen, is shown below (fig. 7.1.3.1).

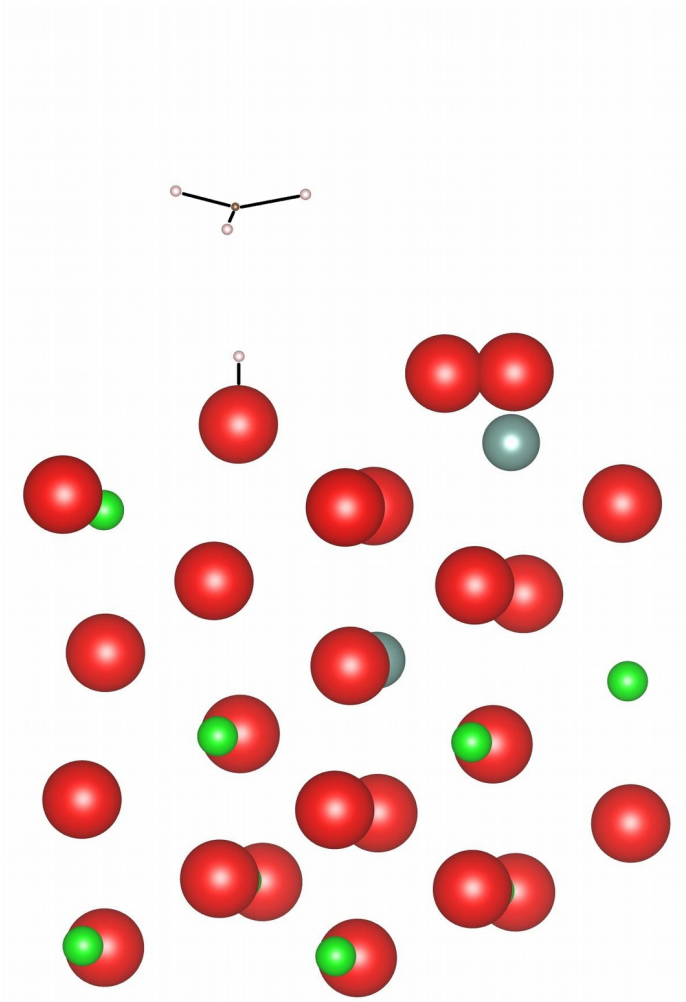

HSE06 model of products of methane activation over O_2/YSZ. Red is oxygen, green zirconium, blue-grey yttrium, light brown hydrogen and dark brown carbon. (Fig. 7.1.3.1)

The optimised product structure (fig. 7.1.3.1) is very similar to that predicted by the GGA-DFT model (fig. 7.1.2.2). The methyl radical is still approximately triangular planar, with H - C – H bond angles of 120º. The O – H bond length is 1.03Å.

The electronic structure can be described with the help of a Bader charge analysis and by visualising the unpaired electron density distribution as below in figure 7.1.3.2.

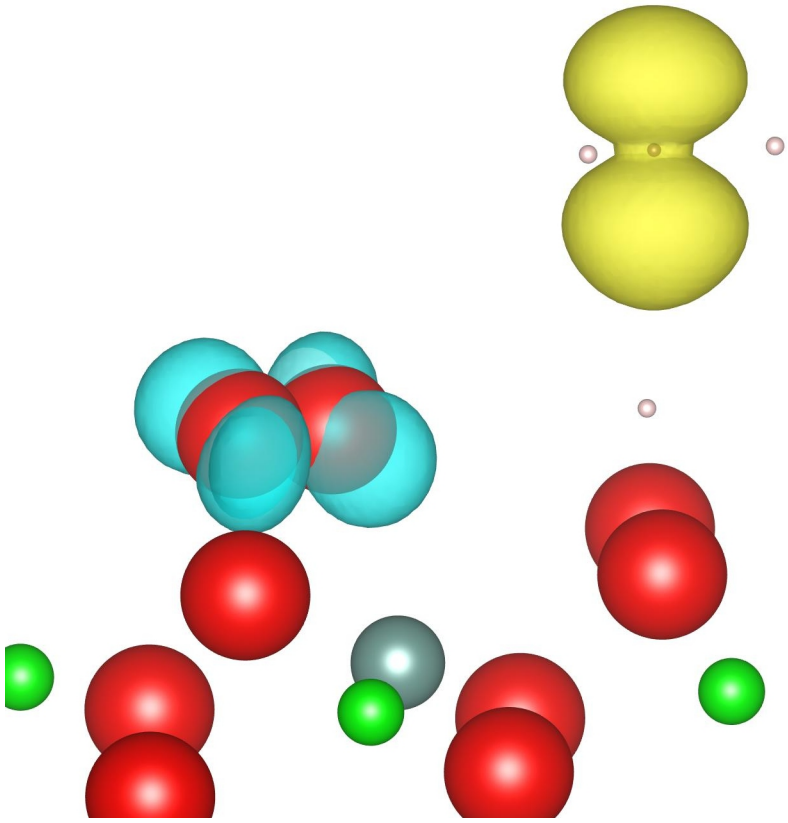

Unpaired spin density as predicted by the HSE06-DFT model of methane activation. Red is oxygen, green zirconium, blue-grey yttrium, light brown hydrogen and dark brown carbon. The yellow and blue surfaces show unpaired electron density.
(Fig. 7.1.3.2)

As can be seen in figure 7.1.3.2 above, the HSE06 hybrid DFT model shows a large region of unpaired electron density on the CH_3 entity, centred on the carbon with symmetrical lobes above and below, perpendicular to the plane of the molecule. The spin density on the CH_3 entity is consistent with the GGA-DFT model (fig. 7.1.2.2) and characteristic of a methyl radical. The O_2 entity has a significant region

of unpaired electron density centred on each oxygen atom. Again, the regions are consistent with the GGA-DFT model, although slightly smaller when plotted at the same level. A Bader charge distribution analysis can be used to quantify how much electron density has been transferred to the O_2 species as well as provide information about electronic states of other entities present. The table below (tab. 7.1.3.1) provides partial charge information based on the Bader partitioning method for selected entities in the initial and final systems, the equivalent for the GGA-DFT model is provided in Tab. 7.1.2.1.

Entity	Charge (initial)	Charge (product)	Charge (product -initial)
O_2	-0.14	-0.74	-0.60
CH_x	±0.00	+0.03	+0.03
$O_{(surface)}$	-1.68	-1.94	-0.26
$H_{(transferred)}$	+0.02	+1.00	+0.98

Bader charges of entities in the reactant and product systems as predicted by HSE06 hybrid functional DFT.

(Tab. 7.1.3.1)

As can be seen from the Bader charges and unpaired spin density surfaces, the distribution of electrons in reactant and product systems fits the same qualitative discipline of electron movement in the reaction as those from the GGA DFT model. The neutral methane molecule looses a neutral hydrogen by homolytic bond cleavage, creating a neutral methyl radical. The hydrogen atom transfers its electron density almost entirely to the surface as it is transferred to the surface oxygen ion. The oxygen ion gains a small amount of electron density, but the majority of it is transferred on to the O_2 species located over the neighbouring YSZ surface oxygen vacancy. In this way the HSE06 hybrid DFT model fully supports the mechanism proposed in section 7.1.2, see figure 7.1.2.8 for a summary illustration.

The Bader charges do show some important differences between the HSE06 hybrid functional DFT and the GGA DFT models. The HSE06 model shows a greater change in charges than the GGA DFT model. In particular, more electron density is gained by the oxygen ion receiving the hydrogen and by the superoxide like O_2 entity. Less electron density is distributed across the uninvolved ions in the system.

Although it is hard to rigorously demonstrate, it is reasonable to suggest that the HSE06 hybrid DFT model is the more accurate of the two representations. Plane-wave GGA DFT has a well known tendency to excessively de-localise electron density due to an unphysical self-interaction effect (see chapter 3). A hypothesis of unrealistically excessive de-localisation would fit with the observation that the GGA DFT model distributes a greater amount of electron density fairly evenly throughout the surface model, rather than concentrating it on the oxygen anion to which the hydrogen is transferred and on the superoxide like O_2 species.

The HSE06-DFT model predicts the reaction to be slightly more thermodynamically favourable than the GGA-DFT model. The overall reaction energy in the HSE06-DFT model is -0.29eV, compared to -0.22eV in the GGA-DFT model. Due to the computational complexity of hybrid functional DFT, it was not possible to undertake an extensive or even limited transition state search. However, one intermediate structure was calculated. Based on the optimised geometry when compared to the series of GGA-DFT calculations, it would not appear that the structure calculated was a good candidate for an approximate transition state. Therefore, it would not be appropriate to attempt any quantitative analysis of the activation energy or any features of the transition state based on this hybrid functional DFT model.

It would however be reasonable to state that, based on the one intermediate calculation performed the hybrid functional DFT model would appear likely to predict a significantly higher activation barrier. At approximately the same C – H bond length after optimisation the change in energy is very roughly 40% greater based on the hybrid functional than GGA DFT for the sample of one intermediate structure calculated. A higher activation barrier would seem intuitively likely, based on the tendency of the hybrid functional DFT method to predict tighter localisation of electron density as compared to GGA DFT. If GGA DFT has a tendency to de-localise electrons, it may potentially allow unfavorable electronic states to be somewhat artificially stabilised by spreading the electrons more widely.

7.2 Subsequent Reactions

The breaking of the first C – H bond and formation of a methyl radical can be seen as an initial activation of methane, opening it up to further reactivity. It is also the case that in YSZ supported metallic catalyst systems that methyl radicals and other fragments will reach the YSZ surface where further reactivity will occur. The further reactions of the methyl radical are explored using a GGA-DFT model in this section.

7.2.1 Formaldehyde Formation

The methyl radical is found by GGA-DFT modelling to react with surface superoxide to form a formaldehyde like H_2CO entity. As discussed in chapter 2, Zhu et al[7] propose formaldehyde as a potential intermediate in methane reforming over YSZ materials.

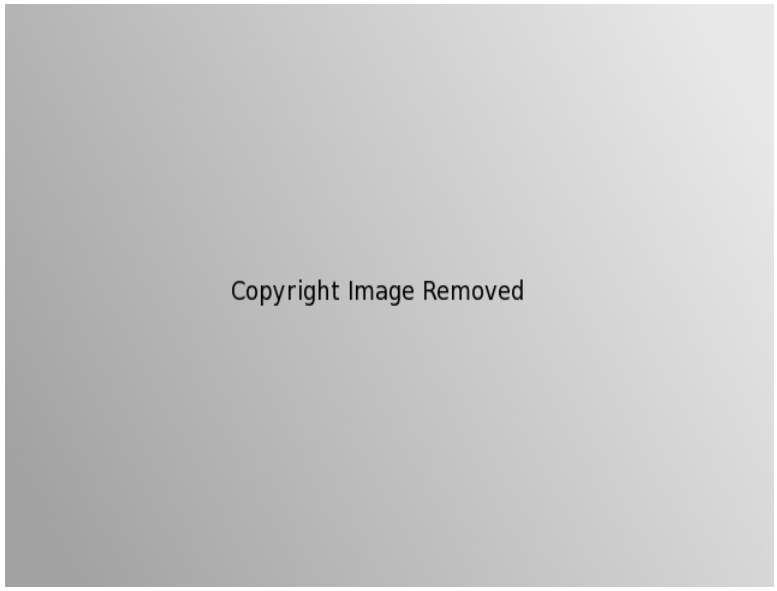

Reaction scheme proposed by Zhu et al[7].

(Fig. 7.2.1.1)

In the scheme above (Fig. 7.2.1.1) surface formaldehyde is proposed as an intermediate through which all methane will pass before further stages lead either to synthesis gas components or combustion products. While the evidence of formaldehyde as an intermediate is not conclusive, there is sufficient reason to

examine it further. The result of the model of formaldehyde formation from a methyl radical and surface adsorbed O_2 species is visualised in figure 7.2.1.2 below.

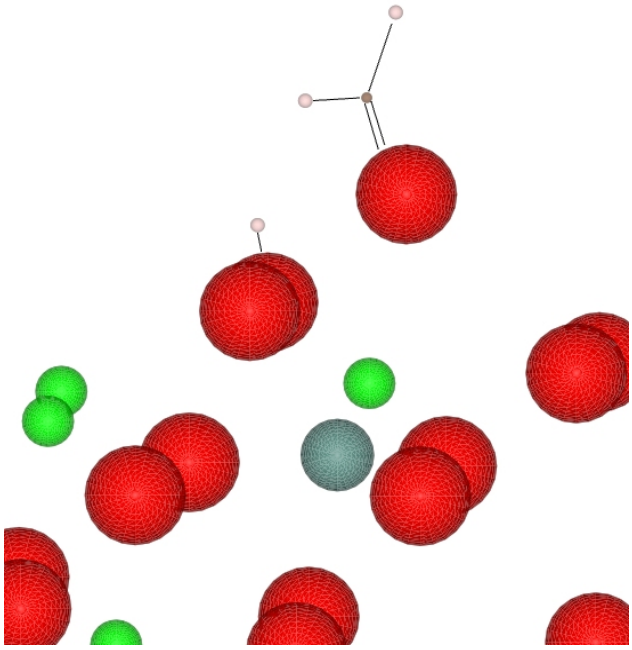

GGA-DFT model of H_2CO resulting from interaction of a methyl radical with superoxide. Oxygen is red, zirconium green, yttrium blue-grey, carbon brown and light grey hydrogen.

(Fig. 7.2.1.2)

The formaldehyde entity is formed of one oxygen from the superoxide, the carbon and two of the hydrogen atoms from the methyl radical. The remaining hydrogen and oxygen form a hydroxide group which is positioned filling the YSZ surface oxygen vacancy site. The overall reaction is exothermic, the energy change being -1.13ev.

The H_2CO entity has bond lengths and angles very close to those of neutral formaldehyde. The angle between the two C-H bonds is 120.3º and they are of 1.11Å in length; the angle between the C-H and C-O bonds is also approximately 120º and the C-O double bond is 1.23Å long. A Bader analysis confirms that the formaldehyde molecule is very close to neutral (-0.03), while the newly created OH entity has a charge close to that of a hydroxide anion (-0.81).

In order to estimate the activation energy and identify an approximation of the transition state a relatively crude (5 point) series of constrained minimisations was performed. The central carbon of the methyl radical was fixed in an evenly spaced series of positions with an initial separation between the methyl radical and the superoxide of 2.2Å to 1.2Å. Due to the relatively sparse nature of this series the activation energy and transition state geometry must be considered as only indicative. The approximate activation energy is found to be 0.6eV. The structure at this point may be regarded as an approximation to the transition state. A visualisation of the transition structure is given below in figure 7.2.1.3 with an electron density isosurface (yellow) to give some guidance as to bonding.

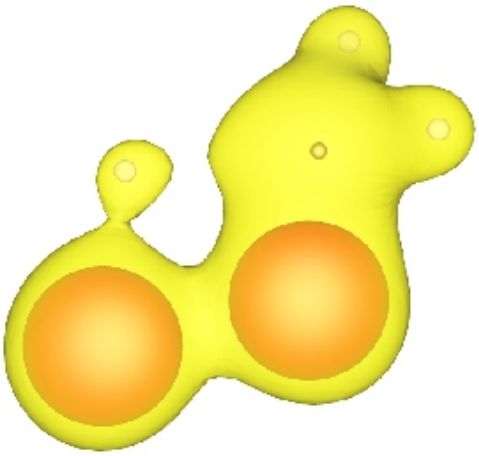

Magnification of the approximate transition structure showing an electron density isosurface (yellow). The YSZ lattice surface has been removed for clarity. Oxygen is red, carbon brown and hydrogen light grey.

(Fig. 7.2.1.3)

The approximate transition structure shows the C – H bond breaking while C – O and H – O bonds form. The O – O bond has yet to be broken. The formation of formaldehyde over YSZ is the first step in the methane reforming reaction scheme proposed by Zhu et al in their model system[7] (step 1 in figure 7.2.1.1). However, modelling investigations reported in this chapter suggest that the transformation from methane to formaldehyde does not occur in a single concerted step but rather proceeds via the methyl radical (see 7.1). The formaldehyde molecule contains the correct ratio of atomic constituents to produce the desired synthesis gas components of carbon monoxide and molecular hydrogen. In the transformation from methane it

has lost two hydrogen atoms as surface OH species. A graphical summary of the transformation is provided in figure 7.2.1.4 below.

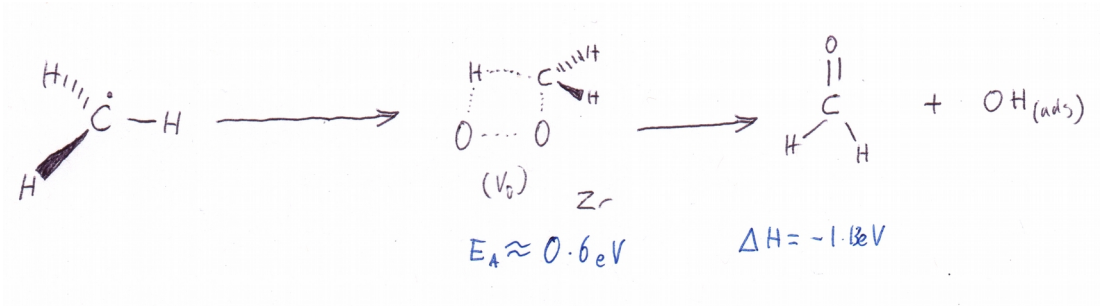

Graphical summary of the transformation, with energies from the DFT model. (Fig. 7.2.1.4)

Formaldehyde is, relative to methane, a fairly reactive molecule which should readily be able to undergo further oxidation or reactions with surface and gas phase species. Formaldehyde contains the correct element ratio to be transformed into one molecule each of hydrogen and carbon monoxide. The reaction scheme of Zhu et al (figure 7.2.1.1) suggests that formaldehyde does indeed decompose to give syngas components, hydrogen and carbon monoxide (transformation 5). The transformation is thermodynamically favourable, exothermic by very approximately -0.5ev based on bond strengths. However, there is likely to be a significant activation barrier, since the two C – H bonds must be broken either sequentially or simultaneously. It is possible that YSZ surface sites may act to reduce the barrier. However, calculations carried out over the bare YSZ terrace surface failed to locate any site where dissociation was energetically favourable. It is possible that the 9 point grid search used missed an active site, that significant activation (e.g. stretching the C-H bonds) is required or that adsorbed surface species promote the activity.

7.3 Products

The interactions of syngas components (hydrogen and carbon monoxide) with the YSZ surface is of interest in understanding product release and potentially additional reactivity leading to by-products or altering the product ratio. This section explores the interaction of methane reforming products with the YSZ surface.

7.3.1 Carbon Monoxide

Carbon monoxide is one of the two primary products of methane reforming and a major component of syngas, assuming the WGS reaction is not employed to liberate more hydrogen from water, driven by the conversion of carbon monoxide to carbon dioxide. For this reason the interactions between the YSZ surface and carbon monoxide is of some interest.

The interactions of carbon monoxide with the YSZ 111 terrace surface have been investigated by applying PW91 GGA DFT modelling to configurations of carbon monoxide in proximity to various surface sites in both vertical orientations and aligned parallel to the plane of the surface. Sites probed include surface oxygen ions, the oxygen vacancy site and above zirconium ions. The results of these calculations indicate that carbon monoxide is fairly inert towards the bare YSZ surface. All interactions found would best be characterised as weak physisorption, the strongest of which (-0.07eV) was found over the oxygen vacancy site with the carbon monoxide adsorbing with the oxygen molecule closest to the surface. The carbon monoxide molecule shows only very slight changes, the C – O bond lengthening by 0.02Å. Both the energy, which it should be noted does not include any dispersion interactions, and the change in C – O bond length are extremely small and should not be considered significant in the context of the model system. The model indicates, at most, weak physical interaction with the surface. YSZ may still play a role in reactions of carbon monoxide, such as the WGS reaction, by immobilising and activating other reagents, such as water (see chapter 6).

7.3.2 Hydrogen

Hydrogen is one of the two primary components of syngas, generally the most significant component by volume and molar ratio. Several of the YSZ surface reactions explored previously in this chapter result in liberation of hydrogen atoms from gas phase molecules and their capture by surface oxygen to form surface O – H groups. The release of hydrogen from surface O – H groups and formation of gas phase molecular hydrogen (H_2) is therefore of interest. Likewise, with molecular hydrogen being present in significant quantities in the gas mixture flowing over the catalyst surface in ATR processes, the interactions of hydrogen with the YSZ surface are of interest. These two concerns are represented by the same processes operating in opposite directions and can be explored simultaneously using GGA-DFT.

The approach taken was to begin with gas phase hydrogen, both as the H_2 molecule and as isolated hydrogen atoms and probe YSZ surface sites. Sites probed include the surface oxygen ion, oxygen vacancy and zirconium ions. In order to test for adsorption the hydrogen molecule or atom was placed in the vacuum gap at a distance of 1Å above the target surface site and the system geometry optimised.

It was found that atomic hydrogen may be captured by surface oxygen ions and oxygen vacancy sites. The minimum energy structures of adsorbed atomic hydrogen over oxygen and oxygen vacancy sites are depicted in figure 7.3.2.1 and analysed below.

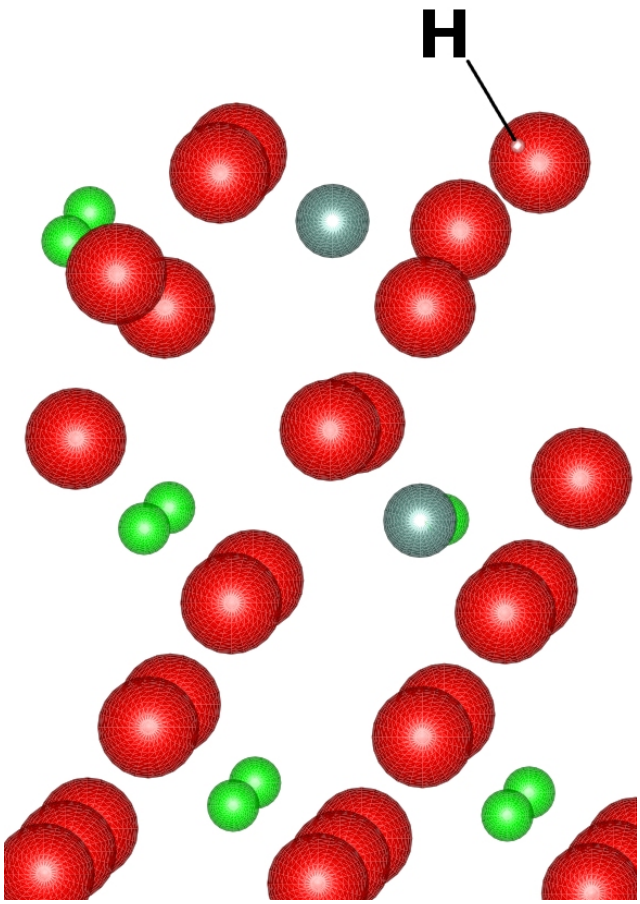

GGA-DFT model of hydrogen atom adsorbed over an oxygen vacancy site, Hydrogen is labelled for clarity. Oxygen is red, zirconium green, yttrium blue-grey and hydrogen light grey.

(Fig. 7.3.2.1)

Figure 7.3.2.1 shows a hydrogen atom adsorbed above an oxygen vacancy site. The interaction is favourable by 0.13eV relative to hydrogen in the gas phase. In order to better understand the interaction a Bader charge analysis was performed. The Bader charge on the hydrogen is -0.17, showing that it has gained a small amount of electron density from the vacancy region to become somewhat hydride-like. A crude 5 point constrained minimisation series showed no activation barrier from the gas phase, but a very flat energy profile with the stabilisation occurring as the hydrogen approaches the vacancy site.

A much stronger interaction (1.2eV) is found for atomic hydrogen with surface oxygen ions. Figure 7.3.2.2 below shows the position of the adsorbed hydrogen atom as predicted by the DFT model.

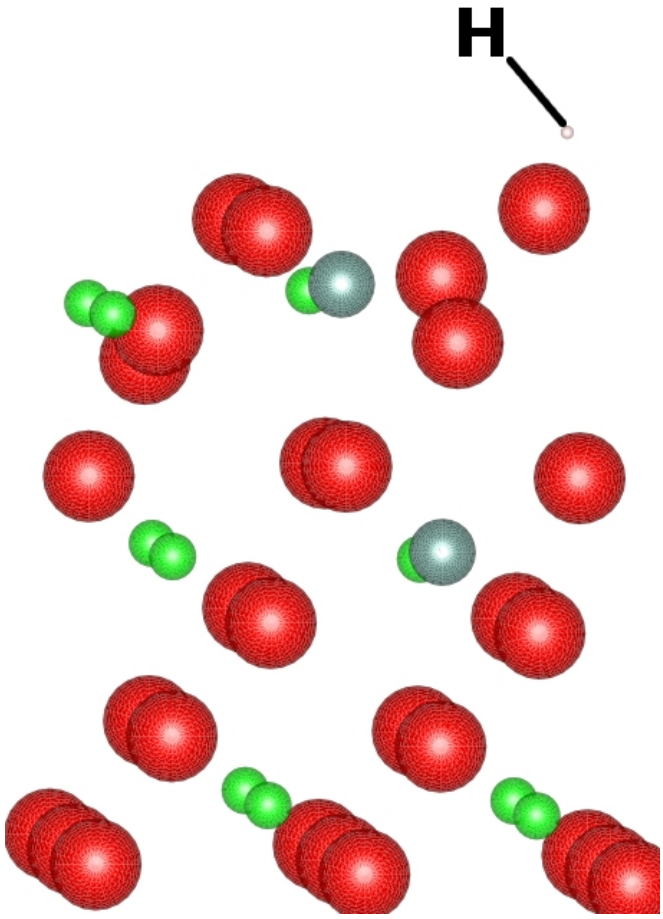

GGA-DFT model of atomic hydrogen adsorbed above a surface oxygen ion, hydrogen is labelled for clarity. Oxygen is red, zirconium green, yttrium blue-grey and hydrogen light grey.

(Fig. 7.3.2.2)

As can be seen in figure 7.3.2.2 above, the hydrogen atom interacts directly with one surface oxygen and is not directly above it but is slightly tilted from the vertical. The O – H distance is 0.97Å, not far from a water O-H bond length. A Bader analysis was performed on the electron density distribution of this system and showed that almost all of the electron density was transferred from the hydrogen atom, leaving it with a charge of +0.92, while the newly formed OH group has an

overall charge of -0.89. The OH group is analogous to a hydroxide anion ($^{-}$OH). An electron density isosurface plot (Fig. 7.3.2.3 below) shows that oxygen shares significant electron density with the hydrogen.

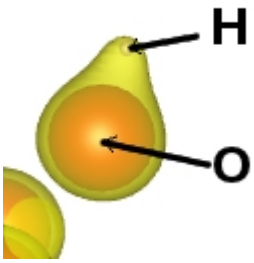

Plot of GGA-DFT electron density level around surface oxygen and adsorbed hydrogen. Yellow is the electron density isosurface, oxygen (red) and hydrogen (grey) are labelled.

(Fig. 7.3.2.3)

The large binding energy (-1.2eV), short O – H distance (0.97Å) and shared electron density all indicate a strong affinity of the surface oxygen for atomic hydrogen. The charge distribution between the hydrogen and oxygen atoms (+0.92 and -1.81) suggest that the affinity of surface oxygen anions for protons (H^{+}) would be at least as strong. A linear 5 point constrained minimisation series with initial O – H separations of 2.47 to 0.97Å indicates no distinct activation barrier for atomic hydrogen adsorption on surface oxygen.

Molecular hydrogen was found to show weaker adsorption interactions on the YSZ surface. Adsorption above the oxygen vacancy site it stabilised by 0.09eV relative to the gas phase and over surface oxygen the strongest interaction found has a strength of 0.1eV. It should be noted that neither of these energies include dispersion effects which are not represented in the DFT model. In both cases the H -H bond lengths are not significantly changed (<0.02Å) from gas phase H_2. A Bader analysis shows very slight electron transfer to hydrogen over the vacancy site and away from hydrogen over oxygen, but in both cases the change in charge is less than ±0.05. The combination of these factors suggests that molecular hydrogen does not have a high affinity for the YSZ bare surface with out significant activation barriers such as the cleavage of the H – H bond.

The understanding of interactions between hydrogen atoms and molecules with the surface can provide some insight in to hydrogen product release from YSZ materials. Reactions described in this chapter which release hydrogen generate surface OH groups. The release of molecular hydrogen from these OH sites is subject to a significant energy barrier. Release of a single hydrogen atom to vacuum from a surface OH group requires the input of approximately 1.2eV of energy, equivalent to 2.4eV for the pair required to make a hydrogen molecule. There is a strong driving force, the H – H bond strength is 4.48eV, meaning that the overall energy for release of two independent surface hydrogen atoms and their joining to produce molecular hydrogen is approximately -2.08eV (strongly exothermic). The energy barrier of 1.2eV is significant, however the catalytic system operates at very high temperatures (up to 1200ºC) and there may be mechanisms by which the barrier can be lowered. For example, it may be speculated that neighbouring O – H sites may experience reduced activation barriers when neighbouring hydrogen atoms are released, or that a surface hydrogen atom of an group can accept an additional hydrogen from an activated gas phase or surface species to release molecular hydrogen. It should be notes that such mechanisms were not explored as part of this work.

7.4 Discussion & Summary

Methane has a first C – H bond dissociation energy of approximately 4.5eV, is highly symmetrical and doesn't contain and functionality to easily provide a lower barrier to activation. There is therefore considerable interest in catalytic systems which allow for methane activation with a lower barrier. The DFT model presented predicts an exothermic (-0.22eV) activation route with a relatively low activation barrier (0.41eV) for hydrogen abstraction over YSZ in the presence of oxygen. As discussed in chapter 6, molecular oxygen will form a reduced superoxide like species over surface oxygen vacancies in an exothermic (-0.47eV) process. The partially reduced O_2 species occupies a site above the oxygen vacancy and promotes the activity of the surface towards methane. A surface oxygen anion in a neighbouring position to the reduced O_2 entity is able to abstract a hydrogen atom from methane. The process occurs by homolytic C – H bond cleavage, the hydrogen being

transferred to the surface oxygen ion as a neutral atom. The electron density is accepted by the surface O_2 species, reducing it to a fully superoxide like state (Bader charge -0.98). For a proposed reaction mechanism, see figure 7.1.2.8. The result is a surface hydroxide (HO^-) group and a neutral methyl radical ($^{\cdot}CH_3$).

The methyl radical, whether produced by O_2/YSZ catalysed hydrogen abstraction or originating on supported metallic particles, is a highly active species when compared to methane. It is likely that many further transformations become possible, including gas phase reactivity. A DFT model of the reaction with molecular oxygen adsorbed on YSZ has been constructed and is discussed in detail in section 7.2.1. The reaction occurs when the methyl radical approaches the superoxide like species with one C – H bond aligned parallel with the O – O bond. C – O and H – O bonds form as the C – H bond breaks. The O – O bond lengthens and eventually breaks to release the formaldehyde molecule. An OH surface group is created from the remaining hydrogen and oxygen and occupies the surface oxygen vacancy site. The overall reaction is strongly exothermic, with an energy change of -1.13eV. The activation barrier is estimated at approximately 0.6eV.

The effect of the two transformations discussed above is to oxidatively convert methane to formaldehyde with the creation of two surface OH groups from the liberated hydrogen. The combined transformation is closely equivalent to step 1 (fig. 7.2.1.1) of the sequence proposed by Zhu et al[7]. The only difference being that instead of H_2O the DFT modelling has produced two surface OH groups. Given that one of the OH groups incorporates oxygen from the gas phase and the other was originally part of the oxide material the numbers and types of atoms are equivalent; Two hydrogen atoms and a single oxygen atom are released in addition the formaldehyde molecule.

The proposed reaction scheme of Zhu et al[7] then shows conversion of formaldehyde, either directly to syngas components (transformation 5 on fig. 7.2.1.1), via gas phase (transformation 6) reactions to syngas (transformation 8) or combustion products (transformation 7) with the addition of oxygen. Another proposed path proceeds (transformation 2) via further oxidation to the formate anion before yielding either a mixture of syngas components and combination products (transformations 3 and 4) or purely combustion products (transformation 9) via

carbonate. The understanding of the possible mechanisms of theses steps could benefit from further modelling work.

The transformation from methane to formaldehyde via the methyl radical yields two atoms of hydrogen, which form OH groups on the YSZ surface, by combining with intrinsic surface oxygen anions or with half of an oxygen molecule adsorbed from the gas phase. Adsorbed hydrogen atoms are found to be tightly bound, with energies of approximately 1.2eV per hydrogen atom over surface oxygen ions. The release of hydrogen bound to surface oxygen to form molecular hydrogen is thermodynamically favoured (approx. -2.08eV per hydrogen molecule), but must overcome a significant energy barrier. It may be the case that mechanisms exist to lower this barrier and that binding becomes less strong as the surface oxygen sites begin to become saturated with hydrogen. Oxidising species from the gas phase will also act to remove surface hydrogen. The release of hydrogen from the surface is necessary to produce syngas. The other component of syngas, carbon monoxide, does not have a strong affinity for the bare YSZ surface, so its release is not an issue. However, carbon monoxide may interact with adsorbed surface species, for example in the WGS reaction or leading to unwanted complete oxidation to CO_2.

In order to summarise and illustrate the key catalytic reactivity leading from methane to syngas as explored in this chapter, a partial reaction scheme has been constructed (fig. 7.4.1), including reaction energies and estimated activation energies where known.

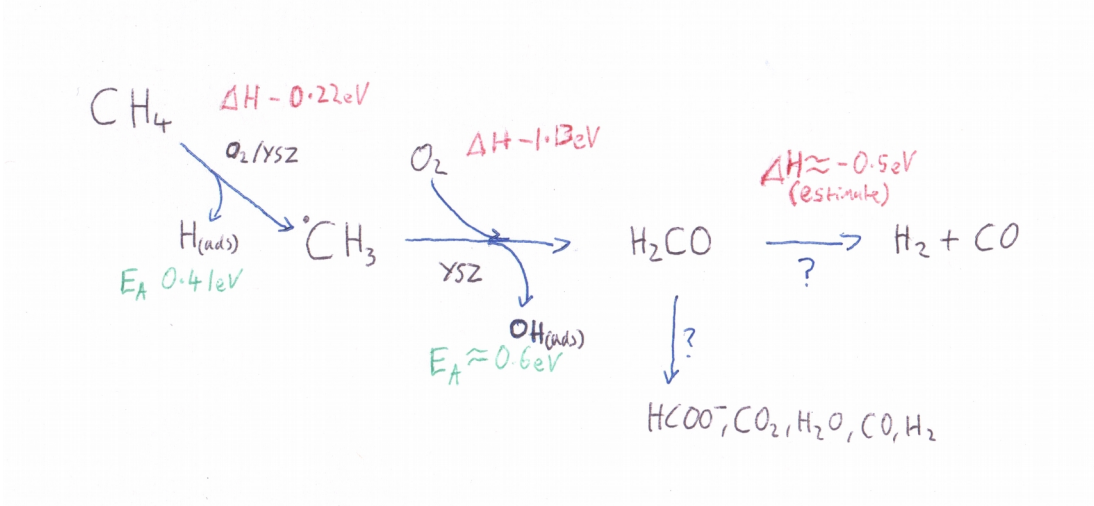

A partial reaction scheme, with reaction energies as predicted by GGA DFT. '?' represents a transformation effected by an unknown mechanism.

(Fig. 7.4.1)

A path leading from methane to formaldehyde, via the methyl radical and liberating two hydrogen atoms in the process, has been characterised by DFT modelling and reaction energetics estimated. The information on electron movement has been used to propose mechanisms for the transformations. These transformations appear to fit well with the processes proposed by Zhu et al[7] on the basis of experimental evidence from their model reactor system. The interactions between hydrogen and carbon monoxide, the components of syngas, and the bare YSZ terrace surface have been explored. The binding strengths of hydrogen to adsorption sites has been characterised to inform discussion about product release from the catalyst surface. The models presented in this chapter add considerable detail to knowledge of the mechanisms by which YSZ materials are able to catalyse conversion of methane to syngas using molecular oxygen as the oxidant.

References

[1] R. Duchovic, W. Hase, H. Schlegel, M. Frisch, K. Raghavachari, *Chem. Phys. Lett.* 98, 120, **1982**.

[2] G. Kresse, J. Furthmüller, *Comp. Mat. Sci*. 6, 15, **1996**.

[3] G. Kresse, J. Furthmüller, *Phys. Rev. B*. 54, 11169, **1996**.

[4] G. Kresse, D. Joubert, *Phys. Rev. B*. 59, 1758, **1999**.

[5] P. Blochl, *Phys. Rev. B*. 5017953, **1994**.

[6] S. Grimme, J. Antony, S. Ehrlich, H. Krieg, *J. Chem. Phys*. 132, 154104, **2010**.

[7] J. Zhu, M. Rahuman, J. van Ommen, L. Lefferts, *Appl. Catal. A*. 259, 95, **2004**.

[8] J. Zhu, J. van Ommen, L. Lefferts, *J. Catal*. 230, 291, **2005**.

Chapter 8. Summary and Conclusions

The modelling work reported in this thesis has aimed at improving knowledge of the features and properties of YSZ materials, with a particular focus on those of significance to its catalytic role in methane reforming. interatomic potentials and DFT techniques have been employed to construct models which allow both bulk and surface properties of this industrially important material to be explored. The ability of the material to conduct oxygen rapidly at high temperature is key to many of its applications. Oxygen conduction has been investigated both in the bulk, where the effects of defect proximity have been studied and near surfaces, where the material interacts with the gas phase. DFT modelling has been carried out to examine the catalytic activity of the surfaces, with a particular focus on methane reforming. Specific surface sites with the ability to adsorb and activate oxidant species from the gas phase have been identified and characterised. The activation of methane over YSZ materials has been modelled. The work reported here adds significant detail to the understanding of this important catalytically active oxide material, including a novel methane C-H bond activation mechanism, details of possible increased oxygen mobility near the surfaces and interactions of surface sites with other gas phase species relevant to reforming processes.

8.1 Bulk and Surface Structure

The work reported in Chapter 4 confirmed the current understanding of the structure of YSZ materials and extends it though application of an exhaustive configuration search. The work in chapter 4 forms the basis for the investigations in later chapters. The bulk structural parameters of cubic zirconia as predicted by the interatomic potentials model and two electronic structure methods were compared with experimental values and all found to achieve reasonable agreement (Tab. 4.1.2). The charge distribution through the bulk system predicted by electronic structure techniques was investigated, zirconium taking a +3.46 and oxygen a -1.73 charge. The effect of doping with yttrium on the electron distribution were reported, yttrium taking a charge of +2.16 in the system.

The effects of low concentration doping on the bulk structure were explored by means of a complete systematic search of the configuration space for a single defect cluster in a 2x2x2 supercell of the material (6.25% $YO_{1.5}$). A preference for NNN relationships between yttrium and vacancy positions is confirmed at low concentrations. For higher dopant concentrations the system was found to be more complex, with many defect configurations being very close in energy. At 18.75 and 25 mole % $YO_{1.5}$ it was seen that the cation lattice and overall structure remain very close to a perfect cubic arrangement; however the oxygen ion lattice undergoes increasing disorder.

8.2 Oxygen Conduction

Chapter 5 reported modelling of the important process of oxygen conduction within YSZ materials. The NEB technique was used to identify activation barriers to the migration of oxygen in the bulk lattice with between different sites. A large disparity in the barriers for migration between sites in isolated NNN defect and NN defect clusters was found, with the NNN location requiring very significantly higher energy. The disparity found supports the existing theory that close proximity to yttrium ions can trap oxygen vacancies, reducing overall conduction ability at high dopant concentrations.

The effect of surface proximity on oxygen conduction activation energies was

studied, with results reported for a large set of randomly constructed fixed linear paths and a smaller set of equivalent NEB sequences at differing depths from the surface. Both sets of results indicate a trend towards reduced migration activation energy and hence increased ionic conduction in the near surface region. The sample size is not sufficient to accurately quantify the size of the effect in general, the sequence of NEB calculations performed suggest a reduction in activation energy of approximately half between the bulk and the first subsurface layer. This finding has significance for understanding oxygen transport processes in catalytic systems, SOFCs and oxygen sensing applications of YSZ materials.

8.3 Oxidant Activation

The properties of potential surface active sites were investigated in chapter 6. Surface sites were explored, both in terms of structure and electronic properties. The surfaces ability to adsorb oxygen readily from the gas phase and transfer electron density to it, creating superoxide like radical species above oxygen vacancies was confirmed and characterised. The process was found to be moderately exothermic and to occur without a significant activation barrier.

Water was found to undergo an exothermic (-0.98eV) hydrogen sharing reaction in which one hydrogen is partially transferred to a surface oxygen adjacent to a vacancy site. No distinct activation barrier was found for the hydrogen sharing interaction. Water in this form receives some additional electron density from the surface adsorption site.

The vacancy region was identified as being able to transfer electron density through an adjacent oxygen to carbon dioxide, forming a carbonate-like CO_3 entity. The creation of the carbonate-like species from gas phase CO_2 is exothermic (-0.77eV). There is an activation barrier to this process of 0.31eV.

The activation of oxidant species is of significance to the understanding of many important catalytic properties including dry, steam and autothermal reforming processes, both when YSZ is the sole catalyst and when used to support metal particles.

8.4 Methane Oxidation

The initial hydrogen abstraction from methane is the first step in oxidative reforming and without the aid of a catalyst requires a very large energy input (bond strength 4.5eV). The YSZ surface with a superoxide like species at a vacancy site was found to be able to abstract one hydrogen from methane, leading to a surface OH species and a methyl radical. The process identified is exothermic (-0.22eV) and has an activation barrier of 0.41eV. The methyl radical is greatly more reactive than methane and will readily undergo further interaction with surface oxygen to from a formaldehyde like surface species. The formaldehyde entity is a proposed intermediate in methane reforming (discussed in chapters 1 and 7). Further significant surface reactions were explored and discussed, as is the release of hydrogen and carbon monoxide from adsorbed species.

The catalytic reactions identified in chapter 7 add significant detail to the understanding of the sites and mechanisms by which YSZ materials participate in methane reforming reactivity.

8.5 Further Work

Electronic Structure Models

GGA-DFT has well known limitations (see chapter 3) in how it represents the electronic structure of materials. In particular it has a tendency to excessively de-localise electron density. The use of hybrid functionals such as HSE06 can improve the accuracy of the electronic structures and particularly the energetics of catalytic reactions. Such a hybrid functional could be applied more widely to catalysis over YSZ materials, given sufficient computational resources. There are also approaches which allow even more computationally demanding electronic structure methods to be applied by dividing the simulation in to regions. For example, GGA-DFT could be applied to the majority of the system and a post-HF method such as Møller–Plesset perturbation theory to the atoms directly involved in reactivity.

Near Surface Oxygen Conduction

The relationship between surface proximity and oxygen conduction was explored in chapter 5. The understanding could be further improved by studying a wider range of possible defect configurations and migration paths using the same methodology as outlined in the chapter. It may also be advantageous to use a larger simulation cell to avoid any possibility of artefacts of interaction with repeat images.

The potential model and slab configuration could be used within a molecular dynamics scheme to explore temperature effects on near surface geometry and complement the results obtained using the static minimisation approach.

It may be interesting to apply the potentials based NEB methodology outlined to clustered defects which may act to trap oxygen vacancies. The research reported here only explores defect clusters limited to a single vacancy and yttrium pair. It should be possible to explore much larger defect clusters in the bulk and yttrium saturated surfaces representing the known propensity of yttrium to surface segregate in YSZ materials.

The surface model reported here is the oxygen terminated (111) terrace interface with vacuum. Other surface geometries and defects, for example steps in the (111) terrace, could be simulated and the peculiarities of oxygen migration near them explored. It may also be possible to model migration within the interface region between YSZ and other materials. A good model of the other material and the interface region would be required as a prerequisite. Interfaces of interest might include YSZ with strontium titanate which is the subject of a controversial study[1-3] reporting huge ionic conductivity within the interface, or the interfaces found within SOFCs where YSZ forms the electrolyte.

Surface Reactivity

Chapters 6 and 7 report investigations of the interactions of molecular entities with the YSZ surface. All of the interactions were investigated over the (111) oxygen terminated terrace surface only. It would be of considerable interest to model interactions with other possible surfaces such as step defects, a wider range of surface dopant arrangements and partially reduced surfaces with hydrogen present over some oxygen sites.

In the vast majority of industrial processes, including the ATR, YSZ is not used alone as a bare oxide. Typically YSZ supports or is impregnated with dispersed metallic particles, including nickel and platinum group metals. The metal particles and the YSZ support material are thought to act in synergistic fashion. Accurate modelling of the structures of metallic particles and their interactions with the YSZ surface would be a significant undertaking, but would allow for simulation of systems much closer to those found in industrial catalysis. Systems of platinum group metals on YSZ are not only of interest in methane reforming catalysis, but are also important materials in SOFCs.

The reactivity explored in chapters 6 and 7 is far from an exhaustive catalogue of possible interactions. There are intermediate and side reactions which could benefit from further investigation. The role of formaldehyde and formate could benefit from further exploration. Additional information on intermediate steps could be particularly useful in understanding factors controlling selectivity and extent oxidation, which is of crucial significance to industrial applications. In methane reforming catalysis, complete combustion represents inefficiency; any understanding of ways to improve the ratio of synthesis gas to combustion products would be of great value.

The role in methane reforming, if any, of carbonate-like activated CO_2 that forms fairly readily over YSZ surface oxygen vacancies (see section 6.3.3) has not been explored in this thesis. It may also be of interest to studies of dry reforming, methanol synthesis and carbon capture. Exploring any reactivity of the activated carbonate entity towards other adsorbates and gas phase species would be of value.

References

[1] J. Garcia-Barriocanal, A. Rivera-Calzada, M. Varela, Z. Sefrioui, E. Iborra, C. Leon, S. Pennycook, J. Santamarial, *Science*. 321, 676, **2008**.

[2] X. Guo, *Science.* 324, 465, **2009**.

[3] J. Garcia-Barriocanal, A. Rivera-Calzada, M. Varela, Z. Sefrioui, E. Iborra, C. Leon, S. Pennycook, J. Santamarial, *Science*. 324, 465b, **2009**.

Acknowledgements

I would like to thank my supervisors, Prof. Richard Catlow and Richard Oldman, for their inspiration, guidance and direction throughout my studies. Their wisdom, advice and input has been invaluable.

Personal thanks is owed to my partner Claire for her patient support and encouragement throughout, and to other members of Prof. Catlow's research group for stimulating conversation and constructive advice.

Thanks is owed to Johnson Matthey for sponsorship, and especially Sam French and Martin Fowles for their involvement.

I am grateful to UCL, EPSRC and the HPC Materials Chemistry Consortium for access to computational facilities, without which this work would not have been possible.